Compact Symmetric Objects. III. Evolution of the High-luminosity Branch and a Possible Connection with Tidal Disruption Events

A. C. S Readhead[1] , V. Ravi[1] , R. D. Blandford[2] , A. G. Sullivan[2] , J. Somalwar[1] , M. C. Begelman[3,4] ,
M. Birkinshaw[5] , I. Liodakis[6] , M. L. Lister[7] , T. J. Pearson[1] , G. B. Taylor[8] , P. N. Wilkinson[9], N. Globus[10],
S. Kiehlmann[11] , C. R. Lawrence[12], D. Murphy[12], S. O'Neill[1], V. Pavlidou[11,13], E. Sheldahl[8], A. Siemiginowska[14] , and
K. Tassis[11,13]

[1] Owens Valley Radio Observatory, California Institute of Technology, Pasadena, CA 91125, USA; acr@caltech.edu
[2] Kavli Institute for Particle Astrophysics and Cosmology, Department of Physics, Stanford University, Stanford, CA 94305, USA
[3] JILA, University of Colorado and National Institute of Standards and Technology, 440 UCB, Boulder, CO 80309-0440, USA
[4] Department of Astrophysical and Planetary Sciences, University of Colorado Boulder, 391 UCB, Boulder, CO 80309-0391, USA
[5] School of Physics, H.H. Wills Physics Laboratory, University of Bristol, Tyndall Avenue, Bristol BS8 1TL, UK
[6] Finnish Center for Astronomy with ESO, University of Turku, Vesilinnantie 5, FI-20014, Finland
[7] Department of Physics and Astronomy, Purdue University, 525 Northwestern Avenue, West Lafayette, IN 47907, USA
[8] Department of Physics and Astronomy, University of New Mexico, Albuquerque, NM 87131, USA
[9] Jodrell Bank Centre for Astrophysics, University of Manchester, Oxford Road, Manchester M13 9PL, UK
[10] Department of Astronomy and Astrophysics, University of California, Santa Cruz, CA 95064, USA
[11] Institute of Astrophysics, Foundation for Research and Technology-Hellas, GR-70013 Heraklion, Greece
[12] Jet Propulsion Laboratory, California Institute of Technology, 4800 Oak Grove Drive, Pasadena, CA 91109, USA
[13] Department of Physics and Institute of Theoretical and Computational Physics, University of Crete, 70013 Heraklion, Greece
[14] Center for Astrophysics—Harvard and Smithsonian, 60 Garden Street, Cambridge, MA 02138, USA

Abstract

We use a sample of 54 compact symmetric objects (CSOs) to confirm that there are two unrelated CSO classes: an edge-dimmed, low-luminosity class (CSO 1), and an edge-brightened, high-luminosity class (CSO 2). Using blind tests, we show that CSO 2s consist of three subclasses: CSO 2.0, having prominent hot spots at the leading edges of narrow jets and/or narrow lobes; CSO 2.2, without prominent hot spots and with broad jets and/or lobes; and CSO 2.1, which exhibit mixed properties. Most CSO 2s do not evolve into larger jetted active galactic nuclei (AGN), but spend their whole life cycle as CSOs of size $\lesssim$500 pc and age $\lesssim$5000 yr. The minimum energies needed to produce the radio luminosity and structure in CSO 2s range from $\sim 10^{-4} M_\odot c^2$ to $\sim 7 M_\odot c^2$. We show that the transient nature of most CSO 2s, and their birth rate, can be explained through ignition in the tidal disruption events of stars. We also consider possibilities of tapping the spin energy of the supermassive black hole, and tapping the energy of the accretion disk. Our results demonstrate that CSOs constitute a large family of AGN in which we have thus far studied only the brightest. More comprehensive CSO studies, with higher sensitivity, resolution, and dynamic range, will revolutionize our understanding of AGN and the central engines that power them.

1. Introduction

Compact symmetric objects (CSOs) are extragalactic radio sources less than 1 kpc in extent that show emission on both sides of their center of activity and in which the observed emission is not dominated by relativistic motion toward the observer (Wilkinson et al. 1994; Readhead et al. 1996, hereafter R96). A major development in the study of CSOs was the discovery that there are two, distinct, classes of CSOs: an edge-dimmed low-luminosity class, which we designate as CSO 1, and an edge-brightened high-luminosity class, which we designate as CSO 2 (Tremblay et al. 2016, see their Section 4.4 and Figure 11).

Compact radio sources associated with active galactic nuclei (AGN) exhibit a wide variety of morphological and radio spectroscopic types. This paper cannot do justice to the enormous amount of work that has been done in this field, and which is the foundation upon which it is built, but to place CSOs in the wider context, the reader is referred to the excellent and exceptionally comprehensive review of the field by O'Dea & Saikia (2021; hereafter OS21), which is both up to date and also traces it back to its origins.

From the earliest studies, CSOs have often been designated as "young" objects, or as objects showing "recurrent" activity (see, e.g., Mutel & Phillips 1980; Phillips & Mutel 1980; Pearson & Readhead 1988; Baum et al. 1990; Conway et al. 1992; R96; Orienti & Dallacasa 2014). In this study we show that these descriptors, "young" and "recurrent," are misleading. We find strong evidence supporting the hypothesis that most CSO 2s exhibit a full life cycle from birth to death as CSOs, and so they cannot correctly be described as "young," although they can correctly be described as "short-lived," as compared to classes of larger jetted AGN, such as FR I and FR II objects (Fanaroff & Riley 1974). The hypothesis that high-luminosity CSOs are short-lived was first put forward by Readhead et al. (1993; hereafter R93). Throughout the previous CSO literature,

including in R93, the terms "young" and "short-lived" have been treated as synonymous, which they are not. To avoid confusion with the earlier literature we will use the terms "early life," "midlife" and "late life" to describe the different evolutionary stages of CSO 2s.

In this paper we present evidence which supports the hypothesis that ∼40% of the bona fide CSO 2s we have identified are "early life," ∼30% are "midlife," and ∼30% are "late life," compared to their overall lifetimes, which range from ≲100 yr to ∼5000 yr. We then discuss the energies, ages, birth rates, and possible origins of CSO 2s in the context of single star capture by a supermassive black hole (SMBH), as was first suggested by Readhead et al. (1994; hereafter R94), with its implications for tidal disruption events (TDEs; Rees 1988) and the late stages of evolution of TDEs with radio jets (jetted TDEs). The possibility that CSO 2s are fueled by the capture of single stars by an SMBH has also been suggested by An & Baan (2012). We also consider two other possible origins of the energy of CSO 2s, namely, the spin of the SMBH and the accretion disk.

An unfortunate development of the last 20 yr in the study of CSOs is that there are now many misclassified CSOs in the literature. This is what led to the present study.

This paper is the third of three papers on the morphological radio properties of CSOs in which we explore the phenomenology of CSOs uncontaminated by misidentified objects. In the first paper (Kiehlmann et al. 2024a, hereafter Paper I), we added two new criteria, based on variability and speed, to the CSO selection criteria and undertook a detailed survey of the literature with the sole purpose of filtering out the misclassified CSOs. This enabled us to identify 79 bona fide CSOs. Our 79 bona fide CSOs include three complete samples[15] that are therefore suitable for statistical studies. In the second paper (Kiehlmann et al. 2024b, hereafter Paper II), we determined the fractions of CSOs in these complete samples. All of the CSOs in these complete samples are CSO 2s. We used the subset of 17 bona fide CSO 2s in these complete samples to show that CSO 2s form a distinct subclass of jetted AGN that has a sharp upper cutoff in size at ≈500 pc.

Another potentially misleading descriptor in CSO studies is the use of the term "recurrent" for CSOs in which there is evidence of more than one epoch of activity. Five of our bona fide CSOs show evidence of more than one epoch of activity, with a distinct gap, or drop in surface brightness, between the emission regions associated with each episode. In our view it should not be assumed that any previous activity was a manifestation of the same physical process as that which produces CSOs, and we present evidence showing that these earlier epochs of activity were a factor 30–1000 times more energetic than the CSOs. For this reason we should use the descriptor "episodic," rather than "recurrent," for this class of rare CSOs, which comprises ∼6% of the bona fide CSOs we have identified. Four CSO 2 objects and one CSO 1 object, out of our total of 79 bona fide CSOs, were found to be episodic.

Throughout this paper we adopt the convention $S_\nu \propto \nu^\alpha$ for spectral index α, and, for consistency with our other papers, we use the cosmological parameters $\Omega_m = 0.27$, $\Omega_\Lambda = 0.73$ and $H_0 = 71$ km s^{-1} Mpc^{-1} (Komatsu et al. 2009). None of the conclusions would be changed were we to adopt the best model

of the Planck Collaboration (Planck Collaboration et al. 2020). In this paper we follow the lead of OS21 in their comprehensive review of peaked spectrum sources, and refer to gigahertz-peaked spectrum sources as peaked spectrum (PS) sources.

2. The Bona Fide CSO Sample and the Scope of This Paper

In this paper we focus on the 54 bona fide CSOs with spectroscopic redshifts that we identified in Paper I. This sample is listed in Table 1. Representative images of these 54 objects are shown in Figure 1. As first pointed out by Baldwin (1982), "This is the radio astronomer's H-R diagram." To make it easy to associate the images with the source data, the order in Table 1 is the number of each object in Figure 1. To facilitate looking up individual sources by name, a version of Table 1 with the objects listed in order of R.A. is given in Table 8 in Appendix A. A brief description of each source is given in Appendix B.

The distribution of our 54 bona fide CSOs between the CSO 1 and CSO 2 classes in the luminosity (P)–size (D) plane is shown in Figure 1, where CSO 1s and CSO 2s are represented by empty squares and filled circles, respectively. The (P, D) values are taken from Paper I, which lists the relevant references. We see that CSO 1s tend to have lower luminosities than CSO 2s, and hence tend to occupy a different region of the (P, D) plane. The luminosities refer to that at the peak of each CSO's radio spectrum, and the sizes are measured from the radio contour maps, as described in Paper I. In six cases the peak occurs below the lowest frequency at which the source has been observed. These are indicated by the up arrows in Figure 1.

2.1. The Emerging Picture of the CSO Family

Since medium symmetric objects (MSOs; Fanti et al. 1995; R96) and FR Is and FR IIs (Fanaroff & Riley 1974) are all symmetric double radio sources that are larger than CSOs, it is highly likely that they began as CSO 2s before reaching 1 kpc in size. Since the timescales are too long to confirm this in individual cases, we take as a working hypothesis that all of these larger-scale doubles did in fact pass through an early CSO 2 phase. In Paper II we saw that fewer than ∼1% of CSO 2s can evolve into larger-scale radio doubles, such as FR Is and FR IIs, and only ∼5% can evolve into MSOs and compact steep spectrum (CSS) sources. Thus, the whole family of CSOs probably embraces at least the following three classes of CSOs, which we present as a schematic diagram in Figure 2:

1. CSO 1s, which, since they are edge dimmed, might be important for feedback and star formation, and/or may be related to FR 0s (Baldi et al. 2015; Baldi 2023).
2. The vast majority of CSO 2s that do not go on to form MSOs, FR Is, or FR IIs, and are the main focus of this paper.
3. The small minority of CSO 2s that we hypothesize do go on to form MSOs, FR Is, or FR IIs.

This subject remains in its infancy, since so far we have studied mostly high-luminosity CSOs. We may well discover further distinct classes of CSOs, or other interesting connections, as we delve deeper into the CSO luminosity function. We have tried to leave room for this in the schematic of Figure 2.

---

[15] A "complete sample" is defined to be a sample that includes all objects down to a given flux density limit over a given area of sky (Pooley & Ryle 1968; Schmidt 1968; Longair & Scheuer 1970).

Table 1
Key to the CSOs in Figure 1 in Numerical Order[a]

ID #	Source Name	z	Class	ID #	Source Name	z	Class
1	J1111+1955	0.299	CSO 2.0	28	J1347+1217†	0.121	CSO 2.2
2	2022+6136†	0.227	CSO 2.1	29	J1944+5448†	0.263	CSO 2.0
3	J0111+3906†	0.668	CSO 2.0	30	J1440+6108	0.445365	CSO 2.1
4	J1735+5049†	0.835	CSO 2.0	31	J1816+3457	0.245	CSO 2.1
5	J2203+1007	1.005	CSO 2.0	32	J1158+2450	0.203	CSO 2.2
6	J1734+0926	0.1813	CSO 2.0	33	J1508+3423	0.045565	CSO 2.1
7	J1939−6342	0.735	CSO 2.0	34	J1234+4753	0.373082	CSO 2.1
8	J0029+3456†	0.772137	CSO 2.1	35	J0119+3210†	0.0602	CSO 2.2
9	J0741+2706	1.601115	CSO 2.0	36	J1414+4554	0.186	CSO 2.1
10	J0943+1702	0.518	CSO 2.0	37	J1945+7055	0.101	CSO 2.2
11	J0713+4349†	0.46	CSO 2.0	38	J1311+1658	0.081408	CSO 1
12	J1035+5628†	0.517	CSO 2.0	39	J0855+5751	0.025998	CSO 2.1
13	J1326+3154†	0.37	CSO 2.2	40	J1025+1022	0.045805	CSO 1
14	J1609+2641†	0.473	CSO 2.1	41	J0131+5545	0.03649	CSO 2.2
15	J1400+6210†	0.431	CSO 2.2	42	J1148+5924	0.01075	CSO 1
16	J1227+3635†	1.975	CSO 2.0	43	J1205+2031	0.024037	CSO 2.1
17	J1159+5820	1.27997	CSO 2.0	44	J0909+1928	0.027843	CSO 1
18	J0825+3919	1.21	CSO 2.1	45	J1220+2916	0.002	CSO 1
19	J1244+4048†	0.813586	CSO 2.2	46	J0906+4124	0.027	CSO 1
20	J1313+5458	0.613	CSO 2.2	47	J1559+5924	0.0602	CSO 1
21	J1120+1420	0.362	CSO 2.0	48	J1254+1856	0.1145	CSO 1
22	J1434+4236	0.452	CSO 2.2	49	J1723−6500	0.01443	CSO 2.1
23	J1644+2536	0.588	CSO 2.1	50	J1247+6723	0.107219	CSO 2.0
24	J2355+4950†	0.238	CSO 2.2	51	J1511+0518	0.084	CSO 2.0
25	J1915+6548	0.486	CSO 2.1	52	J1407+2827†	0.077	CSO 2.1
26	J1602+5243	0.105689	CSO 1	53	J0405+3803†	0.05505	CSO 2.0
27	J2327+0846	0.02892	CSO 1	54	J0832+1832	0.154	CSO 1

Notes. The ID # is the reference number in Figure 1. Other common names of these objects are given in Paper I, which also gives references for the redshifts. † indicates objects in the complete PR+CJ1+PW sample.
[a] A version of this table in R.A. order may be found in Table 8 in Appendix A.

We emphasize that CSOs may well be formed by a variety of mechanisms.

Thus, this paper is not intended to provide a complete description of CSOs, which is, in any case, impossible at this early stage in their study, but rather to draw attention to the peculiar properties of $\gtrsim 99\%$ of CSO 2s. Thus, we focus primarily on #2 above and the possible connection with TDEs. We are limited in our complete samples to the brightest, and hence most luminous, CSOs—i.e., to CSO 2s, of which, as shown in Paper II, the majority are short-lived and exhibit a sharp cutoff in size at ∼500 pc. In addition, we particularly wish to draw attention to the potential of CSO 2s for addressing many interesting questions of AGN and relativistic jet physics through the combination of time-domain astronomy and high-resolution imaging.

The follow-up of these high-luminosity CSO 2 observations with observations that include both lower-luminosity CSO 1s and CSO 2s is clearly of paramount importance in understanding AGN (OS21), the creation of relativistic jets (OS21), and feedback (OS21). For these reasons, we have embarked upon a program to observe the steep spectrum counterpart of the incomplete Very Long Baseline Array (VLBA) Imaging and Polarimetry Survey (VIPS; Helmboldt et al. 2007) flat spectrum sample, which will extend the CSO luminosity function almost an order of magnitude below the level considered in this study.

In view of our focus on high-luminosity objects, in this paper we do not discuss in detail the properties of CSO 1s. CSO 1s are sufficiently different, morphologically, to CSO 2s, that we think they merit intensive study on their own. In view of their similar edge-dimmed morphologies, it is possible that CSO 1s are related to FR 0s, and may be of great interest in the study of feedback (Duggal et al. 2021).

Another important consideration is that of potentially "frustrated" CSOs (van Breugel et al. 1984; Wilkinson et al. 1984; O'Dea et al. 1991; O'Dea 1998), objects in which the small size is due to confinement by the interstellar medium of the host galaxy. We are aware of these factors that complicate the study of CSOs. Again, a study of this interesting class of objects is beyond the scope of the present paper, but we include this possibility in Figure 2.

Similarly, while in this paper we advance the hypothesis that many CSO 2s are formed by single star capture, we are not suggesting that *all* CSO 2s are formed in this way, and we cannot yet even be certain that *any* CSO 2s are formed in this way. In Section 13 we consider at length alternative scenarios for the formation of CSO 2s.

It should therefore be clear that it is not our intent in this paper to attempt to describe the whole phenomenology of CSOs. Any such description will require a concerted effort, pushing to lower luminosities, and this will take many years, possibly several decades, to accomplish.

3. CSO 1 and CSO 2 Classes

The sole criterion we apply to distinguish between CSO 1s and CSO 2s is the "edge-dimmed" versus "edge-brightened" morphology. We do not apply any luminosity constraints on either class. By "edge dimmed" we mean that
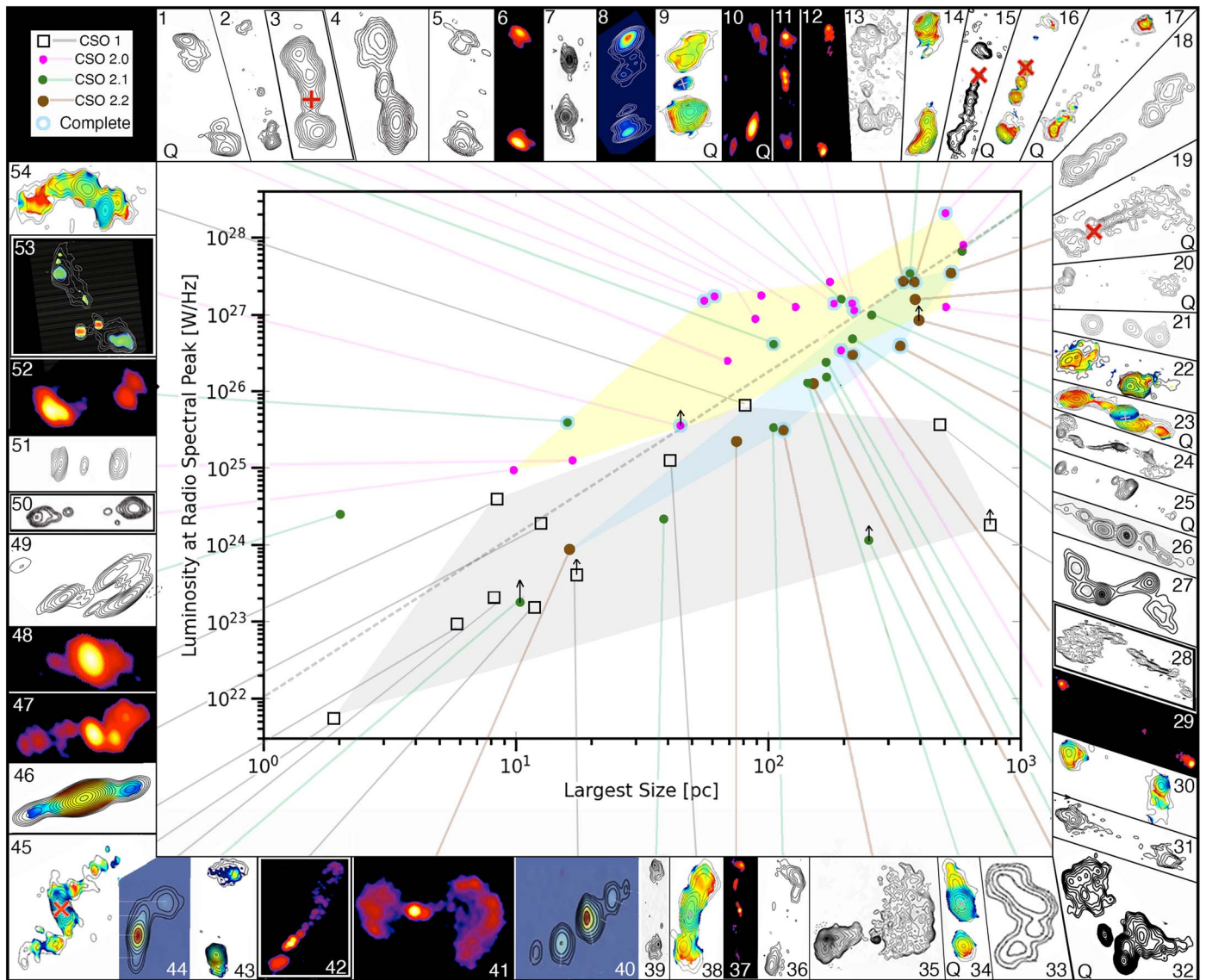
Figure 1. The radio astronomer's "Hertzsprung–Russell diagram" (Baldwin 1982) for CSOs: the distribution in the luminosity–size (*P*, *D*) plane of the 54 bona fide CSOs for which we have spectroscopic redshifts. Open square symbols: CSO 1 objects. Pink, green, and brown filled circles: CSO 2.0, 2.1, and 2.2 objects, respectively. Up arrows on symbols indicate CSOs with rising spectra below 1 GHz, for which we have only a lower limit on the peak luminosity. The light blue annuli around the symbols indicate objects in the complete Pearson & Readhead (1988; PR), the first Caltech–Jodrell Bank survey (CJ1; Polatidis et al. 1995), and the survey of Peacock & Wall (1982; PW) sample. The diagonal dashed line, dividing the (*P*, *D*) plane in two, has been drawn by eye to maximize the ratio of CSO 2.0 objects above the line to those below the line, and to maximize the ratio of CSO 2.2 objects below the line to those above the line. The references for the 54 radio emission maps in this figure are indicated by a dagger symbol[†] in the individual source notes in Appendix B. Many of the maps have their true sky orientations rotated for arrangement purposes. CSOs for which there is evidence of more than one epoch of activity are indicated by double borders—i.e., CSO 1 (#42) CSO 2.0s (#3, #50, and #53), and CSO 2.2 (#28). In these five cases, the size plotted refers to the most recent activity (see text). Quasars are indicated by the letter "Q." The other CSOs are radio galaxies. The faint yellow, blue, and gray regions show the areas of the (*P*, *D*) plane occupied by the CSO 2.0, CSO 2.2, and CSO 1 objects, respectively, making it clear that they predominantly occupy different regions of the (*P*, *D*) plane (see text).

moving out from the center of activity the surface brightness drops. By "edge brightened" we mean that moving out from the center of activity the surface brightness first increases, but that it may drop toward the outer extremities of the source.

As can be seen from Figure 1, there is a wide variety of CSO 2 morphologies, but we have managed to classify these using three subclasses, which, as we show later, likely correspond to an evolutionary sequence:

CSO 2.0: these are CSOs in which there are two distinct outer lobes, making them edge brightened, with hot spots at their outer edges opposite the nucleus, narrow jets (if visible at all), and lobes not much wider than the hot spots. These are

indicated by pink symbols in Figure 1, with pink lines connecting their positions in the (*P*, *D*) plane to their corresponding images.

CSO 2.2: these are CSOs in which there are two distinct outer lobes but the hot spots are not dominant or are invisible, or the lobes are well resolved normal to the jet axis. The hot spot, or hot spots, do not need to be located at the end of the lobe opposite the core. These are indicated by brown points in Figure 1, with brown lines connecting the points in the (*P*, *D*) plane to their corresponding images.

CSO 2.1: these are "indeterminate," or "intermediate," CSO 2s, which have some of the properties of CSO 2.0s and some of the properties of CSO 2.2s. For example, they might look like
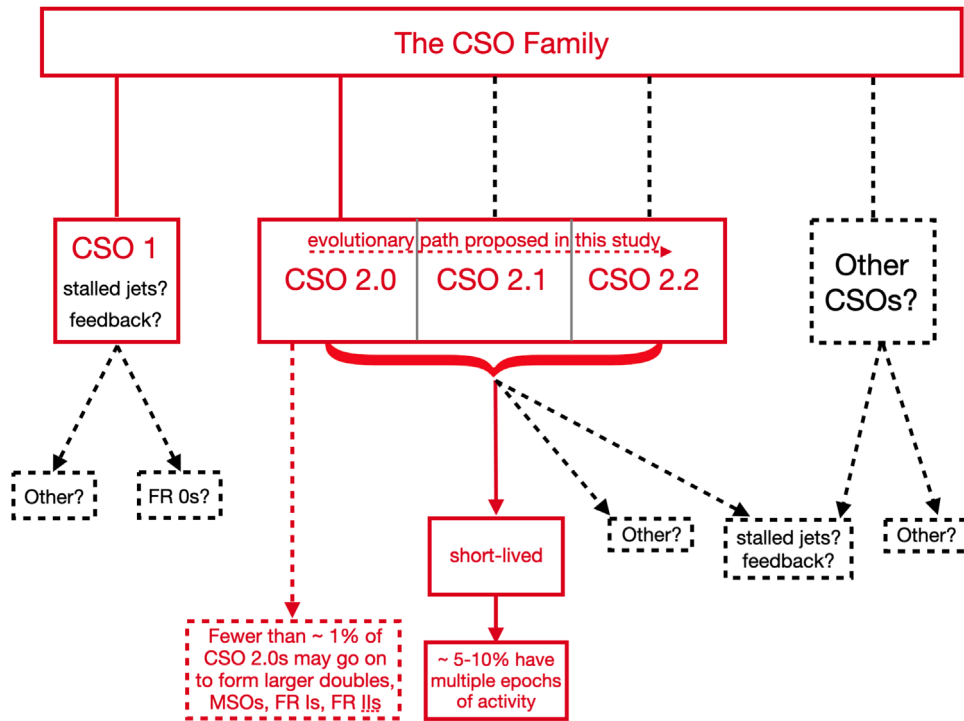
Figure 2. The complex emerging picture of the CSO family thus far. The solid boxes, lines, and arrows indicate distinctions that in our view have been firmly established in these three papers. The dotted lines indicate hypotheses that remain to be proven. The red items are all discussed in varying amounts of detail in Papers I, II, and III. The black items are other possibilities that have been discussed in the literature, and/or that are likely to be verified or discovered as we observe fainter CSOs and dig deeper into the CSO luminosity function. For details on FR0s, FR Is, FR IIs, stalled jets, feedback, and multiple epochs of activity the reader is referred to OS21.

Table 2
Binomial Tests of the Numbers of Successes in the Blind Test Classifications

Number of CSOs	Teams in Agreement	Expected Fraction	Expected Number	Observed Number	Observed Fraction	Binomial Probability
54	4	0.0156	1	26	0.47	1.3×10^{-32}
54	3 or 4	0.203	10	46	0.85	2.4×10^{-24}
54	2	0.703	38	8	0.15	3.4×10^{-17}
54	0	0.0937	5	0	0	4.9×10^{-3}

Notes. Each row shows the result for the number of teams in agreement given in the second column. We see that all four teams agreed on the classification for 26 of the 54 CSOs, whereas only one was expected in the case of purely random class assignments. We also see that three or four of the teams were in agreement on 46 of the CSOs, whereas only 10 were expected. As shown here, were the distribution random, we would expect five cases where none of the four teams were in agreement, whereas in fact there were no such cases.

CSO 2.0s on one side of the nucleus and CSO 2.2s on the other side, or they might have hot spots that are not located at the extremities of their envelopes. These are indicated by green points in Figure 1, with green lines connecting the points in the (P, D) plane to their corresponding images. Two objects in this "indeterminate" class (#33 and #49 in Figure 1) have very peculiar morphologies that seem unrelated in any way to other CSO 2s, so they are "indeterminate," but the remainder are all mixtures of CSO 2.0 and CSO 2.2 morphologies, and may be designated as "intermediate."

Our reasons for assigning each of the 54 CSOs to the four classes, CSO 1, CSO 2.0, CSO 2.1, or CSO 2.2, are given for each object individually in Appendix B. To ensure that we were not biasing the distributions of and conclusions about the different CSO 2 classes in the (P, D) plane, and to assess the reliability and reproducibility of our CSO classification scheme, we carried out blind tests to classify the 54 bona fide CSOs for which we have spectroscopic redshifts. These blind tests and their results are described in Appendix C.

In the blind tests we used four teams, and their classifications as well as the final classifications we adopted are given in Table 9 in Appendix C. The significance of these classifications can be tested against the hypothesis that the CSOs are randomly distributed. Results are given in Table 2. Since there are four classes and four teams, there are $4^4 = 256$ possible outcomes of the blind test on each of the 54 CSOs being classified. The details of the calculations of the expected fractions and binomial probabilities shown in Table 2 are given in Appendix C.

The binomial probabilities, shown in the seventh column of Table 2 leave no room for doubt that the classification system is one that is astrophysically meaningful, and therefore provides a useful description of CSOs. Thus, in spite of the variety of morphologies exhibited by CSOs, they can reliably be assigned to one of the four morphological classes defined above.

Table 3
The Numbers and Percentages of CSOs in the Different Classes

Class	Number in Class	Percentage of Total	Percentage of CSO 2s
CSO 1	11	20% ± 7%	⋯
CSO 2.0	17	31% ± 9%	40% ± 11%
CSO 2.1	15	28% ± 8%	35% ± 10%
CSO 2.2	11	20% ± 7%	26% ± 9%

Note. The numbers and fractions of CSOs in the different CSO classes for the full total of 54 CSOs with spectroscopic redshifts, and for the 43 CSO 2s with spectroscopic redshifts.

4. Distributions of CSOs among the Different Classes

In Table 3 are shown the numbers and percentages of the CSOs in different classes out of the 54 bona fide CSOs with spectroscopic redshifts. In Papers I and II we discussed a variety of selection effects that are mainly of relevance to the size distribution of CSO 2s. In this paper we focus on selection effects that are of particular relevance to the distributions of the different classes of CSOs that we have identified and their distributions in the (P, D) plane.

4.1. Selection Effects among the Four CSO Classes

There are many selection biases in this sample, and in particular there is a strong redshift selection bias, so the interpretation of the data on these 54 sources must be treated with care. But the 54 CSOs populate the (P, D) plane densely enough for us to be able to look for variations in morphology with P and D among the high-luminosity CSOs, above 10 pc in size. It is important to consider any biases that might affect the distribution of the four classes of CSOs in the (P, D) plane. For this purpose we show in Figure 3 the redshift distributions of the different classes of CSOs. It is immediately clear that CSO 1s are seen predominantly at lower redshifts than CSO 2s. This is undoubtedly a selection effect due to the fact that CSO 1s are low-luminosity objects and that their symmetric regions, being edge dimmed, are of low surface brightness. Both of these effects will push high-redshift CSO 1s below the detection levels of the finding surveys, which have, thus far, been restricted to high flux densities. It is to be expected, therefore, that CSO 1s will be found at higher redshifts as the survey flux density limits are extended downwards.

We will not discuss the redshift distribution of CSO 2.1s since they have mixed CSO 2.0 and CSO 2.2 characteristics. We therefore compare the redshift distributions of the CSO 2.0s and CSO 2.2s shown in Figure 3. Although the two distributions overlap substantially, it appears, by eye, to be the case that the CSO 2.2s are concentrated at somewhat lower redshifts than the CSO 2.0s. The Kolmogorov–Smirnoff (K-S) two-sample test gives a K-S test statistic of 0.55 and a p-value = 0.0026. So it is rather unlikely that these two distributions are drawn from the same parent population, although the possibility that they are cannot be ruled out definitively.

If this is due to selection bias, the implication is that our sample is missing CSO 2.2 objects at high redshifts. This would not be surprising because, like the CSO 1 sources, CSO 2.2 objects lack bright hot spots and their lobes have lower surface brightnesses than those of CSO 2.0 objects. Thus this

selection effect is in the sense that it biases against detecting CSO 2.2s in the lower right-hand quadrant of the (P, D) plane.

The distributions in size and luminosity of CSO 1s versus CSO 2s are shown in Figure 4. The sizes and luminosities are taken from Paper I. As in Paper I, the "peak luminosities" are the luminosities at the frequency of the peak of the spectrum for CSOs with PS, and at the lowest observed frequency for six CSOs which have monotonically falling spectra. In Figure 4 it can be seen that CSO 1s are on average smaller and less luminous than CSO 2s. These are clearly two very different classes of objects: the CSO 1s tend to be nearby, low-luminosity objects, whereas the CSO 2s have higher luminosities that lie in the range of FR I and FR II objects.

While CSO 1s are clearly a very interesting class of jetted AGN, there are no immediately apparent morphological trends among the bona fide CSO 1s in our sample that can be followed up, and we will have to wait for larger, deeper surveys to investigate the evolution of CSO 1s. For this reason we focus for the rest of this paper on the CSO 2s, for which we find that there are interesting morphological trends.

4.2. Comparison of CSO 2.0s and CSO 2.2s

The distributions in size and luminosity of CSO 2.0s versus CSO 2.2s are shown in Figure 5, where it can be seen that on average the CSO 2.0s are smaller than the CSO 2.2s, and on average their luminosities are larger. For the whole sample of 54 CSOs with spectroscopic redshifts, the median size of the CSO 2.0s is 129 pc and the median size of the CSO 2.2s is 340 pc, i.e., the ratio of the median sizes is ∼2.6:1. For the PR+CJ1+PW subsample these numbers are 190 pc and 340 pc, i.e., a ratio of the median sizes of ∼1.8:1. For the whole sample of 54 CSOs with spectroscopic redshifts, the median luminosities of CSO 2.0s and CSO 2.2s are 12 and 4×10^{26} W Hz^{-1}, respectively, i.e., the ratio of the median luminosities is ∼3:1. For the PR+CJ1+PW subsample these numbers 1.4×10^{27} W Hz^{-1} and 1×10^{27} W Hz^{-1}, respectively, i.e., the ratio of the median luminosities is ∼1.4:1. As we have discussed in Papers I and II, the whole sample is heavily affected by sampling effects, so it is the complete PR+CJ1+PW subsample that we should use, and for this we see that the CSO 2.0s are significantly smaller than the CSO 2.2s, but their luminosities are comparable.

Summary of classifications in the (P, D) plane. The areas of the (P, D) plane occupied by the CSO 1s, 2.0s, and 2.2s are shown by the faint gray, yellow, and blue highlighted regions in Figure 1, respectively. These make it clear that these different classes occupy different, but overlapping, portions of the (P, D) plane.

5. The Evolution of CSO 2s

In this paper we aim only at a very basic approach to the evolution of CSO 2s. We wish to determine whether or not there is clear evidence for the evolution of CSO 2s in the (P, D) diagram shown in Figure 1. Fundamentally, we wish to determine whether the hypothesis of R93 that most high-luminosity CSOs are "short-lived" is correct or not. We see in the (P, D) plot that CSO 2.0s are all larger than 20 pc. If we consider only the region of the (P, D) diagram above 20 pc, we see that there is a tendency for the CSO 2.0s to be located toward the upper left-hand side (yellow region) of the
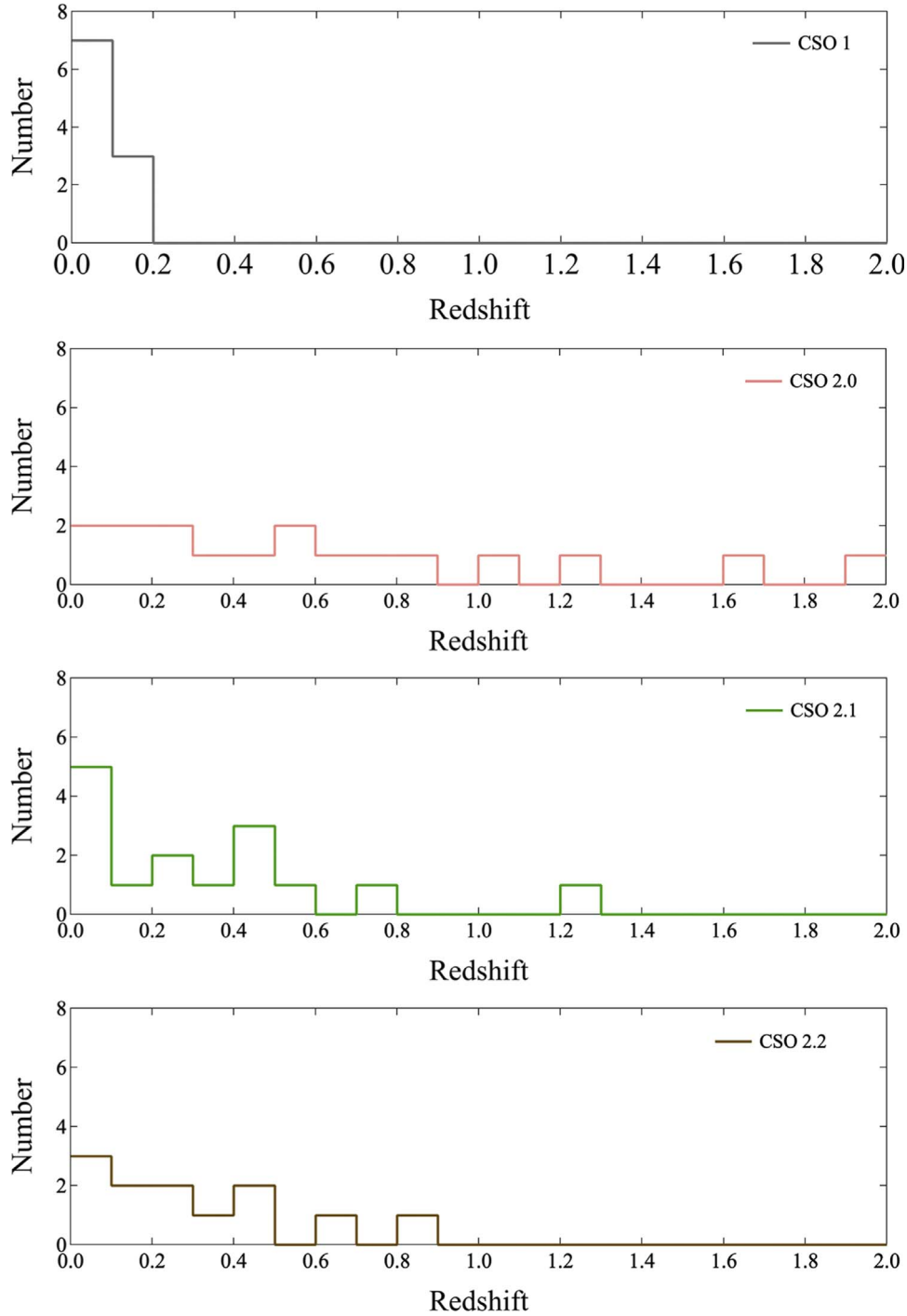
Figure 3. Redshift distributions of the CSO classes.

distribution, and the CSO 2.2s toward the lower right-hand side (blue region).

5.1. Selection Effects in the CSO 2 (P, D) Distribution

In Figure 1, there is an upper envelope of the CSO 2s that rises from $P \sim 10^{25}$ W Hz^{-1} at $D \sim 10$ pc to $P \sim 3 \times 10^{28}$ W Hz^{-1} at $D \sim 500$ pc. This is likely due to the combined effect of (i) the finite resolution of very long baseline interferometry (VLBI; ≈ 4 mas), so that the smallest angular size CSOs recognizable in 8 GHz VLBI surveys is ≈ 30 pc at $z = 1$; and (ii) the CSO luminosity function. In Figure 6(a) we

show the (P, D) diagram for the PR+CJ1+PW sample broken up into different redshift bins. Note that the upper envelope has the same characteristics as that of the whole sample, shown in Figure 1. We see that the luminosity increases with redshift bin. This tells us that the lower-luminosity CSO 2s seen in the low-redshift bins do not all evolve into high-luminosity objects. Conversely, the higher-luminosity objects seen in the higher-redshift bins are not seen at low redshifts due to the steepness of the luminosity function.

The lower envelope in Figure 1 is due to the selection effect of the flux density limits of the complete samples. We see that the lower envelope of the CSO 2s is more or less flat at
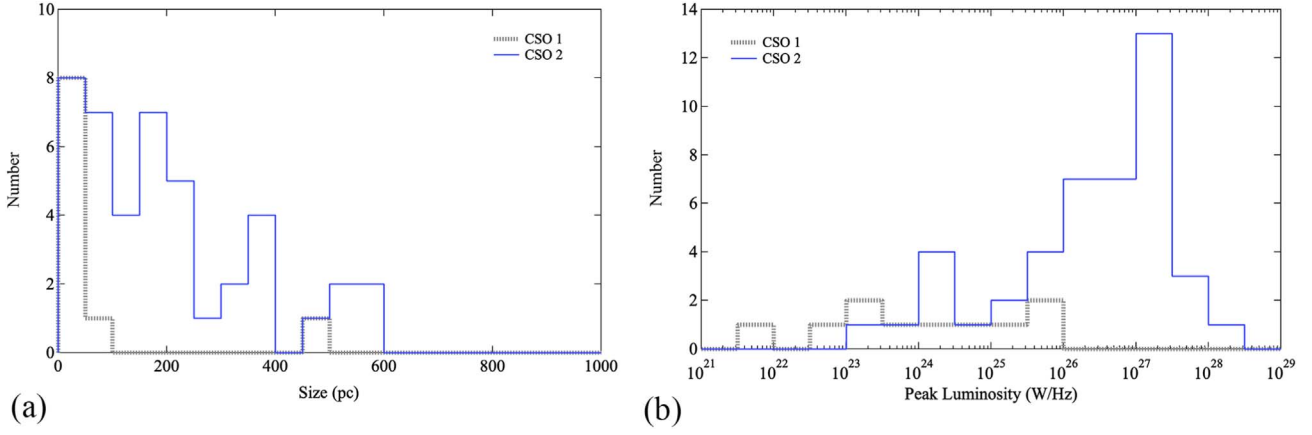
Figure 4. Comparison of CSO 1s and CSO 2s. (a) The distributions of the largest projected linear sizes. (b) The distributions of the peak luminosities.
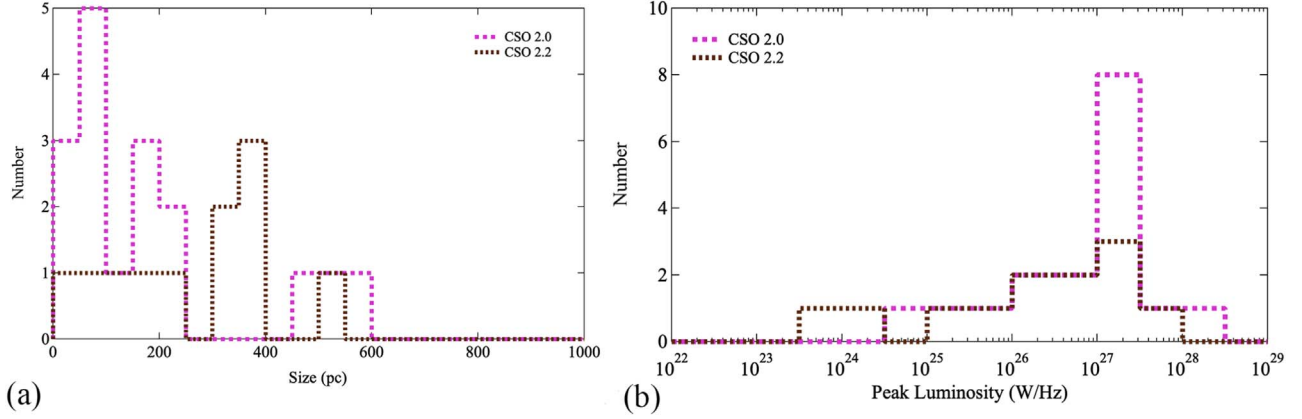

Figure 5. (a) Comparison of the largest projected linear sizes of CSO 2.0s and CSO 2.2s. (b) Comparison of the luminosities of CSO 2.0s and CSO 2.2s.
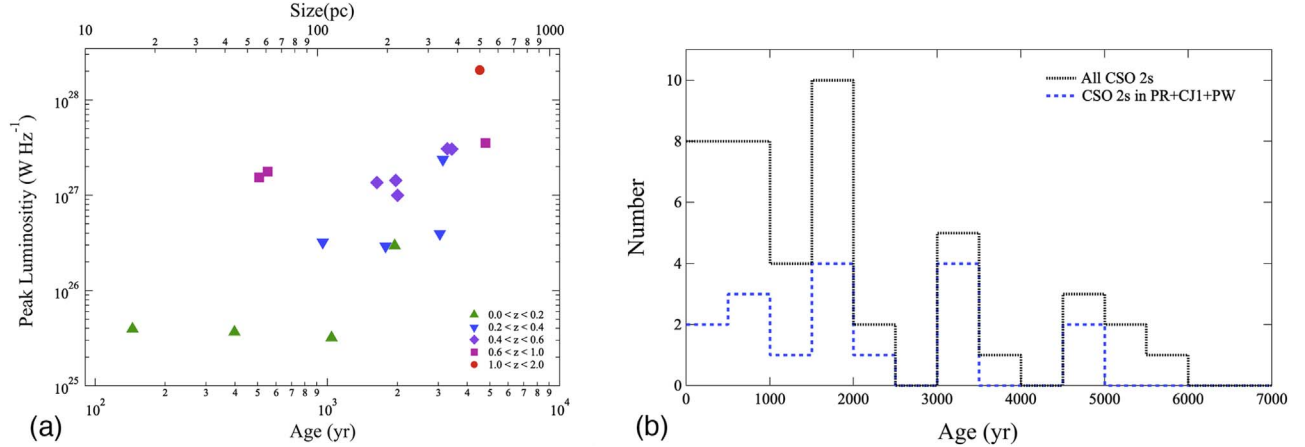

Figure 6. Sizes, ages and luminosities of CSO 2s, assuming a hot spot separation speed of $v_s = 0.36c$ (see text). (a) The observed luminosities, ages, and redshifts for the CSO 2s in the complete PR+CJ1+PW sample. The sample is divided into five redshift bins, as indicated in the legend. The trend of increasing luminosity with size is due to the steep luminosity function (see text). The large jumps in luminosity in the individual bins are all associated with jumps in redshift. (b) The distribution of luminosity with age. Black dotted line: the 44 CSO 2 objects with spectroscopic redshifts; blue dashed line: the 17 CSO 2 objects in the PR+CJ1+PW complete sample.

$P \sim 10^{24}$ W Hz^{-1} from $D \sim 10$ pc to $D \sim 500$ pc. There are several selection effects responsible for the lack of objects below $P \sim 10^{24}$ W Hz^{-1}, including spectral index and surface brightness sensitivity limits.

If we imagine reducing the flux densities of each of the objects in the PR+CJ1+PW sample of Figure 6(a), while their other properties are unaffected, they will each follow a track in the (P, D) plane indicated by the gray arrow attached to each object in Figure 7. For example, were we to reduce the flux density of each object by two orders of magnitude they would appear at the ends of the gray arrows in the positions shown by the corresponding faint symbols.

Note that this reduction in flux densities has populated part of the lower right quadrant of the (P, D) plane that previously

Table 4
Distributions of CSO 2.0s, CSO 2.1s, and CSO 2.2s in the (P, D) Plane

Class	Designation	Number Upper Left	Fraction Upper Left	Number Lower Right	Fraction Lower Right	Ratio of Fractions Upper/Lower
CSO 2.0	Early life	15	88%	2	12%	7.5
CSO 2.1	Midlife	5	33%	10	67%	0.50
CSO 2.2	Late life	1	8%	11	92%	0.09

Notes. The dashed line in Figure 1 is drawn to maximize the ratio of CSO 2.0s to CSO 2.2s in the upper left and to maximize the ratio of CSO 2.2s to CSO 2.0s in the lower right. The numbers of CSO 2.0s and 2.2s in the upper left and lower right is shown in this table. This shows an astonishingly clear bifurcation of the morphologies of CSO 2s in the previously unexplored (P, D) plane.
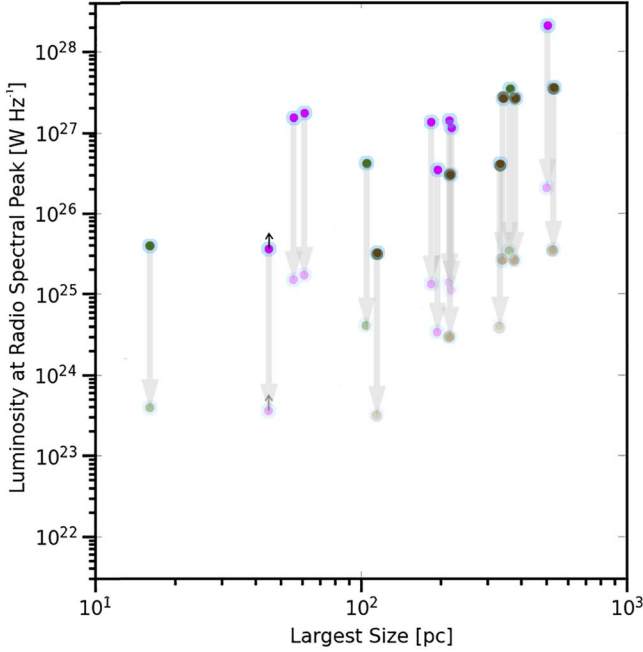

Figure 7. Observing complete samples to lower flux density limits. The 17 CSO 2s in the PR+CJ1+PW sample from Figure 1 are shown by the dark symbols. An identical sample in which each object is 100× weaker, such as might be discovered in a complete sample of radio sources with a 5 GHz flux density cutoff of 7 mJy, is shown by the light symbols at the ends of the gray arrows.

was unpopulated. Since CSOs must fade after their fueling ceases, there must be many low-luminosity CSOs with large sizes—i.e., with sizes in the ≈50 pc to ≈500 pc range. Were we to reduce the flux density limit below the lower limit of the PJ+CJ1+PW sample of $S_{5\,\mathrm{GHz}} = 700$ mJy, sources could then begin to populate the lower right quadrant of the (P, D) plane.

5.2. Evolution in the CSO 2 (P, D) Distribution

We have shown in Paper II that most ($\gtrsim 99\%$) CSO 2s constitute a distinct population of jetted AGN that is not related to other classes of jetted AGN, including CSS, PS, FR I, and FR II objects, and that the CSO 2 size distribution cuts off well below the 1 kpc CSO selection criterion. We now advance the hypothesis that most CSO 2s pass through all the stages of their evolution, from birth through death, as CSOs.

Before discussing CSO 2s per se, critical context is provided by the (P, D) diagram of FR II objects (Kaiser et al. 1997), and the "Baby Cygnus A" model discussed by Begelman (1996), who considers the equipartition case in which the particle and magnetic field energy densities are equal, resulting in simple

scaling relationships. Suppose the source luminosity P is dominated by an emission region with volume, V_{em}, and pressure, p_{em}. Then $P \propto p_{\mathrm{em}}^{7/4} V_{\mathrm{em}}$. V_{em} could be comparable to the volume of the entire cocoon or some smaller volume representing the lobes, which evolves inside the cocoon as the overall source grows. If the electrons reside in the emitting region for a time t_{em}, which could be the age of the source or shorter, then $p_{\mathrm{em}} \propto L_j t_{\mathrm{em}}/V_{\mathrm{em}}$, where L_j is the jet power. Thus $P \propto L_j^{7/4} t_{\mathrm{em}}^{7/4} V_{\mathrm{em}}^{-3/4}$. For a constant velocity of jet advance and constant L_j, and if $t_{\mathrm{em}} \sim \mathrm{age} \propto D$, the scaling is $P \propto D^{7/4} V_{\mathrm{em}}^{-3/4}$, i.e., $P \propto D^{-1/2}$ (assuming $V_{\mathrm{em}} \propto D^3$). Thus, in equipartition, and with constant jet power, the luminosity should decrease with increasing source size. The expectation for CSO 2s, therefore, might well be that the luminosity will drop as the size increases, but unfortunately, as discussed in Section 5.1, the (P, D) diagram of CSO 2s is dominated by the luminosity function.

Such a decrease in luminosity with increasing source size is evident among the FR II sources from the complete sample of 3CRR FR II radio sources studied by Kaiser et al. (1997), and becomes even more clear in the subsample with $z < 1$ studied by Godfrey & Shabala (2013) and Shabala & Godfrey (2013), where allowance is made for the intrinsic spread in the jet power L_j.

It should be remembered that both FR IIs and CSO 2s were small and weak at birth, and hence must have first appeared at the bottom left of the (P, D) diagram. This must then have been followed by a period of growth, when the jet power was increasing, in order for them to end up as high-luminosity radio doubles. In the case of the 3CRR FR IIs this occurs at $D < 8$ kpc (Kaiser et al. 1997). In the case of CSO 2s, the scale at which the P changes from increasing to decreasing with D remains to be determined. It is possible that in CSO 2s this occurs over the observationally accessible size range. Clearly, if this is the case, then the (P, D) relationship of CSO 2s will provide invaluable insight into both their own and FR II evolution. To exploit this possibility we need higher-resolution observations of CSO 2s.

The bifurcation in the morphologies of CSO 2.0s and CSO 2.2s, respectively shown by the yellow and blue regions of the (P, D) plane in Figure 1, prompted us to separate these two classes in the (P, D) plane approximately by drawing a dashed line from bottom left to upper right. The dashed line in Figure 1 has been drawn by eye to to maximize the ratio of CSO 2.0s above the line to those below it, and to maximize the ratio of CSO 2.2s below the line to those above it.

The numbers and fractions of CSOs 2s in the three subclasses are shown in Table 4. These are striking: we see that the fractions of CSO 2.0s and CSO 2.2s each flip by a factor ∼10 across this line, while the fraction of CSO 2.1s is

virtually unchanged. In Figure 1 the points in the upper left half of the figure are predominantly pink (CSO 2.0), while below it they are predominantly brown (CSO 2.2). This is clearly not a random effect, and we have shown in Section 5.1 that the only selection bias we have been able to conceive of goes in the opposite direction. For these reasons we hypothesize that the observed bifurcation of the CSO 2.0 and CSO 2.2 classes in the (P, D) plane is due to the evolution of CSO 2s, such that CSO 2.0→CSO 2.2, with a possible intermediate class of CSO 2.1, starting from an initial spread of ∼two orders of magnitude in peak luminosity.

If we now imagine the trajectory of an individual CSO 2s in the (P, D) plane, we see that the stages of growth and decay will match those of the (P, D) plane that are dominated by the pink and brown points, respectively. We suggest, therefore that CSO 2.0s (pink points) are objects that are increasing in D, and that CSO 2.2s (brown points) are objects that have slowed or stopped increasing in D. Given this scenario, and given that CSO 2.0s are on average significantly smaller than CSO 2.2s, we would expect the separation speeds, v_s, of the outer edges of the lobes straddling the nucleus to be higher in CSO 2.0s than in CSO 2.2s. We return to this point in the next section.

We note that the spread in CSO 2 luminosities at small D is at least a factor of 10^2, so it appears that the CSO 2s below the upper envelope in Figure 1 are a mixture of unevolved "early life," intermediate "midlife," and evolved "late-life" objects. This is seen clearly in the respective distributions of pink, green, and brown points.

Note that the CSO 2.1 sources exhibit features common to both CSO 2.0s and CSO 2.2s. In addition, as shown in Table 4 they are much more evenly distributed across the dashed line that demarcates the regions dominated by the CSO 2.0s and 2.2s. In both respects, they are intermediate in properties between the CSO 2.0s and the CSO 2.2s. It is for these reasons that we regard them as an intermediate step between CSO 2.0s and CSO 2.2s in the evolutionary sequence that we have suggested, and refer to them as "midlife." However, it remains possible that CSO 2.1s are not necessarily a midlife stage between CSO 2.0s and CSO 2.2s but may represent CSO 2s in asymmetric environments which causes one side to experience turbulence but not the other. Such asymmetry could be caused by an environment with an average velocity parallel with the CSO jet axis, inducing a high Reynolds number in one jet but not the other. Additionally the ambient density may not be symmetric about the core, leading to the observed differences in the two CSO 2.1 lobes. In any case, CSO 2.1s represent a middle-ground between CSO 2.0s and CSO 2.2s in appearance and physical properties. It should also be remembered that, for those CSO 2s whose axes are not very close to the plane of the sky, the two sides are seen at significantly different ages, and that this could also lead to one side having an apparent CSO 2.0 morphology and the other having an apparent CSO 2.2 morphology even if the two sides evolve identically.

5.3. Other Studies of Short-lived Compact Jetted AGN

There have been several studies of short-lived, as opposed to young, compact jetted AGN, which are often referred to as "fading" sources, characterized by steep spectra, indicative of the energy supply having been switched off, and a lack of hot spots or jets (Giroletti et al. 2005; Kunert-Bajraszewska et al. 2005, 2006, 2010; Giroletti 2008; Orienti et al. 2010, 2023; Callingham et al. 2015). Morphologically, therefore, these faders have the same characteristics as the CSO 2.2 objects we discuss in this paper. Many of the faders are low-luminosity objects, but the sample studied by Orienti et al. (2023) are high-luminosity objects, and several of them are A-class CSO candidates (see Paper I), and therefore highly likely to be bona fide CSOs. We have deep multifrequency VLBA observations of these objects in hand and are presently analyzing these.

Given the similarities of faders and CSO 2.2s, the question naturally arises as to why the CSO 2s discussed in this paper should not simply be combined with CSS and other PS objects and treated as a whole? Indeed, this would have been our own inclination had we not come across the unexpected sharp cutoff in CSO 2 sizes presented in Paper II. The statistical tests of Paper II show that there is only a one in ∼6000 probability that this cutoff is just a random result. What this means is that, while it is indeed possible that CSO 2s are drawn from the same population as the high-luminosity CSS sample, for example, studied by Orienti et al. (2023), this is highly unlikely. In the VIPS flat spectrum sample the bona fide CSO 2s show the same size distribution as do those from the PR +CJ1+PW sample discussed in Paper II. We also find that, in the PR+CJ1+PW CSO 2 sample, the numbers of steep spectrum objects ($\alpha < -0.5$) is approximately equal to the number of flat spectrum objects ($\alpha \geqslant -0.5$). We have proposed a program of VLBA observations of 332 CSS sources that will remove the spectral index cutoff of $\alpha \geqslant -0.5$ that defines the VIPS sample at present. Taking an extremely conservative estimate, by removing the flat spectrum cutoff from the VIPS sample, we will at least treble the number of CSO 2s in complete samples, to ∼50. If the ~14 steep spectrum VIPS CSO 2 objects we expect to find show the same size distribution as the 19 flat spectrum VIPS CSO 2 objects that we have in hand, then the level of significance of the size cutoff will increase to a p-value that will make an absolutely compelling case for the distinctive nature of the vast majority of CSO 2s. In addition, we note that by pushing the flux density limit on complete samples down to $S_{8.5\,\mathrm{GHz}} = 85$ mJy, including steep spectrum sources, one accesses the population of CSO 2s with spectral peaks at $\gtrsim 1$ Jy below 100 MHz.

6. The Ages of CSO 2s

Owsianik & Conway (1998) discussed the separation speed of CSO 0710+439 in detail, and found that the hot spot separation speed is $v_s = (0.354 \pm 0.041)c$ (assuming $H_0 = 71$ km s^{-1} Mpc^{-1}). From this and the size of the source they derived an age of 1100 ± 100 yr, and concluded that CSOs are young, by which, in our interpretation, they mean "short-lived". Gugliucci et al. (2005) carried out a detailed study of 20 CSOs for which they could estimate the ages, or lower limits to the ages. They measured kinematic ages that ranged from 20 ± 4 to 3000 ± 1490 yr. Combining their kinematic ages with those of Polatidis & Conway (2003) we find that seven out of 13 CSOs had kinematic ages below 500 yr. These authors also showed that the number of objects dropped off steeply for ages above ∼2000 yr, and concluded that CSOs could not evolve into FR I or FR II objects.

Polatidis & Conway (2003) considered the separation speed of the hot spots in eight of our bona fide CSO 2s. An unweighted average of their data yields $\overline{v_s} = (0.30 \pm 0.04)c$, for $H_0 = 71$ km s^{-1} Mpc^{-1}.

An & Baan (2012) studied a sample of 46 CSOs and CSO candidates. Of these 25 are among the bona fide candidates in

our sample selected in Paper I, and 24 have spectroscopic redshifts. Among the 24 bona fide CSOs with spectroscopic redshifts, 14 have measured separation speeds listed by An & Baan (2012), with speeds ranging between $0.08c$ and $0.96c$, and an average of $\overline{v_s} = (0.42 \pm 0.07)c$, and five have upper limits on the separation speed. If we use those upper limits as actual values of v_s, then we find $\overline{v_s} = (0.38 \pm 0.06)c$, whereas if we use $v_s = 0c$ for the five objects having upper limits then we find that $\overline{v_s} = (0.31 \pm 0.07)c$.

The evolutionary hypothesis we are proposing in this paper predicts that the CSO 2.0s should, on average, have higher separation speeds than the CSO 2.2s, which have likely slowed down. So we should be able to differentiate between CSO 2.0s and CSO 2.2s when considering CSO 2 separation speeds. Returning to the study of Polatidis & Conway (2003), we find that five of their 10 objects are bona fide CSO 2.0s, and for these their results yield a hot spot separation speed of $\overline{v_s} = (0.36 \pm 0.04)c$. In the An & Baan (2012) study there are nine CSO 2.0s with measured separation speeds and one with an upper limit. For the nine with measured separation speeds we find an average of $\overline{v_s} = (0.41 \pm 0.08)c$. If we use the single upper limit as actual value of v_s, we find $\overline{v_s} = (0.39 \pm 0.08)c$, whereas if we use $v_s = 0c$ for this object we find that $\overline{v_s} = (0.37 \pm 0.09)c$. For the remainder of this paper we assume that the mean separation speed of CSO 2.0s is $\overline{v_s} = 0.36c$, the average of the measured speeds of bona fide CSO 2.0 objects, and as a simplifying assumption we assume this separation speed for all CSO 2s during "early life."

The distribution of ages for the 44 CSO 2 objects for which we have spectroscopic redshifts, based on our measured largest angular sizes and assuming a constant hot spot separation speed of $0.36c$, is shown in Figure 6(b). In Paper II we showed that there are 17 bona fide CSO 2s with spectroscopic redshifts in the complete PR+CJ1+PW sample. The distribution of ages for these 17 CSO 2s, assuming a hot spot separation speed of $0.36c$, is shown in Figures 6(a) and (b). We note that the ages in both of these samples extend to ≈5000 yr, so we will use 5000 yr as the typical lifetime of the CSO 2s we are discussing.

In Figure 1 the CSO 2s in the complete sample are indicated by the light blue annuli around the points. We see that there are eight CSO 2.0s, three CSO 2.1s, and six CSO 2.2s. Thus, in the complete sample, the number of "early life" CSO 2.0s is about the same as that of "late-life" CSO 2.2s, and these are both significantly larger than the number of CSO 2.1s in the "midlife" phase. We conclude that CSO 2s spend roughly half their lifetimes in the "early life" phase, then pass through the "midlife" stage quickly, and spend about half their lifetime in the "late-life" phase. Since, as seen in Figure 1, both CSO 2.1s and CSO 2.2s have lower peak luminosities than CSO 2.0s of comparable size, we assume that the luminosity begins to drop off significantly once CSO 2s pass onto the " midlife" and "late life" stages.

It is difficult to measure the separation speeds in CSO 2.2s because they usually do not have bright hot spots at the outer edges of their outer lobes; however, in cases where they can be measured, they are found to be lower than for CSO 2.0s. For example, in the CSO 2.2 object J2355+4950 Polatidis & Conway (2003) measured a hot spot separation speed of $(0.12 \pm 0.03)c$, and the CSO 2.2 object J1945+7055 has a hot spot separation speed of $(0.024 \pm 0.006)c$ (Taylor et al. 2009). So the CSO 2.2 object J2359+4950 has a separation speed of about one-third that of the average CSO 2.0, whereas in the

CSO 2.2 object J1945+7055 the separation speed is about one seventh of the average CSO 2.0 separation speed.

In Figure 8 we compare the separation speeds in three CSO 2.0s with three CSO 2.2s, chosen to illustrate and explore the possible differences in morphology and separation speeds in these two classes. The separation speeds of the three CSO 2.0s are easy to determine because they have well-defined hot spots at the leading edges of their outer lobes. These are $(0.52 \pm 0.03)c$ for J0713+4349 (Polatidis & Conway 2003), $(0.24 \pm 0.015)c$ for J1247+6723 (Polatidis & Conway 2003), and $(0.19 \pm 0.03)c$ for J1511+0518 (An et al. 2012). The separation speeds of the CSO 2.2s are not easy to determine.

6.1. Separation Speed in the CSO 2.2 J0119+3210

Giroletti et al. (2003) have carried out a detailed study of the motion of components in J0119+3210. The speeds they derive for various components are shown in Figure 8(d), where we highlight components E1, E2, and W1 with red arrows. Giroletti et al. (2003) derived a significant separation speed between components E2 and W1. However, we see that component E1 is closer to the leading edge of the eastern lobe, and is moving almost due south. It is by no means clear to us, therefore, that the outer edges of J0119+3210 are actually separating, and that the measured relative motions do not apply to components moving along the jets.

6.2. Separation Speed in the CSO 2.2 J0131+5545

In Figure 8(e) we show the stacked 15 GHz image of Lister et al. (2020) and their measured velocities (red arrows) of the components C1, C8, and C5 relative to component C0, which they assume to be stationary in the rest frame of the central engine.

We propose here a different interpretation of these relative motions based on the morphologies of the CSO 2.2s J0111 +396, J0713+4345, and J2355+4950, which were studied in detail by R96 and Taylor et al. (1996), who showed that the nuclei are not coincident with bright components. Lister et al. (2020) have identified the nucleus of J0131+5545 as component C0. We suggest that, as with the above three CSO 2s, the nucleus in J0131+5545 is not coincident with the bright component C0. The jet axis is almost east–west, and, using the velocities measured by Lister et al. (2020), shown by the red arrows, we see that C1 is moving west with a speed of $(0.166 \pm 0.007)c$ relative to C0, while C5 is moving west with a speed of $(0.188 \pm 0.013)c$ relative to C0. Thus, the difference between C1 and C5 in westward motion relative to C0 is $(0.022 \pm 0.015)c$, consistent with zero. We suggest, therefore, that the nucleus lies between components C0 and C8, and that component C0 is moving eastward relative to both the nucleus and the two outer components, C1 and C5. Subtracting off the mean westward speed of $(0.177 \pm 0.015)c$ from the speeds derived by Lister et al. (2020), shown by the red arrows, we derive the speeds shown by the green arrows. On this interpretation, the outward motion of the lobes has stopped and the material at the outer edges of the lobes at C1 and C5 is moving almost normal to the jet axis and parallel to the interface of the lobe with the interstellar medium.

Note that on this alternative interpretation, the speeds of components C0 and C8, which we assume to straddle the central engine, are oppositely directed and of similar magnitude. Thus, while components C0 and C8 might
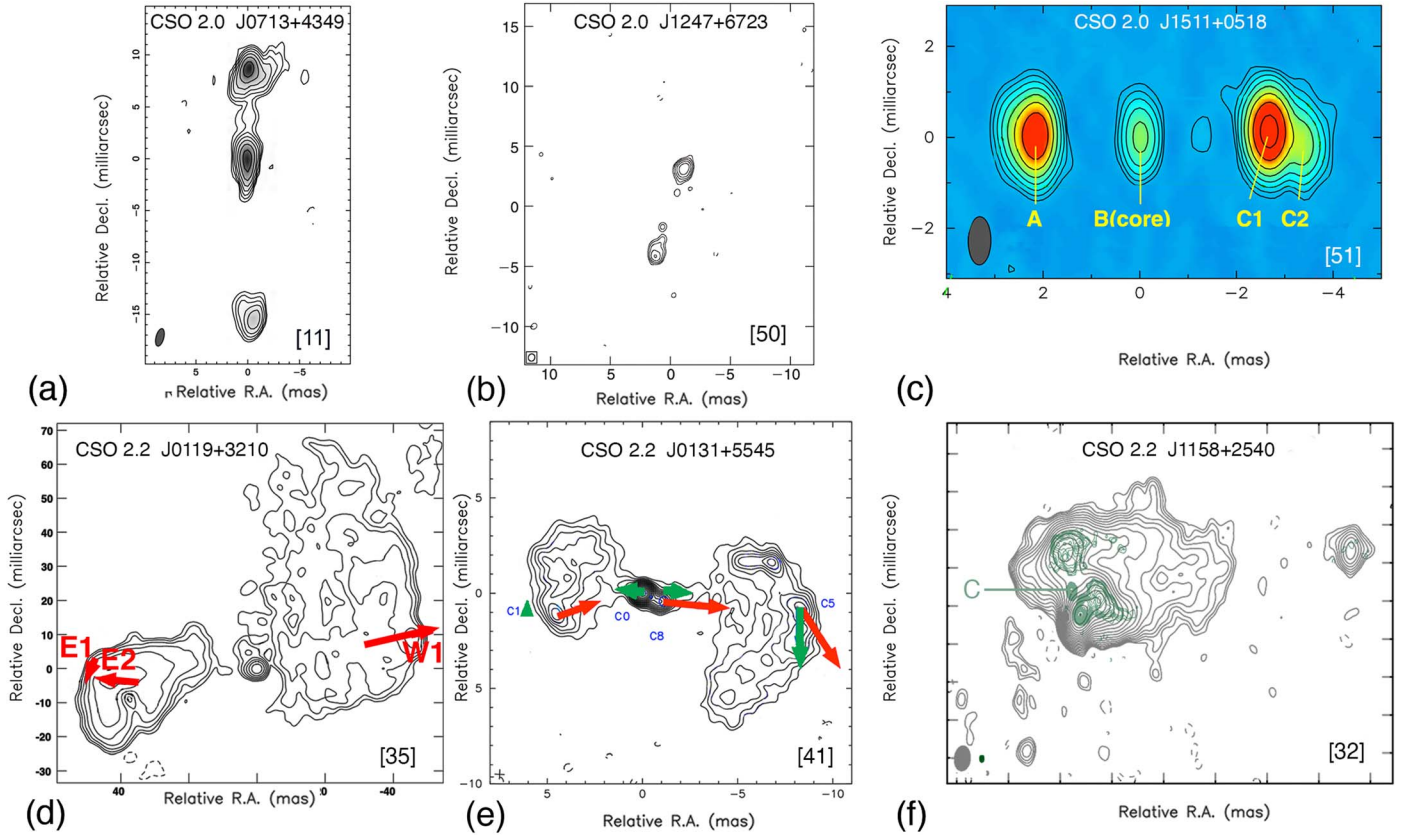
Figure 8. Three illuminating examples of CSO 2.0s and CSO 2.2s, selected to illustrate speed comparisons. CSO 2.0s: (a) J0713+4349 (Owsianik & Conway 1998), (b) J1247+6723 (Marecki et al. 2003), and (c) J1511+0518 (An et al. 2012). CSO 2.2s: (d) J0119+3210 (Giroletti et al. 2003), (e) J0131+5545 (Lister et al. 2020), and (f) J1158+2540 (Tremblay et al. 2008). The identification numbers of these six objects in Figure 1 are indicated in the [square] brackets.

represent a newly reborn CSO 2 and a new phase of activity, as proposed by Lister et al. (2020), in this paper we adopt the alternative explanation that these are simply high surface brightness regions of the jets, such as are commonly seen in CSO 2s. There are now more VLBI data from 2022 which may help to determine which interpretation of the motion is correct, and we are pursuing this analysis in greater detail, but it may well require VLBI astrometry to settle this question.

6.3. Separation Speed in the CSO 2.2 J1158+2540

In Figure 8(f) we have overplotted the 5 GHz map (gray contours) and the 15 GHz map (green contours) of J1158 +2540 observed by Tremblay et al. (2008). The core is seen clearly in the 15 GHz map, and is indicated by the letter "C." The CSO is aligned north–south, and Tremblay et al. (2008) found that the separation of the peaks in these components appears to be decreasing. This is very likely a result of the "dentist's drill" effect (Scheuer 1974; Perucho et al. 2019), but it does indicate a very slow speed of advance or even that the advance has stopped. From the morphology of this object, as seen clearly in the multifrequency maps of Tremblay et al. (2008), the advance does appear to have stopped while the source expands normal to the jet axis.

Summary and conclusion: thus, where we can measure them, the separation speeds of CSO 2.2s are on average less than those in CSO 2.0s. Our conclusion from this section is therefore that, based on the small number of objects for which measurements are available, the separation speeds of CSO 2s are consistent with the evolutionary hypothesis that CSO 2.0s

evolve into CSO 2.2s. Our hypotheses regarding the negligible separation speeds in J0119+3210 and J0131+5545 could be checked by astrometric VLBI.

7. The Energies of CSO 2s

In this section we estimate the radio emission energy requirements for CSO 2s. We first point out that the highest-luminosity CSO 2s in Figure 1—i.e., numbers 15, 16, 17, 18, and 19—are all highly asymmetric. It is likely that the emission from these objects is slightly relativistically boosted, and we therefore exclude them from our energy estimates. In our selection of CSOs we deliberately specify only that emission should be seen on both sides of the nucleus, without requiring that the emitting regions straddling the nucleus have comparable flux densities. We do this in order not to exclude CSOs with emission regions that are mildly beamed toward the observer from our sample. However, for the purposes of energy calculations, any objects suspected of having flux densities boosted even by factors of a few should clearly be excluded. From Figure 1, we see, therefore, that the most luminous CSO 2s suitable for the discussion of the energies of CSO 2s have luminosity $\sim 3 \times 10^{27}$ W Hz^{-1}.

R94 pointed out that the energy requirements for CSO 2s are $\sim 1\ M_\odot c^2$, and suggested that CSO 2s are formed via single star capture by a SMBH in an elliptical galaxy nucleus. R96 carried out a detailed study of PR CSO 2s, and estimated that the maximum energy requirement of CSO 2s is $\sim 20\ M_\odot c^2$. We show below that this estimate is a factor ~ 2–3 too high. Note that these energy estimates are based solely on the radio

Table 5
The Energies of CSO 2s Assuming Equipartition

CSO	$U_{\text{tot,eq}}$ from Maps ($M_\odot c^2$)	$U_{\text{tot,eq}}$ by Scaling ($M_\odot c^2$)
J0111+3906	0.57	0.68
J0131+5545	0.051	0.041
J1205+2031	1.5×10^{-4}	5.1×10^{-4}
J2355+4950	2.06	2.06[a]
Highest-luminosity CSOs	⋯	7

Note.
[a] By definition, since the others are scaled to J2355+4950 (see text). The energies determined from maps used the sizes and flux densities of all individual components, whereas the energies derived by scaling used generic lobe sizes, peak luminosities, and the relationship $U_{\text{T,eq}} \propto L_{\text{peak}}^{4/7} D_{\text{lobes}}^{9/7}$.

emission regions, and do not include any energy associated with the X-ray and γ-ray emission, nor do they include any energy expended in expanding into the surrounding medium.

R96 used multifrequency global VLBI observations with continuous 12 hr tracks, so their maps of the CSO 2s in the PR sample are of as high quality as is obtainable today with VLBI. Using their measured flux densities and angular sizes for the model-fitted components in J0111+3906 and J2355+4950, we have recalculated the R96 equipartition energies in these objects for the Lambda cold dark matter (ΛCDM) cosmology. The total equipartition energy requirements of J0111+3906 and J2355+4950 are given in Table 5.

The multifrequency global network VLBI maps of R96 provide the most accurate total equipartition energy estimate of a CSO 2 for J2355+4950. We therefore develop a scaling relation relative to J2355+4950 to provide a quick method of estimating the approximate equipartition energy for any CSO 2, for which one has the peak luminosity and the lobe size.

The total equipartition energy $U_{\text{T,eq}} \propto L_{\text{bol}}^{4/7} D_{\text{lobes}}^{9/7}$ (Blandford 1990; Longair 2011), where L_{bol} is the bolometric luminosity and D_{lobes} is the physical size of the radio-emitting region. Since L_{bol} scales with the peak luminosity, we see that $U_{\text{T,eq}} \propto L_{\text{peak}}^{4/7} D_{\text{lobes}}^{9/7}$. The peak luminosities of J0111+3906 and J2355+4950 are $1.54 \times 10^{27}\,\text{W Hz}^{-1}$ and $3.95 \times 10^{26}\,\text{W Hz}^{-1}$, respectively. Their mean lobe sizes are ~1.5 pc and ~47 pc, respectively. The equipartition energy values derived from the maps and model fitting of R96, adjusted to the ΛCDM cosmology, and by the scaling relation, are shown in Table 5.

We next consider the smallest and weakest CSO 2.2 in our sample, J0131+5545, which is shown in Figure 1 as #41, and in Figure 8(e). This is a "late-life" CSO 2 in which the energy supply has likely been switched off, or is rapidly decreasing, so that this object has very likely reached its energy peak. We use the observed values of flux densities and spectral indices from Lister et al. (2020), and an estimated mean lobe size from their maps of 4.5 mas, i.e., 33 pc (see Figure 8(e)), to obtain an observed total equipartition energy of 0.051 $M_\odot c^2$.

Given these observed measures of the total equipartition energies in CSO 2s, and the general agreement with the scaling relation, we can be confident that the maximum energy observed in CSO 2s may be estimated from the observed peak luminosity of $3 \times 10^{27}\,\text{W Hz}^{-1}$ and a mean lobe size of ~50 pc. Scaling this to the energy of J2355+4950, we find that the maximum total equipartition energy of CSO 2s is ~7 $M_\odot c^2$.

The least luminous CSO 2 in our sample is the CSO 2.1 object #43 in Figure 1, J1205+2031 (NGC 4093). This CSO 2 has been mapped with the European VLBI Network by Cheng et al. (2021). From their 5 GHz VLBI image we have estimated the angular sizes and flux densities of the two lobes, and, assuming a spectral index of $\alpha = -0.7$ for both lobes, we obtain a total energy of $\sim 1.5 \times 10^{-4}\,M_\odot c^2$ for this object.

We see, therefore, that the energies of CSO 2s observed thus far range from $\sim 1.5 \times 10^{-4}\,M_\odot c^2$ to $\sim 7\,M_\odot c^2$. This refers only to the energy associated with the radio-emitting regions. The total energies of CSO 2s, including the X-ray and γ-ray emission and the work done in expanding into the interstellar medium, likely increase the total energy by a factor of a few.

8. Multiple Epochs of Activity in CSO 2s

Baum et al. (1990) discovered evidence of a previous epoch of activity in the CSO 2 J0111+3906. Thus, in the course of the literature search described in Paper I, we also searched for any CSOs in which there was evidence of a previous epoch of activity. We identified these objects through gaps in the emission between the smaller-scale and larger-scale features, or through a dramatic reduction in surface brightness between the small-scale and the large-scale structure. Among the 79 bona fide CSOs we identified in Paper I, we found four bona fide CSO 2s showing evidence of previous epochs of activity, which are shown in Figure 9 and listed in Table 6. This suggests that the fraction of CSOs showing evidence of a previous epoch of activity lies in the range ~5%–10%.

A possible evolutionary model, in which multiple bursts of activity in CSOs in particular, and in compact jetted AGN in general, has been suggested by Reynolds & Begelman (1997). In their model the object shows bursts of activity lasting 10^4 yr spaced 10^5 yr apart. Czerny et al. (2009) considered the source evolution between repetitive outbursts and found that accretion rates small compared with the Eddington limit are required for short-duration outbursts ($<10^3$ yr). The maximum size of the radio source in their case was dependent on the initial jet power, duration of the outburst, and the properties of the interstellar medium. While these models may well apply in some CSOs, neither of them explains the sharp cutoff in the CSO 2 size distribution at ~500 pc that we found in Paper II.

We have calculated the energies of the larger components in these CSO 2s, which are listed in Table 6 using the methods of the previous section. As can be seen in the table, these energies exceed those of CSO 2s by at least a factor 30. It should be borne in mind that these relics of an earlier epoch of activity are no longer being fueled and thus the energies calculated here for the larger components are likely considerably lower than the total energy associated with the earlier active phase.

We have also measured the position angles of the innermost jetted features of the CSOs and compared these with the large-scale structure. The differences in position angle, ΔPA, are shown in Table 6. We note that in the case of the CSO 0108 +388, the jet bends from an initial $\Delta\text{PA} \sim 46°$ toward $\Delta\text{PA} \sim 0°$ in the northeastern jet, and a similar bend is seen in the southwestern jet. This could be due to pressure gradients in the interstellar medium of the host galaxy.

Because of their seemingly different origins, we conclude that there is no reason to reject the single star capture hypothesis on the basis of the evidence of previous epochs of activity in some CSO 2s. It is entirely possible that single star capture could have occurred in a galaxy that previously hosted
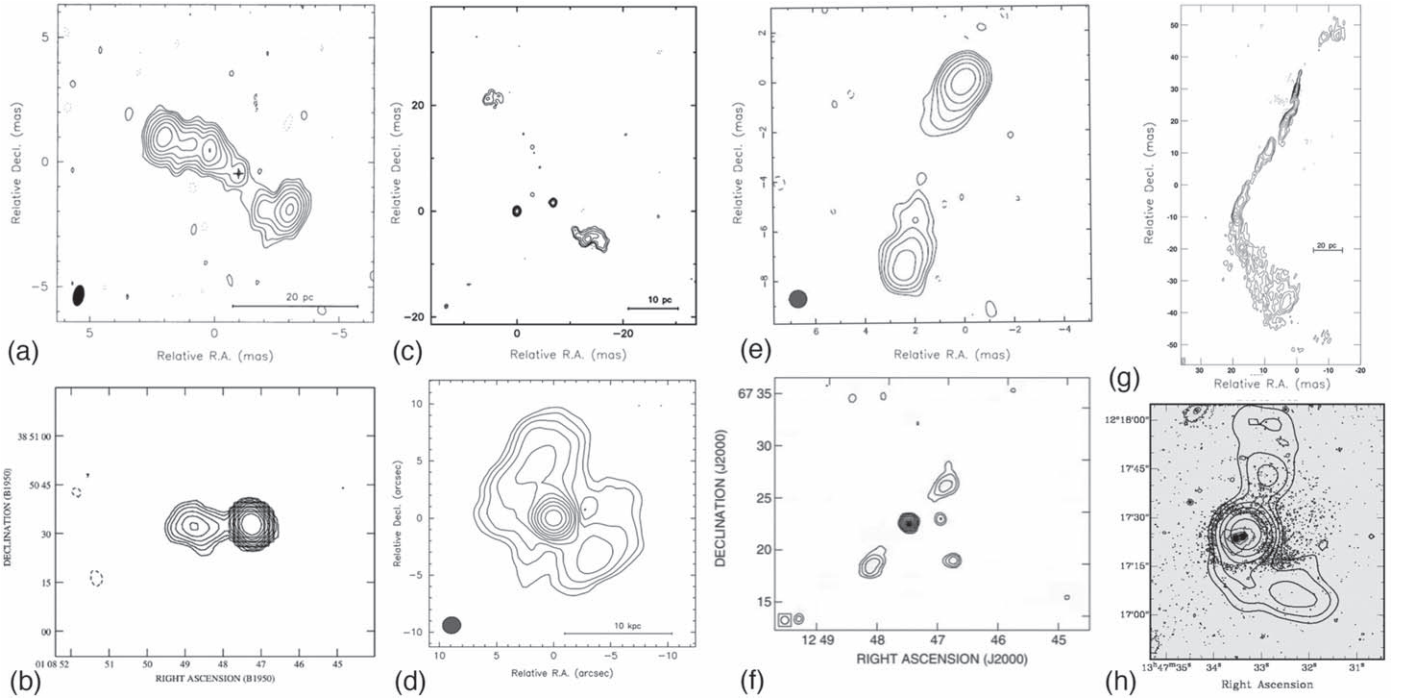
Figure 9. CSO 2s showing evidence of a previous epoch of activity. The top row shows parsec-scale radio maps, and the bottom row shows radio maps of the same objects at kiloparsec scales. 0108+388 (J0111+3906): (a) 15 GHz VLBI map (Taylor et al. 1996) and (b) 1.4 GHz Very Large Array (VLA) map (Stanghellini 2003). 0402+379 (J0405+3803): (c) 15 GHz VLBA map (Maness et al. 2004) and (d) 1.4 GHz VLA map (Maness et al. 2004). 1245+676 (J1247+6723): (e) 15 GHz VLBA map (Polatidis 2009) and (f) 1.4 GHz VLA map (Marecki et al. 2003). 1345+12 (J1347+1217): (g) 15 GHz VLBA map (Lister et al. 2003) and (h) 1.4 GHz VLA map (Stanghellini et al. 2005).

Table 6
CSO 2s Showing Evidence of a Previous Epoch of Activity

B1950 Name	J2000 Name	Redshift	CSO Size (pc)	Large-scale Size (kpc)	Large-scale Energy ($M_\odot c^2$)	ΔPA	References
0108+388	J0111+3906	0.669	56.0	80	~6,600	~46°	1, 2, 3
0402+379	J0405+3803	0.05505	44.4	16	~250	~1°	4
1245+676	J1247+6723	0.10700	23.6	1400	~2,700	~23°	5, 6, 7, 8, 9, 10, 11, 12, 13
1345+12	J1347+1217	0.122	215.4	140	~320	~5°	14, 15, 16, 17

References. (1) Baum et al. (1990), (2) Schoenmakers et al. (1999), (3) Conway (2002), (4) Maness et al. (2004), (5) White & Becker (1992), (6) Lara et al. (2001a), (7) Lara et al. (2001b), (8) Marecki et al. (2003), (9) Bondi et al. (2004), (10) Saikia et al. (2006), (11) Saikia et al. (2007), (12) Polatidis (2009), (13) An & Baan (2012), (14) Stanghellini et al. (1998), (15) Stanghellini et al. (2005), (16) Orienti & Dallacasa (2014), and (17) Pushkarev et al. (2017).

an AGN fueled through a different means. In this scenario, jet launching during the renewed period of activity may indeed be favored by the presence of a fossil, magnetized disk (Kelley et al. 2014). A weak jet was inferred for the nearby TDE ASASSN-14li (Pasham & van Velzen 2018), and a powerful relativistic jet was inferred for the candidate TDE VT J024345.70−284040.0 (Somalwar et al. 2023), both of which exhibited weak AGN activity prior to the TDEs.

9. CSO Host Galaxy Properties

The physical properties of CSO 2 host galaxies can inform our understanding of their formation channels. If CSO 2s are caused by discrete accretion events, like TDEs as hypothesized by this work, we may expect that their host galaxies would show specific features. For example, TDE properties are likely to correlate with the SMBH mass. In this section, we determine some of the physical properties of the CSO 2 host galaxies. We focus on the galaxy stellar and black hole masses. We briefly

and qualitatively comment on the presence of star formation and AGN activity.

We only consider the six CSO 2s for which we have high-quality archival optical spectra from Lawrence et al. (1996). Our CSO 2s are sufficiently distant that, in some cases, public survey photometry alone is not sufficient to set reliable constraints on the galaxy properties, so we conservatively focus on the subsample with spectra.

We measure host galaxy stellar masses by fitting the galaxy spectral energy distributions. We simultaneously fit the galaxy spectrum and public photometry. We adopt the spectra presented by Lawrence et al. (1996). We mask out any regions affected by nebular emission, sky lines, or standard star features. We perform optical and IR photometry for each of these objects using images from the Pan-STARRS and Wide-field Infrared Survey Explorer (WISE) surveys, respectively. We use the LAMBDAR code (Wright 2016) to obtain point-spread function (PSF)-matched aperture magnitudes, where the fiducial aperture is defined as 2.5× the Kron magnitude in the Pan-STARRS r-band image to define the fiducial aperture size.

Table 7
CSO 2 Host Galaxy Stellar and Black Hole Masses

CSO	$\log M_*/M_\odot$	$\log M_{BH}/M_\odot$
J0111+3906	$11.58^{+0.12}_{-0.16}$	9.35 ± 0.34
J0713+4349	$11.92^{+0.11}_{-0.10}$	9.76 ± 0.33
J1035+5628	$11.91^{+0.13}_{-0.12}$	9.74 ± 0.34
J1400+6210	$11.83^{+0.05}_{-0.08}$	9.65 ± 0.31
J2022+6136	$12.18^{+0.01}_{-0.01}$	10.06 ± 0.30
J2355+4950	$11.61^{+0.08}_{-0.20}$	9.41 ± 0.39

We then simultaneously fit the photometry and spectra for each galaxy using the bagpipes code (Carnall et al. 2018). We assume a τ-model star formation history, Calzetti et al. (2000) extinction, and a fixed metallicity. We do not include any AGN component. We include three additional components to enable the spectrum fit: we float the velocity dispersion, a second-order polynomial calibration vector, and a white noise component to account for any underestimated systematic uncertainties. We perform the fit using recommended procedures, and report the resulting stellar masses and 1σ uncertainties in Table 7. These masses are consistent within a factor of $\sim$0.5 dex with results obtained using just the photometry, and using simple mass-to-light ratio scaling relations (e.g., Bell et al. 2003); we are confident that the stellar masses are all $\log M_*/M_\odot \gtrsim 11$.

If the observed light includes a significant contribution from AGN emission, these masses are likely overestimated. We do not expect this to be the case, however, based on the optical spectra. All the galaxy optical spectra are broadly consistent with old elliptical galaxies. The optical spectrum for J0111+3906 looks like a typical quiescent galaxy. No strong [O III] emission or other emission lines are detected, and stellar absorption features consistent with old stars are visible. The remaining five CSO 2s show AGN-like emission lines (e.g., [O III] and [N II]), similar to Seyfert galaxies. No obvious broad components are detected. The stellar continuum is weak for most of these five, but absorption features consistent with old stars are weakly detected in a few. Given the lack of strong broad emission lines from this subsample or other features suggesting a bright AGN continuum, we do not expect that the stellar masses are hugely overestimated.

We can convert these stellar masses to black hole masses using the bulge mass–black hole mass relation from Kormendy & Ho (2013):

$$\frac{M_{BH}}{10^9\,M_\odot} = 0.49^{+0.06}_{-0.05}\left(\frac{M_{bulge}}{10^{11}\,M_\odot}\right)^{1.16\pm0.08};$$
$$\text{intrinsic scatter} = 0.29 \text{ dex.} \qquad (1)$$

We assume $M_* \approx M_{bulge}$, as is appropriate for elliptical galaxies. The resulting black hole masses are reported in Table 7. For galaxies with $M_* \gtrsim 10^{11}\,M_\odot$, the black hole masses are $M_{BH} \gtrsim 5 \times 10^8\,M_\odot$.

CSO host galaxies properties have previously been considered by Willett et al. (2010), who used Spitzer mid-infrared spectra and photometry to study the stellar populations, AGN activity, and black hole masses of an inhomogeneously selected sample of eight nearby CSOs ($z \lesssim 0.1$). Most of their CSOs show evidence for AGN activity and moderate star formation; one did not show detectable AGN or star formation emission.

This is qualitatively similar to the objects discussed in this section, although our data set is very different from that used by Willett et al. (2010) so we cannot perform a like-to-like comparison. They find black hole masses in the range $10^{8.2-8.8}$ $M_\odot$, which are significantly lower than our black hole masses, which are in the range $10^{9.3-10.1}$ $M_\odot$. This trend may be in part caused by the higher redshifts of our objects, which are in the range $z \approx 0.2$–0.7.

More likely, much of the difference may be caused by differences in the methodology used to compute the black hole masses. Willett et al. (2010) adopt a calibration that measured the relation between V-band bulge luminosities and black hole mass for AGN; we adopt the more recent and, arguably, more robust Kormendy & Ho (2013) calibration measured for classical bulges and elliptical galaxies. It is established that the Kormendy & Ho (2013) calibration is an upward revision of previous black hole mass relations, as discussed in that work. Moreover, as mentioned earlier, we are also using distinct data sets from Willett et al. (2010). A like-to-like comparison of our sample to Willett et al. (2010) would require a detailed and uniform study of the host galaxy properties of all these objects, which is beyond the scope of this work. Instead, we think it conservative to simply state that the CSO 2s from both our sample and that of Willett et al. (2010) tend to have similarly high black hole masses $\gtrsim 10^8\,M_\odot$.

10. The Birth Rates of CSO 2s and TDEs

We have seen in Paper II that the redshift distribution of our sample of 54 CSOs is strongly affected by selection bias. By considering only the PR+CJ1+PW complete sample, we can use the CSO 2 ages derived above to estimate the birth rate of CSO 2s. For these objects, from Figure 6 we see that the oldest CSO 2s are estimated to have ages of $\sim$5000 yr, assumed here to be the typical CSO 2 lifetime. In Figure 10 we show the redshift distribution for the PR+CJ1+PW complete sample as well as that of the CSO 2s in these complete samples. Apart from the outlier, J1227+3635, at $z = 1.975$, we see that the CSO 2s are approximately uniformly distributed in redshift out to a redshift of $z = 0.9$. It seems, therefore, that CSO 2s began to appear in appreciable numbers at a redshift of $z \sim 0.9$, i.e., about 7 Gyr ago.

We now make a very rough estimate of the birth rate of CSO 2s, which we refine in the next section. Given the lifetime of $\sim$5000 yr, this means that there is a probability of $\sim 5 \times 10^3/7 \times 10^9 \sim 7 \times 10^{-7}$ of seeing a particular CSO 2 at the present time, for the moment ignoring that fact that objects at high redshifts cannot be seen over the whole seven billion years because of the light travel time, which we calculate correctly in the next section. The comoving volume of the universe out to redshift $z = 0.9$ is $\sim$120 Gpc^3, so the space density of CSO 2s that is required to observe one CSO 2 at the present time is $\sim 1/(7 \times 10^{-7} \times 120)$ Gpc$^{-3} = 1.2 \times 10^4$ Gpc^{-3}, and the birth rate, given that we observe 16 CSO 2s out to redshift $z = 0.9$, is $\sim 16 \times 1.2 \times 10^4/7 \times 10^9$ Gpc^{-3} yr$^{-1} \sim 3 \times 10^{-5}$ Gpc^{-3} yr^{-1}.

10.1. The Tip of the Iceberg

The birth rate of $\sim 3 \times 10^{-5}$ Gpc^{-3} yr^{-1} is based on the PR+CJ1 and PW samples, which are complete down to 0.7 Jy at 5 GHz and 1.5 Jy at 2.7 GHz, respectively. Because of the steepness of the luminosity function, we are only sampling the most luminous CSO 2s in each redshift range. The samples are
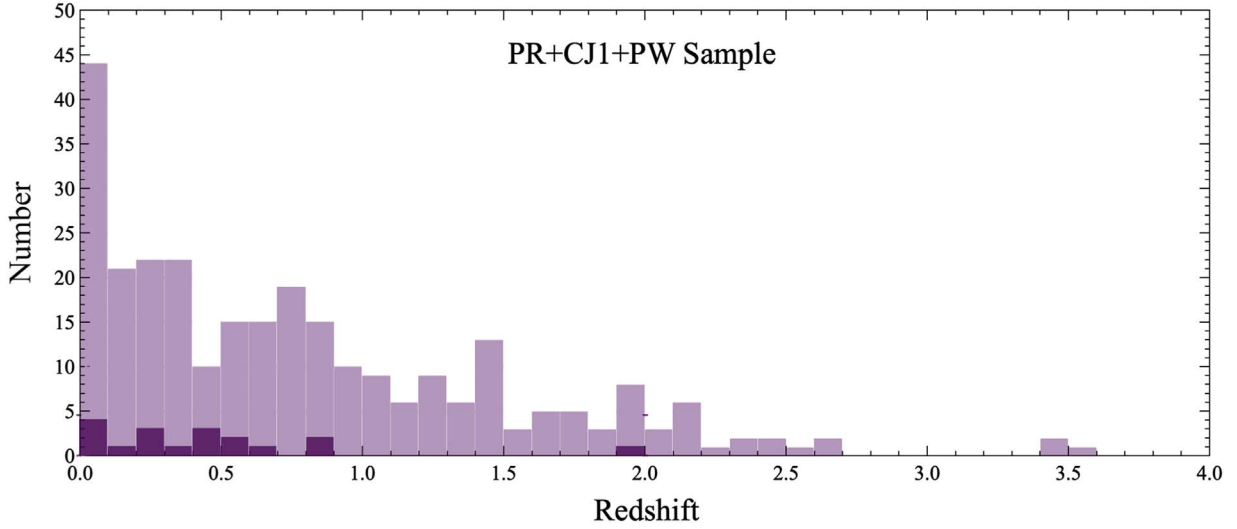
Figure 10. The redshift distribution for the PR+CJ1+PW complete sample. The light shaded distributions show the complete sample. The dark shaded regions show the CSO 2s. Note that these distributions are not stacked vertically, so the values on the ordinate represent the total numbers of sources and the numbers of CSO 2s in each sample.
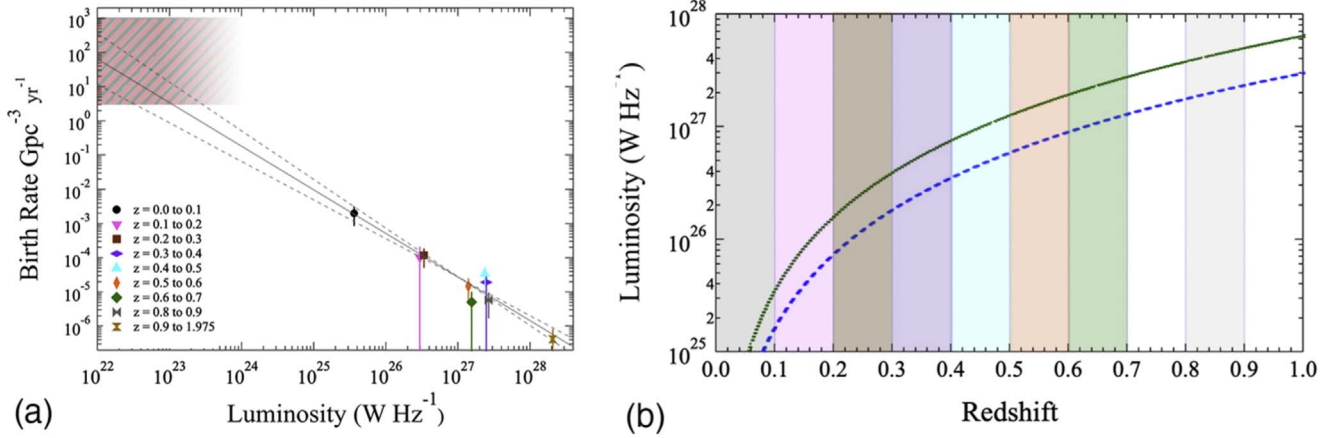

Figure 11. Dependence of birth rates of CSO 2s in the complete PR+CJ1+PW samples on luminosity. (a) The birth rates vs. luminosities of CSO 2s are shown by the plotted points. The solid gray line is the least-squares fit to the points and the dashed lines show the $\pm 1\sigma$ ranges of the fit. The approximate range of birth rates for jetted TDEs is shown by the red and gray hatched region (see text). (b) The luminosity cutoffs of the PW (green line) and PR+CJ1 (blue dashed line) samples. The colors of the panels are faded versions of the colors in the different redshift ranges shown in panel (a).

therefore luminosity limited depending on the redshift of the CSO 2s. We have divided 16 CSOs into redshift bins of width $\Delta z = 0.1$ out to a redshift of $z = 0.9$, as shown in Figures 11(a) and (b), and then one bin covering $0.9 < z \leqslant 1.975$ to accommodate the lone CSO 2 at $z = 1.975$ (J1227+3635). The colors of the panels in Figure 11(b) indicate $\Delta z = 0.1$ bins and are diluted versions of the colors show in Figure 11(a). We calculate the CSO 2 luminosities in Figure 11(b) as the average luminosity in each bin. All bins show luminosity variations of a factor <3, so we do not expect this choice to affect our results significantly. In future work, with a larger CSO 2 sample, we will perform a rigorous likelihood analysis to calculate the CSO 2 luminosity function and birth rate; based on preliminary tests applying such a framework to the sample in this work, we do not expect that result to be significantly different from the one found here using this simplified calculation, so we choose to adopt this simpler, more intuitive, methodology.

The luminosity cutoffs corresponding to 1.5 Jy (the PW sample) and 0.7 Jy (the PR+CJ1 sample) are shown as a function of redshift by the green and blue dashed curves in

Figure 11(b), respectively. We see that the three CSO 2s we have observed in the redshift range $0.0 < z < 0.1$, which all have luminosities below 4×10^{25} W Hz^{-1}, would have fallen below the flux density limits in the higher-redshift bins. Similarly, the four CSO 2s we have observed in the redshift range $0.1 < z < 0.3$, which all have luminosities below 4×10^{26} W Hz^{-1}, would have fallen below the flux density limits in the higher-redshift bins. It is clear, therefore, that in these flux density–limited complete samples we are seeing only the tip of the iceberg, i.e., only the most luminous CSO 2s in each redshift range.

The solid line in Figure 11(a) is a least-squares fit to the log (birth rate) versus log(luminosity) data of the CSO 2s, and has a slope of -1.27 ± 0.15. The upper and lower 1σ limits on the slopes are indicated by the dotted lines in Figure 11(a).

The birth rate analysis may offer a prediction of the finite-lifetime scenario for CSO 2s. Multiepoch wide area radio surveys such as the VLA Sky Survey (VLASS; Lacy et al. 2020), Deep Synoptic Array (DSA2000; Hallinan et al. 2019), and those made with Square Kilometre Array pathfinders (e.g.,

Murphy et al. 2013) should be able to detect the births of CSO 2s as radio transients. For example, VLASS is sensitive to $\sim$1 mJy transients that rise over the 6 yr between epochs (e.g., Dong et al. 2021). To a distance of 1 Gpc, where the VLASS sensitivity limit corresponds to 1.2×10^{23} W Hz^{-1}, the survey should observe the birth of $\sim$50 CSO 2s. Likewise, transient searches performed by comparing the FIRST survey to VLASS are sensitive to $\sim$1–2 decade-timescale transients, and could observe the birth of CSO 2s. D. Z. Dong et al. (2023, in preparation) have identified all FIRST versus VLASS transients hosted by galaxies within 200 Mpc, and found $\sim$2 events that are consistent with being young CSO 2s. This is consistent with expectations: given the selection criteria used in D. Z. Dong et al. (2023, in preparation), we would expect $\sim$one new CSO 2 to be detected. Significant caveats to these predictions are that the ultimate luminosity of a CSO 2 is likely not attained near birth, and, as, we see in Figure 6(a), there might be a correlation between the (peak) luminosity of a CSO 2 and its age. Nonetheless, time-domain radio surveys provide the opportunity to characterize the processes driving the births of powerful radio AGN.

10.2. The Birth Rates and Radio Luminosities of Jetted TDEs

The birth rate of jetted TDEs has been shown to be weakly constrained to be $(0.003–1) \times$ the total TDE rate by De Colle & Lu (2020), which implies a birth rate of 3–1000 Gpc^{-3} yr^{-1}. This range is indicated by the red and gray hatched region in Figure 11(a). The luminosity of jetted TDEs can be estimated roughly from the observed maximum radio flux density at multiple wavelengths of $\approx$10 mJy for AT2022cmc (Andreoni et al. 2022): in a source at rest emitting isotropically, observed distantly with a flux density S', and in which the jet is continuous, the observed flux density is $S = \mathcal{D}^{2-\alpha} S'$ (Scheuer & Readhead 1979), where $\mathcal{D}$ is the Doppler factor:

$$\mathcal{D} = \frac{1}{\Gamma(1 - \boldsymbol{\beta} \cdot \boldsymbol{n})}, \qquad (2)$$

and $\Gamma = (1 - \beta^2)^{-1/2}$ is the Lorentz gamma factor.

Here we use $\Gamma = 12$, as estimated for AT2022cmc (Andreoni et al. 2022), and we assume the angle between the jet axis and the line of sight is $\theta \sim 1/\Gamma$, at which angle $\Gamma = \mathcal{D}$ so that the luminosity for off-axis TDEs is reduced by the factor Γ^2, assuming spectral index $\alpha = 0$. We have therefore reduced the peak flux density of AT2022cmc of $\sim$10 mJy observed in this on-axis jetted TDE to 0.07 mJy, which corresponds to a peak luminosity of 6.5×10^{23} W Hz^{-1} for the unbeamed jetted TDE for comparison with the luminosities of the (unbeamed) CSO 2s. This upper cutoff is indicated by the fading red and gray hatched bar in Figure 11.

11. A Hypothesis Regarding Fueling of CSO 2s and FR IIs

The SMBH in the central engines of FR II objects, such as Cygnus A (Figure 12 bottom panel), are continuously fueled for $\sim$10^7 yr (Carilli et al. 1991). We propose the hypothesis that CSO 2s (Figure 12, top panel) are continuously fueled for timescales of years to $\sim$5 $\times$ 10^3 yr, and that something truncates the fueling of CSO 2s after this time, otherwise they would, no doubt, go on to become FR IIs. This fueling disparity between CSO 2s and FR IIs has no obvious explanation.

Paper II provides compelling evidence for a sharp cutoff in size of CSO 2s at $\approx$500 pc. This is consistent with our interpretation of the evolutionary sequence proposed in this paper, in the sense that the evolutionary sequence, which is based on morphology alone, without reference to the sizes, suggests that an upper size cutoff must exist for CSO 2s. This relationship between evolution and size cutoff can be seen clearly in Figure 13, where the CSO 2.0s are generally smaller than the CSO 2.2s and of greater luminosity in the same size range.

As can be seen from Figure 1 and Fanaroff & Riley (1974), the luminosities of CSO 2s and FR IIs (Fanaroff & Riley 1974) cover the same range from $\sim$10^{25} to $\sim$10^{28} W Hz^{-1}. Note that these CSO 2 luminosities are at the peak frequency, which, as can be seen in Paper I, in almost all cases lies between 100 MHz and 10 GHz. However, the total energies of the most luminous CSO 2.0s are approximately 2×10^4 times less than the total energy of Cygnus A ($\sim$7 $\times$ 10^{58} erg), which we have calculated based on the flux densities, angular sizes, and spectral indices for the different components of Cygnus A given by Hargrave & Ryle (1974). So it appears that had CSO 2s simply continued at the same luminosity for $\sim$10$^4 \times$ longer, they would have evolved into FR IIs, like Cygnus A, with comparable kiloparsec sizes and total energies.

Clearly, in CSO 2s there is a physical process operating that does not operate in FR II objects. This unknown physical process terminates CSO 2 development as jetted AGN after a few tens of years up to 5000 yr or so. As pointed out in R94, one simple way to accomplish this might be through a single isolated fueling event, such as stellar capture.

The fact that CSO 2s only began to appear in significant numbers about seven billion years ago, at redshift $z = 0.9$, may support the hypothesis of a single isolated fueling event, because prior to that time there was significantly more galaxy merging providing fueling to AGN, which would drown out any effects due to the capture of a single star. On the other hand, galaxy mergers can also enhance the TDE rate (Pfister et al. 2019), and partial stellar disruptions may also play a significant role in fueling SMBHs of the mass considered herein with order-unity duty cycle (MacLeod et al. 2012). However, self-consistent modeling of TDE rates with the SMBH mass function and star formation histories (Kochanek 2016) robustly predicts that TDE rates drop precipitously with redshift for all SMBH masses, consistent with the redshift distribution of the CSO 2 population. Further, if CSO 2s of the luminosities exhibited by our sample require SMBHs as massive as those inferred above, evolution in the SMBH mass function also supports the late appearance of the CSO 2 population.

The highly statistically significant cutoff in the size of CSO 2s discussed in Paper II cannot be due to episodic fueling, because that would not produce the observed sharp cutoff in the numbers of CSO 2s at around 500 pc. Random fueling could produce a slow drop-off in the numbers of CSO 2s, but not the abrupt change that is observed.

12. CSO 2s and TDEs

This cutoff is clearly telling us something important about the origins and nature of this unique class of jetted AGN. It should not, of course, be assumed that all CSO 2s have the same origin, but Occam's razor should apply and we should consider multiple origins only when demanded by the
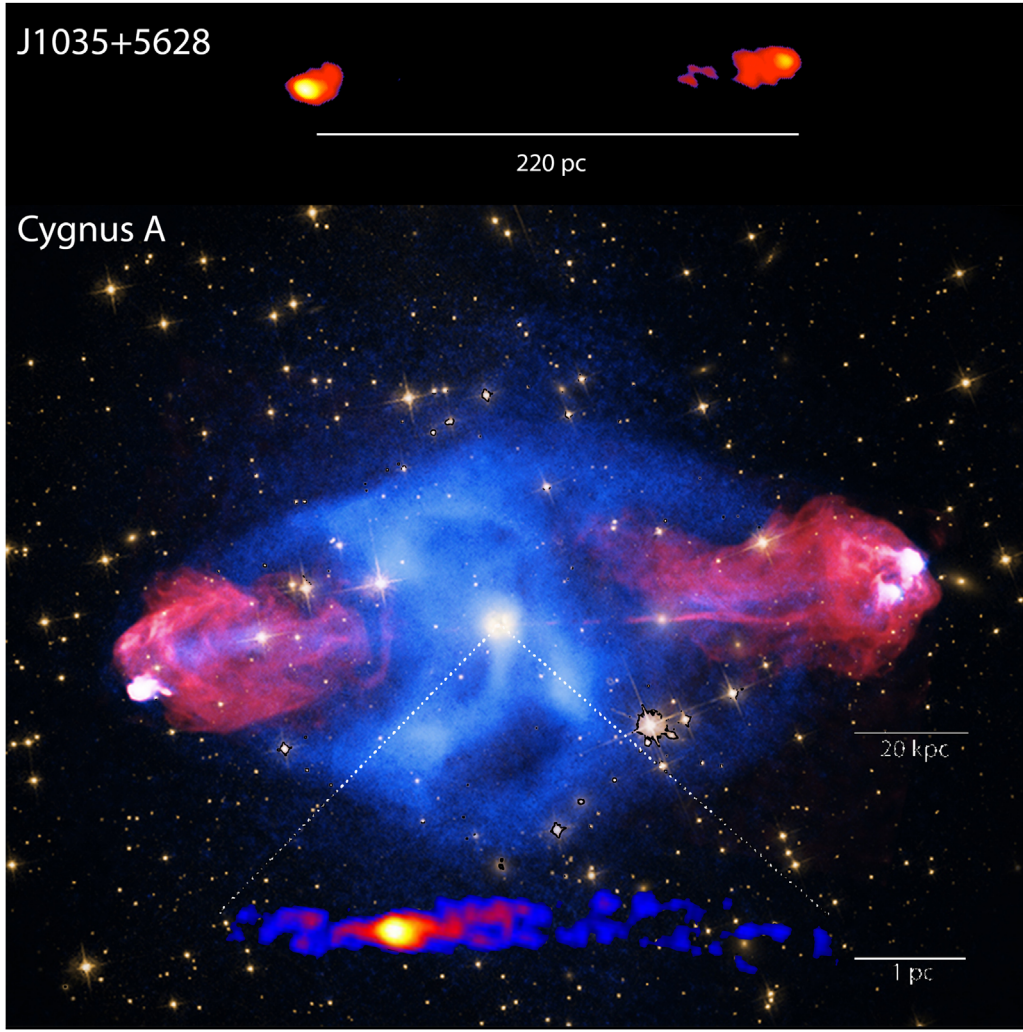
Figure 12. Upper panel: VLBA image of the CSO 2.0 object J1035+5628 (Taylor et al. 2000). Lower panel: composite Cygnus A image from Blandford et al. (2019) in which the radio emission is shown in red and the X-ray emission is shown in blue, all overlaid on the optical image. The VLBI Cygnus A inset is from Boccardi et al. (2017). Although the ranges of luminosities of CSO 2s and FR IIs are indistinguishable, only $\lesssim 1\%$ of CSO 2s go on to form FR IIs. The remaining $\gtrsim 99\%$ disappear before reaching a size of ~ 500 pc and an age of ~ 5000 yr.

phenomenology. Since we are not able, as yet, to make a compelling case for the origin we here investigate different possibilities.

In the following, we first demonstrate the plausibility of some CSO 2s being formed through TDEs, as first suggested by R94. We then compare the CSO 2 birth rate with the expected rate of TDEs for the SMBH masses we derive above, and show that it is possible that all CSO 2s represent TDEs. We finish by identifying certain predictions of the TDE hypothesis for CSO 2s.

12.1. CSO 2s Powered by TDEs

TDEs occur when stars pass within the tidal radius, R_T, at the pericenter of their orbit around an SMBH. The tidal radius depends primarily on the stellar radius, R_*, the stellar mass, M_*, the SMBH mass, M_{BH}, and on the internal stellar structure. Neglecting the effects of SMBH spin, the ratio of R_T to the Schwarzschild radius is (e.g., MacLeod et al. 2012):

$$R_T / R_S \approx 1.6 m_{*,3}^{-1/3} m_{BH,9}^{-2/3} r_{*,10}, \qquad (3)$$

where $m_{*,3} \equiv M_*/3\ M_\odot$, $r_{*,10} \equiv R_*/10\ R_\odot$, and $m_{BH,9} \equiv M_{BH}/10^9\ M_\odot$. Stars that are not massive enough or too compact will be disrupted within the event horizon, and the results will thus be invisible.

The characteristic timescale on which post-TDE bound material falls back onto the SMBH is the fallback timescale, t_{fb}. Defining β as the ratio between the stellar dynamical timescale, $\sqrt{R^3/GM_{BH}}$, and the pericenter passage timescale (R_p/v_p, where R_p is the pericenter radius and v_p is the corresponding stellar velocity), the fallback timescale is given by Rees (1988):

$$t_{fb} \approx 37\beta^{-3} m_{BH,9}^{1/2} m_{*,3}^{-1} r_{*,10}^{3/2} \text{ yr.} \qquad (4)$$

Encounters with small impact parameters will have $\beta \gg 1$. The fallback timescale is defined in terms of accretion of the most bound material. Following this time, the accretion rate is expected to taper according to a power-law decay, with an index of $-5/3$ expected for a flat distribution of disrupted material in orbital energy space. Hydrodynamical simulations of TDEs find rough agreement with this scenario for a variety of stellar types, although the power-law slopes of the accretion rate decay depend sensitively on the nature of the disruption
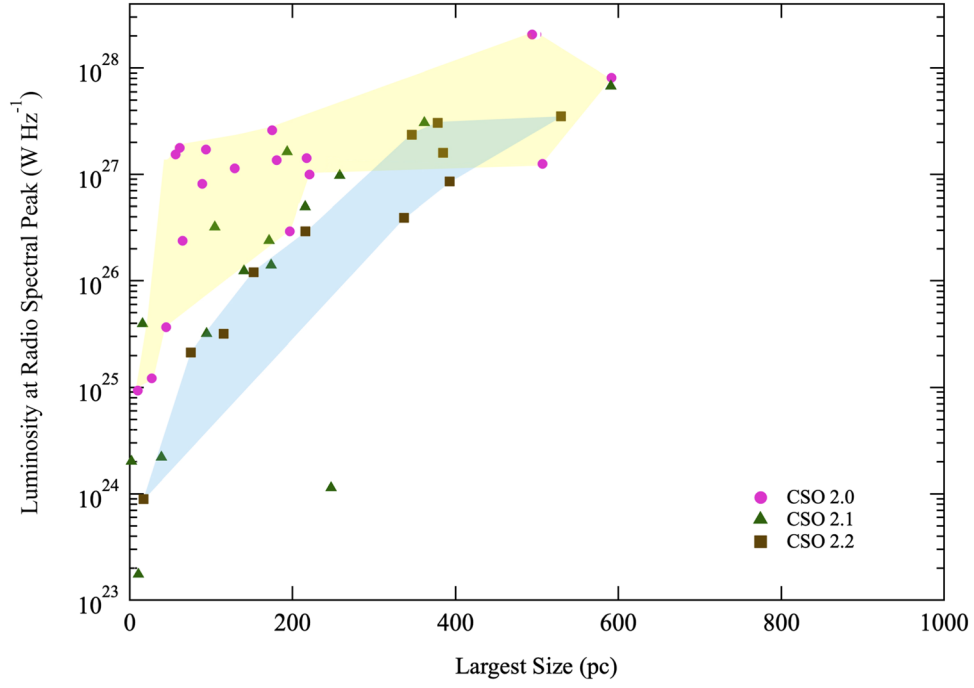
Figure 13. CSO 2s in the (P, D) plane: pink circles—CSO 2.0s; green triangles—CSO 2.1s; brown squares—CSO 2.2s. The faint yellow and blue regions show the areas of the (P, D) plane occupied by the CSO 2.0 and CSO 2.2 objects, respectively. In this log-linear plot the size cutoff and evolution from CSO 2.0 to CSO 2.2 is more clear than in the log–log plot of Figure 1. Note the absence of any CSO 2s in the size range 600–1000 pc. This shows the abrupt cutoff in CSO 2 size well before reaching the nominal cutoff imposed by the CSO size selection criterion, as discussed in detail in Paper II.
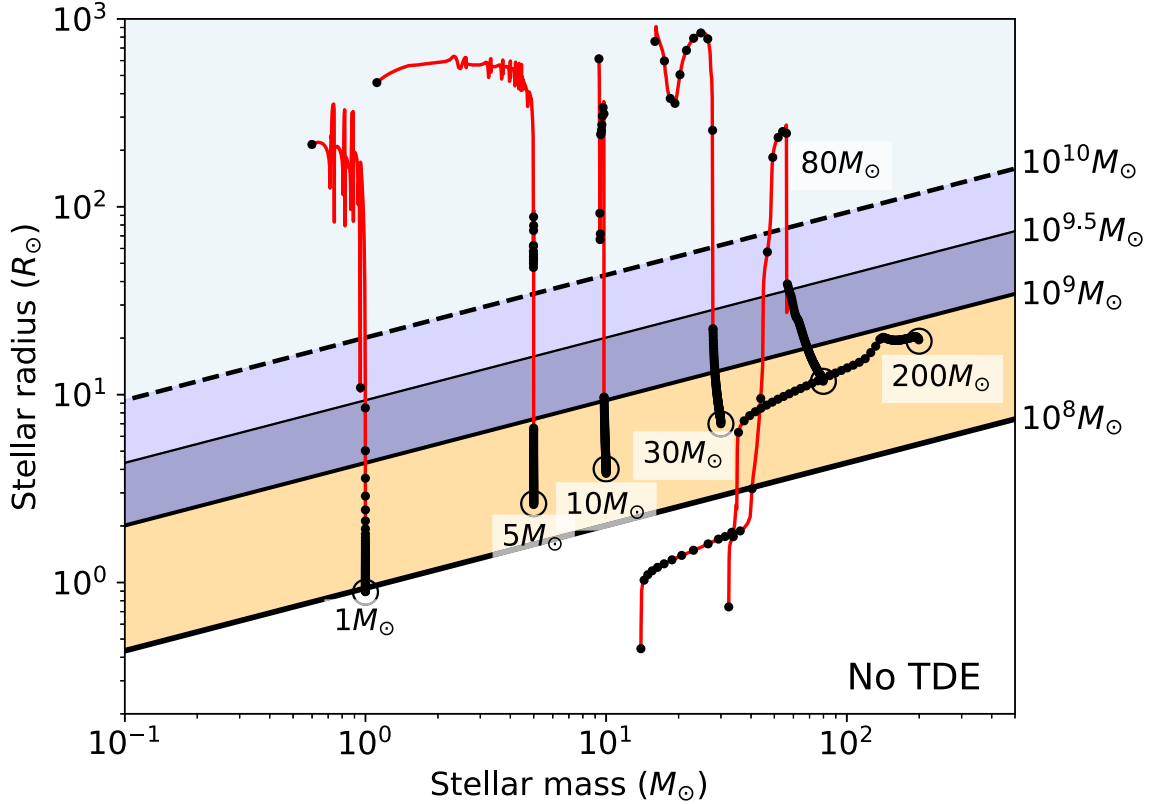
Figure 14. Regions in the stellar radius–mass space where disruption is possible outside the event horizons of SMBHs of different masses. The lower limits, corresponding to $R_T/R_S = 1$ for SMBHs of various masses as labeled, are shown as lines, and the shaded area indicates where disruption is observable. We also show evolutionary tracks for solar-metallicity stars of 1 $M_\odot$, 5 $M_\odot$, 10 $M_\odot$, 30 $M_\odot$, 80 $M_\odot$, and 200 $M_\odot$ interpolated from the MESA Isochrones and Stellar Tracks (MIST; Dotter 2016). The stars are evolved from the zero-age main sequence (indicated as open circles) either to the end of thermal pulsations on the asymptotic giant branch, or to supernova. Each track is garnished with black dots that indicate intervals of $1/100$ of the lifetime of each star. For example, a 1 $M_\odot$ star can be disrupted by a $10^9 M_\odot$ SMBH for $\sim 4/100$ of its lifetime.

(e.g., impact parameter) and the stellar structure (e.g., MacLeod et al. 2012; Guillochon & Ramirez-Ruiz 2013; Norman et al. 2021). The maximal accretion rate can be estimated as the ratio $M_*/t_{\rm fb}$:

$$\dot{M}_{\rm max} \approx 0.08\beta^3 m_{\rm BH,9}^{-1/2} m_{*,3}^2 r_{*,10}^{-3/2} \; M_\odot \; {\rm yr}^{-1}. \qquad (5)$$

Only massive and/or post–main-sequence stars can be observably disrupted by SMBHs of the $\gtrsim 10^9 \; M_\odot$ masses inferred for the CSO 2 sample herein. Figure 14 shows the regions of the stellar radius–mass space where disruption is possible, together with sample stellar evolutionary tracks. The figure indicates that disruption is not possible for the most massive CSO 2 SMBHs for most of the lifetimes of most stars. We note however that the treatment of the extended envelopes of the most massive ($\gtrsim 100 \; M_\odot$) stars in the Modules for Experiments in Stellar Astrophysics (MESA; Paxton et al. 2018) may not be entirely accurate based on observations of WNh stars in the Small Magellanic Cloud (Gräfener 2021). The precise amount of mass donated to an SMBH in either a full or partial disruption (e.g., of just an envelope), and whether or not disruption occurs for different β and SMBH spins, requires numerical simulations. For example, MacLeod et al. (2012) performed detailed simulations of the disruption of stars with masses up to $5 \; M_\odot$ and showed that $>10^9 \; M_\odot$ SMBHs could only disrupt such stars in post–main-sequence phases. In general, the maximal accretion rate will be much less than the Eddington rate.

The energetics and timescales of CSO 2s are consistent with expectations for TDEs around the most massive SMBHs. Any given TDE around a $\gtrsim 10^9 \; M_\odot$ SMBH is much more likely to be a post–main-sequence star of one to a few solar masses, rather than a $\gg 10 \; M_\odot$ star. Although the $80 \; M_\odot$ star in Figure 14 spends over half its lifetime in a region where a TDE is possible, its lifetime is only ~ 4 Myr, and the $5 \; M_\odot$ star spends ~ 10 Myr in the TDE region of the plot. We now consider the minimum stellar mass for which a TDE can power a CSO 2 jet, which in a fiducial case requires $\sim 1 \; M_\odot c^2$. This can be approximately equated to the total accreted mass (see below) for the sub-Eddington mass supply rates under consideration, and for a rapidly rotating SMBH. We note that although the relativistic TDE Swift J1644+57 converted just $\sim 1\%$ (Cendes et al. 2021) of the rest energy of the approximately solar-mass disrupted star (Tchekhovskoy et al. 2014), such events are entirely different from CSO 2s given the initial super-Eddington accretion phase and prompt jet launching. Then, as approximately a third of the mass of an evolved star will be accreted (MacLeod et al. 2012), the fiducial scenario assumed above of a $3 \; M_\odot$ horizontal-branch star with a radius $10 \; R_\odot$ is energetically reasonable for a CSO 2. The rise and decay timescales of the accretion will be less than about 100 yr. A somewhat more massive star in an AGB phase (AGB star disruptions contribute a smaller fraction of the envelope mass to accretion) disrupted by a $10^{9.5} \; M_\odot$ SMBH can easily accommodate the $\sim 10^3$ yr durations inferred for the CSO 2s considered here.

12.2. Comparing the CSO 2 and TDE Rates

The CSO 2 birth rate of $\sim 3 \times 10^{-5} \; {\rm Gpc}^{-3} \; {\rm yr}^{-1}$ can be compared with the empirical TDE rate of $\sim 10^3 \; {\rm Gpc}^{-3} \; {\rm yr}^{-1}$ found by van Velzen (2018). A direct comparison is fraught with uncertainty.

1. First, the initial mass function (IMF) in nuclear regions, and in particular for stars in CSO 2 host galaxies on radial orbits, may be substantially different to the field IMF in the Galaxy. For example, Nayakshin & Sunyaev (2005) have argued that the IMF in the centers of galaxies is top-heavy by at least a factor 10. Maness et al. (2007) have presented compelling evidence for a long-standing top-heavy IMF in the central parsec of our own Galaxy based on the work of Paumard et al. (2006). They conclude that the model that fits the observations best has IMF slope $x = -0.85$, in comparison with the Salpeter (1955) IMF slope of $x = -2.35$. More recent observations of a larger sample have shown the IMF in the center of our Galaxy to be extremely top-heavy with $x = -0.45$ (Bartko et al. 2010). There is indeed evidence for the preferential disruption of $\gtrsim 2 \; M_\odot$ stars in nearby TDE hosts (Mockler et al. 2022). The uncertainty in the IMF needs to be taken into account, as does the prospect of evolved-star disruptions contributing significantly to the putative CSO 2 TDEs.

2. Second, the fraction of disruptions that result in radio emission from relativistic jets is largely unconstrained by observations thus far. Although it is possible to consider the fraction of relativistic TDEs in relation to the overall TDE population (e.g., Andreoni et al. 2022), these relativistic TDEs are potentially very different to the TDEs that could correspond to CSO 2s. The inferred accretion rates are disparate by more than four orders of magnitude, and the selection of impact parameters, SMBH spins, and preexisting AGN activity is unknown. Additionally, evidence is mounting for delayed radio emission in a wider sample of TDEs (Horesh et al. 2021; Somalwar et al. 2023), and the full extent of this phenomenon is yet to be observed. A recent review (De Colle & Lu 2020) posits that the fraction of TDEs that launch jets is largely unconstrained in the range of 3×10^{-3}–1.

3. Third, evolution in the SMBH mass function, and stellar populations available for disruption, must be accounted for in comparing local TDE rates with the higher-redshift CSO 2 sample. This latter effect may result in a near order-of-magnitude decline in the total TDE rate between $0 < z < 1$ (Kochanek 2016).

We nonetheless argue that the CSO 2 birth rate is consistent with expectations from the TDE rate. For SMBH masses $\lesssim 10^8 \; M_\odot$, consistent with most TDEs observed as transients, giant stars are likely to contribute 10% of the rate (Magorrian & Tremaine 1999; MacLeod et al. 2012). Approximately 3×10^{-4} of the SMBHs in the local Universe have masses in excess of $10^{9.4} \; M_\odot$ (Shankar et al. 2009), representing the typical SMBH masses of the CSO 2 sample. The remaining factor of 10^3 discrepancy can be explained by the need to disrupt the most massive evolved stars (or even more massive main-sequence stars) likely in the tips of the red giant or AGB sequences, possibly on deeply plunging orbits, and potentially in the presence of previous AGN activity and/or a rapidly spinning SMBH. Further, as indicated in Figure 11, an extrapolation of the birth rates of CSO 2s is consistent with the range of relativistic TDE birth rates inferred by De Colle & Lu (2020), assuming a maximum luminosity consistent with observed relativistic TDEs (Andreoni et al. 2022). This hints at a continuum of jet powers between the TDEs observed as

transients and CSO 2s, where the luminosity is determined by several factors including SMBH properties, and the physical properties and orbits of the disrupted stars.

12.3. Predictions of the CSO 2 TDE Scenario

Although it is plausible that CSO 2s can be explained by TDEs around the most massive SMBHs, testable predictions of this scenario are required in order to proceed. First, evidence for significant ongoing accretion, in particular $\gg 10^{-4}$ of the Eddington rate, should be absent from CSO 2s. Identifying a sample of slowly evolving nuclear transients that can be linked to evolved-star TDEs around lower-mass SMBHs can determine the corresponding rate, and enable tests of the outcomes of extended slow accretion, in particular with regards to jet launching.

We are only seeing the highest-luminosity CSO 2s in each redshift range. The lowest-luminosity CSO 2s in our complete samples have luminosities $\sim 3 \times 10^{25}\,\mathrm{W\,Hz^{-1}}$ but the lowest-luminosity CSO 2s we have observed have luminosities $\sim 10^{23}\,\mathrm{W\,Hz^{-1}}$.

As shown in Table 5 for object J1205+2031 (#43 in Figure 1), the radio energy requirement is four orders of magnitude lower than for a fiducial CSO 2 (J2355+4950). The energy requirement is only $\approx 10^{-4}\,M_\odot c^2$, well within the energy range of current TDEs. So it is clearly possible to observe CSO 2s that have both energy and luminosity comparable to those of TDEs caused by $\approx 1\,M_\odot$ stars.

We suggest, therefore, that these low-energy CSO 2s are indeed the results of TDEs of $\approx 1\,M_\odot$ stars, and that as we explore smaller CSO 2s at these low energies we will be able to form a connection with TDEs. A number of the bona fide CSO 2s have estimated ages in the 100–200 yr range. It is to be expected that as we push to higher resolution and lower flux densities, and continue to apply the CSO 2 selection, we will find CSO 2s in the 10–20 yr age range. This presents the prospect of studying the initial formation events in archival survey data.

We can push our limits on complete samples down a factor 10 by observing the steep spectrum CSOs in the sample that complements the incomplete flat spectrum VIPS sample, and we have undertaken a program to do just this.

13. Relativistic Jet Scenarios

If the expanded classification of CSO 2s into CSO 2.0s, 2.1s, and 2.2s represents a continuum of CSO evolution, as we contend, a coherent physical model should describe their sourcing and morphology. We now return to the topic of CSO 2 ignition and evolution discussed in Sections 5 and 12, and interpret it in the context of a uniquely fueled relativistic jet propagating into an external medium. We develop a model for CSOs in a separate paper (A. G. Sullivan et al. in preparation). For that reason, although much good work has been done on "young CSO" models, we do not refer to that work here, but discuss it fully in our upcoming paper. For the present we refer the interested reader to OS21 on this topic.

13.1. Fueling by Quasistationary Disks

13.1.1. Inflow Models

The traditional way to discuss the energetics of massive black holes in galactic nuclei is to suppose that the black holes

are essentially dormant until they are supplied with gas. If this happens through an orbiting disk at a steady rate $\dot{M}$ under the action of a local (usually magnetic) torque, then the radiative luminosity is $L = \epsilon \dot{M} c^2$, where ϵ is the radiative efficiency (Shakura & Sunyaev 1973; Balbus & Hawley 1991). For a thin disk, which is commonly believed to be appropriate when the mass supply rate is modest relative to the Eddington rate, ϵ is related to the binding energy of the innermost stable circular orbit (ISCO), which depends on the black hole spin, and leads to an estimate $\epsilon \sim 0.05$–0.4. For $r \gg r_{\mathrm{ISCO}}$, the outward transport of angular momentum and energy by the torque contributes to the dissipation at a rate three times the local release of gravitational binding energy. Energy is conserved because a zero torque boundary condition at the ISCO leads to a deficit in the release of energy by the disk, close to the ISCO. The energy released is presumed to be radiated and outflows are supposed to be dynamically unimportant. This is now called "standard and normal evolution" or SANE accretion (Curd et al. 2022).

When the mass supply rate is either much smaller or much larger than this, it is commonly argued that the accretion is radiatively inefficient close to the black hole and $\epsilon \ll 1$. For a low mass supply rate, it is supposed that a thick, ion pressure–supported torus forms. The ions are accompanied by much cooler electrons which have to maintain a near-Maxwellian distribution function at ~ 0.1 of the ion temperature, despite being collisionless and in the presence of plasma turbulence. When the mass supply rate is large, the gas becomes radiation dominated and the inefficiency follows from photon trapping. In either case, the torus's funnel supposedly traps magnetic flux in what is now called a magnetically arrested disk (MAD) state (Narayan et al. 2022 and references therein). If the black hole is spinning fast, a significant amount of flux threads the event horizon and two electromagnetically powered jets are formed. As the gas flow is essentially conservative, it was, traditionally, supposed to pass through a cusp, located in the equatorial plane between the marginally stable and marginally bound orbits, before plunging, invisibly, into the horizon.[16]

Under these circumstances, jet formation has been seen, implicitly, as a consequence of accretion with jet power efficiency $L_{\mathrm{jet}} = k \dot{M} c^2$, with k variously estimated to increase from ~ 0.3 to ~ 2—we adopt $k = 1$—as the angular frequency of the black hole, Ω_{H}, increases from $\sim 0.5\Omega_{\mathrm{max}}$ to $\Omega_{\mathrm{max}} \equiv c^3 / 2GM$ (Tchekhovskoy et al. 2011). A near-maximally rotating black hole will put roughly 10 times as much power into the jets as would have been released by the accreted gas in a steady, radiatively efficient disk flow and much more than is released in a radiatively inefficient flow. On the other hand, the jet production efficiency estimated for a small sample of CSOs does not seem to reach the highest efficiency levels (Wójtowicz et al. 2020).

This view has been developed with the aid of powerful, general relativistic magnetohydrodynamic (MHD) and particle-in-cell simulations (Tchekhovskoy et al. 2011; Parfrey et al. 2019; Davis & Tchekhovskoy 2020). They usually derive from initial conditions with mass and magnetic flux orbiting the black hole (Narayan et al. 2022). These simulations frequently exhibit winds, driven by radiation pressure, gas pressure, or

---

[16] More recent MAD simulations exhibit a strong toroidal current sheet (Parfrey et al. 2019; Ripperda et al. 2022). The continued avoidance of reconnection, particle acceleration, and efficient radiative emission in this current sheet is problematic.

magnetic fields, though most of the mass supplied passes through the torus to the black hole. After settling down to a quasi-steady state the disk can also exhibit local dynamo action, so that the polarity of the magnetic field threading the horizon alternates relatively rapidly (Simon et al. 2011). These field reversals are thought to occur on many radial scales with clear, observational implications for the jets.

13.1.2. Outflow Models

An alternative model of the gas flow is suggested by the Event Horizon Telescope observations of M87 (Event Horizon Telescope Collaboration et al. 2019). In its most extreme form, when the black hole is near-maximally rotating, most of the gas supplied to the outer disk is carried off by a hydromagnetic wind (Blandford & Globus 2022). The power for driving this wind comes primarily from the spin of the black hole, not the release of gravitational energy by infalling gas.[17]

In the outflow model, it is conjectured that the black hole is immersed in an ergomagnetosphere with very little gas present and that electromagnetic energy is transported radially outward from the hole, through a small-scale (a "clutch") or large-scale (a "capstan") electromagnetic field connecting the horizon to the disk, as well as parallel to the spin axis to form the jets (Blandford & Globus 2022). The magnetic flux passes through the equatorial plane, even close to the horizon, without forming a dissipative current sheet. It is "hemmed in," not by the pressure of hot gas orbiting in a thick torus, as in the inflow model, but by the inertia of cold gas orbiting in a thin disk and the vertical magnetic field threading the disk, strong enough to suppress the magnetorotational instability (Blandford & Globus 2022). Stresses applied to this vertical field below the Alfvén point are communicated to the disk. The transition from magnetic to inertial dominance happens at a radius $r_{\rm ring}$, and the mass of orbiting gas in this region is $m_{\rm ring}$. Presumably, $r_{\rm ring}$ and $m_{\rm ring}$ increase with $\Omega_{\rm H}$. Rotation power is unimportant below some intermediate value of $\Omega_{\rm H}$.

Within the ring, the strength of the poloidal magnetic field must be roughly constant. Outside the ring, the magnetic field strength declines with radius, in such a way as to maintain the magnetocentrifugal wind, although the total flux threading the disk resides mostly at large radius. This wind is then responsible for the jet collimation, extending far along the jet and interacting with its surface. Under these circumstances, the jet power should be bounded above by $\sim (\Omega_{\rm H}/2\pi\Omega_{\rm max})^2 (GM/r_{\rm ring}c^2)^{-4}(m_{\rm ring}/M)$ times the gravitational power $c^5/G \sim 3 \times 10^{52}$ W, with $\Omega_{\rm max} = c^3/2GM$. This allows the jet power to be much larger than ever observed, in principle.

However, it is unreasonable to expect the gas to remain in the ring forever. Either an interchange-like instability will allow it to accrete onto the black hole, as in the inflow model, or magnetic stress will expel it as the innermost part of a wind, as in the outflow model. If we suppose that the residence time of the gas in the ring is N times the dynamical time at the ring, $t_{\rm ring} = N(r_{\rm ring}^3/GM)^{1/2}$, then we can introduce the flow rate through the ring $\dot{m}_{\rm ring} = m_{\rm ring}/t_{\rm ring}$, to obtain

$L_{\rm jet} \sim N(\Omega_{\rm H}/2\pi\Omega_{\rm max})^2 (GM/r_{\rm ring}c^2)^{-5/2}\dot{m}_{\rm ring}c^2$, accommodating both models. What is important is that the total jet energy produced, under either idealization, can equal, and may even exceed, the rest-mass energy of the gas supplied to the ring, provided the black hole rotates rapidly.

13.2. Ignition Models

13.2.1. TDEs

We consider two possible explanations for the sources of CSO 2s to account for the most energetic (Table 5) and the most luminous (Figure 4(b)) CSO 2s. The first is that the CSO 2s are associated with black holes that spin at least modestly fast, $\Omega_{\rm H} \gtrsim 0.5\Omega_{\rm max}$ and capture a single star. We introduced this model in Section 12 (Rees 1988; OS21), and elaborate here on the plausibility of this model on physical grounds. The maximum CSO 2 energies measured so far, $\sim 7~M_\odot c^2$, can be accommodated by a single stellar capture under either the inflow or the outflow models. When $\Omega_{\rm H}$ is large, the Lense–Thirring precession of the orbits of the debris will lead to the presence of infalling gas from many directions which, under the outflow model, is conducive to the formation of a collimated jet. Less energetic CSOs are easily explained with lower $\Omega_{\rm H}$ or partial tidal stripping.

Models of TDEs generally suppose that stars are ripped apart on relativistic parabolic orbits and that the bound debris returns to the black hole and eventually settles into a disk at a rate $\dot{M}$. As previously discussed, the simplest dynamical models of this give $\dot{M} \propto (t/t_0)^{-5/3}$ (Phinney 1989), though simulations show a richer pattern of outcomes (Bonnerot & Lu 2020; Curd 2021). For the inflow model, we expect the amount of mass that falls in after time t will decrease $\propto t^{-2/3}$. Less than about $10^{-5}~M_*$ will be available to power a CSO 2.0 after ~ 1000 yr, which seems inadequate. However, for the outflow model, mass may be cycled, through a magnetocentrifugal wind (Blandford & Payne 1982), many times to large radii without becoming unbound so that it will fall back again. This can prolong the timescale over which a jet can be powered.

If TDEs operating under the outflow scenario are responsible for most CSO 2s, then it is reasonable to expect that CSO 2s should be accompanied by a disk luminosity corresponding to a net inflow $\dot{M} \sim 10^{-3}~M_\odot$ yr^{-1} or total disk luminosity $\lesssim 10^{43}$ erg s^{-1}. In addition, the central black holes should be rapidly spinning, as might be made apparent by X-ray spectroscopy of fluorescent iron lines.

More generally, many new observational capabilities are coming online and much should be learned about TDEs, reconciling radio, optical, and X-ray perspectives. This will provide a better framework in which to interpret our, no less rapidly, developing understanding of CSOs. This includes the possibility that we will be able to rule out the TDE model.

13.2.2. Disk Instabilities

An alternative model for CSOs[18] supposes that the disk is thin and accretes gas at a modest rate. The outer disk may evolve to a state of instability, possibly thermal (Czerny et al. 2009), similar to what is observed in dwarf novae (Smak 1984; Osaki 1996). Such an instability induces a sudden transition to a high-torque state when the mass inflow increases by several

---

[17] If the black hole rotational energy is not tapped, it is still energetically possible for most of the mass supplied at large radii to escape to freedom in a wind from intermediate radii (Blandford 1999). This can be powered, gravitationally, by a small fraction of the supplied mass, that makes it to the ISCO, and which, altruistically, sacrifices itself for this purpose. However, this arrangement is unlikely to form powerful jets and is not of interest for CSOs.

[18] As with supernovae and gamma-ray bursts, it would not be a surprise if the full class of CSOs involved quite different physical explanations.
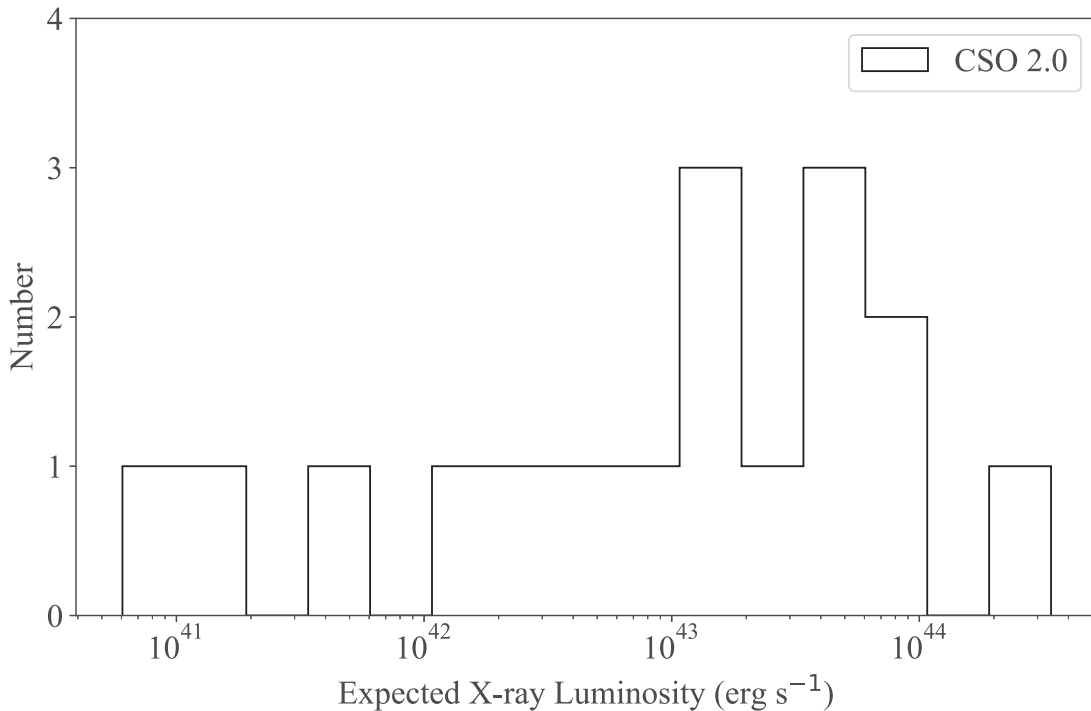
Figure 15. The expected thermal X-ray luminosities of the 17 bona fide CSO 2.0s with spectroscopic redshift if collimated by gas pressure.

orders of magnitude. For example, if the steady rate of inflow is $\dot{M} \sim 10^{-5}\, M_\odot\, \mathrm{yr}^{-1}$, and it increases by 100 at a radius $\sim 10^{17}$ cm, where there is $\sim 1\, M_\odot$ of gas, then it might be possible to account for the higher level of jet power needed to account for a CSO.[19] This model might be challenged to account for the apparent upper cutoff in the CSO 2 energies. Again, disk emission might be expected.

13.3. Propagation into External Media

13.3.1. Early Life Expansion

Once the jets of a CSO 2 have been launched, they propagate into the external medium in much the same manner as that of a typical FR II source. We suppose that in this stage—corresponding with the CSO 2.0 phase—the actively launched jet collides with the external medium and shocks form at its head. At these shocked regions, the hot spots, like those apparent in J1035+5628 in Figure 12, form due to particle heating of the jetted material in the shocked regions, which simultaneously amplifies magnetic fields and synchrotron emission (Begelman et al. 1984; Blandford et al. 2019). At the site of this hot spot, the jetted material becomes redirected upstream and inflates a cocoon bounding the jet. This cocoon will also emit synchrotron radiation and should produce the less bright radio emission surrounding the hot spots (Begelman et al. 1984).

Directing relativistic outflows out to distances $\gtrsim 10$ pc, as seen in CSO 2s and indeed larger double radio sources, requires a large-scale collimation mechanism. Explanations of this collimation involve pure gas pressure from either the cocoon or the ambient medium (e.g., Bromberg et al. 2011; Harrison et al. 2018), or large-scale magnetic fields (e.g., Lyubarsky 2009, 2011). In the former scenario, the ambient pressure

directly balances the component of the jet ram pressure projected perpendicular to the jet axis (McConville et al. 2011). A strong collimation shock forms at the site of the pressure balance, and redirects the jetted material along the jet axis. In magnetized jets, the hoop stress of the magnetic field assists in collimation. While these two models do not give significantly different phenomenological descriptions of jets (i.e., that the jet propagates into the external medium, inflating a cocoon to pressure confine the jet), the additional magnetic pressure can require lower external gas pressure for collimation (Bromberg et al. 2014). Distinguishing between these models should be achievable observationally.

Luminous thermal X-rays surrounding the jet represent one potential probe. Since in a gas-collimated jet the thermal pressure of the external medium must balance the pressure in the jet p_j, we expect:

$$\frac{1}{3}\frac{U_{\mathrm{tot,eq}}}{V} = n_a k_B T_a, \qquad (6)$$

where $U_{\mathrm{tot,eq}}$ is once again the equipartition energy of the CSOs, V is the volume of the emitting region, n_a is the number density of the ambient gas, k_B is Boltzmann's constant, and T_a is the external temperature. In Equation (6) for pressure balance, we have assumed that the CSO 2 jet pressure is one-third the average equipartition energy density. With an ambient gas temperature of $T = 10^7$ K, we estimate the external particle density and consequently the luminosity of its thermal emission (e.g., Rybicki & Lightman 1985). We show the anticipated thermal X-ray luminosities for CSO 2.0s in Figure 15. We expect gas pressure–collimated CSO 2.0s to have X-ray luminosities in excess of $\sim 10^{41}$ erg s^{-1}. X-ray emission in excess of this threshold (although with low spatial resolution) has already been observed among some CSO 2s (Britzen et al. 2007; Siemiginowska et al. 2016; Kosmaczewski et al. 2020),

---

[19] If this model were also to explain some TDEs, the leading edge of the inflow would have to steepen to form a front and not diffuse.

giving credence to the gas pressure–collimated hypothesis. However, inverse-Compton emission originating in jets (Stawarz et al. 2008; Sobolewska et al. 2022) and thermal X-rays from the accretion disk (Koratkar & Blaes 1999; Kubota & Done 2018; Sobolewska et al. 2022) may also account for an X-ray excess. Although difficult, the resolution of X-ray emission from nearby CSOs at subkiloparsec scales of the core could help distinguish these origins.

Simultaneously, constraints on magnetized jets may come from additional radio polarization measurements as well as improved radio spectra. The stronger and more orderly magnetic fields in this model should induce greater degrees of magnetic polarization. Another difference between the gas pressure–dominated and magnetized models lies in the advance speed of the jet head. The heads of Poynting flux–dominated jets are predicted to propagate at relativistic speeds, notably faster than their totally gas pressure–collimated counterparts, as the lack of collimation shocks near the base of the jets does not slow the jets down (Bromberg et al. 2014). The subrelativisitic advance speeds observed in CSO 2.0s makes this globally magnetized jet scenario unlikely. Further measurements of the speeds of advance of CSO 2s can constrain this model considerably. Nevertheless, these jets could still be strongly magnetized at small scales with instabilities dissipating larger-scale magnetic fields, giving way to a principally cocoon gas pressure–collimated jet at those scales (Levinson & Begelman 2013). In such cases, standing transverse magnetosonic oscillations in the jet on parsec scales (Lyubarsky 2009; Levinson & Globus 2017) or significant rotation measures (e.g., Kharb et al. 2009) may give credence to this model.

13.3.2. Late-life Rise

Motivated by the morphological structure previously described, we suppose that the transition that separates CSO 2.0s from CSO 2.2s occurs when jet fueling either severely weakens or terminates completely. While the intermediate stage between these two states remains obscure, due to the ambiguous nature of the CSO 2.1 class, we believe it possible that after a period of jet activity, the CSO 2 jet shuts off (possibly due to one of the models considered in Section 13.2), and the remaining downstream material in the cocoon begins to rise convectively as a turbulent plume. In this model, the rising plume phase represents the CSO 2.2 state.

Before discussing the consequences of the rising plume model, we first briefly consider our motivation for interpreting late-life CSO 2s as lacking active jets. Without active jets, they should emit less radio synchrotron emission as there is no longer a continuously supplied stream of energetic particles flowing from the core. Additionally, we also expect less X-ray emission than early life CSO 2s as the material in the radio-emitting lobes will be less energetic, and no longer require the strong collimation needed in the CSO 2.0 case. Objects we classify as CSO 2.0 represent nearly twice as many X-ray sources as those we classify as CSO 2.2s in recent observations (Kosmaczewski et al. 2020). With both lower radio luminosities and even fewer X-ray detections than CSO 2.0s, we suppose that the radio lobes of late-life CSO 2.2s may rise as plumes rather than through strong jet power.

A turbulent plume rises buoyantly as long as the density inside the plume remains less than the density of the ambient medium. This occurs subsonically as the plume both collides with the external medium at its head and entrains ambient material without forming a strong shock. If the ambient medium is convectively stable, i.e., the ambient density decreases with distance from the central engine, the plume will reach a terminal distance, at which point it begins to spread horizontally (Morton et al. 1956) and produces the characteristic mushroom cloud shape observed in volcanic plumes (Woods 2010). In fact, Morton et al. (1956) showed that a plume rising in any convectively stable ambient medium will reach a maximum distance from the central engine and begin to spread horizontally.

This picture can explain the observed behavior of CSO 2.2s, whose outward-advancing speeds are negligible and which exhibit sizable features orthogonal to the jet direction. Consider an ambient density profile of $\rho_a = \rho_0(\zeta_0/\zeta)^a$, where ζ is the distance from the center of the AGN. We may estimate the change in distance of the buoyant plume $\Delta\zeta$ from the central engine by the scale height of the ambient medium:

$$\Delta\zeta \sim \left[\rho_a \left| \frac{d\rho_a}{d\zeta} \right|^{-1} \right]_{\zeta_0} = \frac{\zeta_0}{a}, \tag{7}$$

where ζ_0 is the distance at which the plume begins to rise. ζ_0 may represent the distance from the central engine reached by the active CSO 2.0, so the maximum distance achieved by the buoyant inactive CSO 2.2 will be $\zeta_{max} = \zeta_0 + \Delta\zeta$. Therefore, the maximum size of a CSO 2 should be:

$$D_{max} = \left(1 + \frac{1}{a} \right) D_0, \tag{8}$$

where $D_{max} = 2\zeta_{max}$ and $D_0 = 2\zeta_0$ (since the total CSO 2 size contains both lobes). Setting D_0 as the median CSO 2.0 size of 129 pc and using a fiducial value for a of 2 (Wang et al. 2022), we obtain an expected size of CSO 2.2s of 200 pc, about a 40% difference from the observed median size of 340 pc. A less steep profile of $a = 0.75$ gives an expected size of CSO 2.2s of 300 pc, nearly an exact match to the observed median size. (On much longer timescales, it is possible that these plumes might evolve to very faint bubbles, analogous to those seen in rich clusters of galaxies.) Consequently, this simple pictures comports with observed CSO 2 properties.

14. Future Observations

If the size statistics discussed in Paper II hold once the steep spectrum counterpart of the VIPS sample has been observed, then a highly significant new avenue for the study of jetted AGN has been discovered. The follow-up of these results with VLBI observations of larger, deeper samples of CSO 2s, including at higher frequencies so as to include smaller CSO 2s, can address, in both the time domain and the structure dimensions, questions on the fueling, launching, and propagation of relativistic jets, in ways that were previously inaccessible.

From the statistics of CSOs in the VIPS and PR+CJ1+PW samples (Paper I) we estimate that over the whole sky there are $\sim$300–1000 CSOs with $S_{8.5\,\text{GHz}} \gtrsim 85$ mJy^{-1} that will be amenable to study with current and planned instruments, greatly improving the power of statistical tests. It will also be possible to look for even fainter CSOs in selected regions to probe the population of low-luminosity CSOs.

Current surveys include VLASS (Lacy et al. 2020) which covers decl. $> -40°$ at 2–4 GHz with a resolution of $2''5$, and detects sources brighter than 1 mJy. With its three epochs of observation, it will provide a list of compact, low-variability sources that can be followed up with VLBI. In addition the MEERKAT (Jonas & MeerKAT Team 2016) and ASKAP (Johnston et al. 2008) instruments provide powerful CSO search capabilities in the Southern Hemisphere.

Future instruments will also find more CSOs. The proposed DSA2000 (Hallinan et al. 2019), covering frequencies 0.7–2.0 GHz and 4 month cadence over 16 epochs will provide an ideal complement to VLASS. The sensitivity of 2 μJy beam^{-1} at each epoch would enable sensitive monitoring of variability of CSOs down to 1 mJy in total flux density, or deeper if necessary.

To improve our understanding of the astrophysics of CSOs, deeper and higher-resolution observations will be needed. We can increase the resolution and sensitivity by going to higher frequencies (45 and 90 GHz), using global VLBI arrays that incorporate large antennas, such as the Green Bank Telescope, the Effelsberg Telescope, Deep Space Network antennas, and the Large Millimeter Telescope. In the longer term, the proposed Next Generation VLA (ngVLA) will be much more sensitive than the VLBA, and its large bandwidth will allow, for example, all of the 3.5–12.3 GHz band to be covered simultaneously. The rms noise in a 1 hr observation is expected to be about 3.2 μJy beam^{-1} at 8 GHz, and an order of magnitude lower at higher frequencies, for a 1 mas beamwidth.[20]

To exploit the full potential the class of CSO 2s offers for understanding the origins and astrophysics of jetted AGN, we will need several orders of magnitude improvement in dynamic range, and a factor ∼four improvement in resolution. This will require extending the VLBI arrays (such as the ngVLA) to near-Earth orbit (NEO). A single 10 m antenna in NEO, operating up to 90 GHz, would allow observations of 300 sources in 18 months down to a flux density limit of <85 mJy at 8.5 GHz. With a 6 yr mission lifetime, i.e., four 18 month cycles, separation speeds down to $0.03c$ could be measured with the (u, v) coverage shown in Appendix D.

15. Conclusion

We have examined a carefully selected sample of 54 bona fide CSOs for which we have spectroscopic redshifts. We have defined three new morphological classes of CSOs: CSO 2.0, CSO 2.1, and CSO 2.2. We have classified the 54 CSOs in our sample into these three CSO 2 classes and the CSO 1 class, using blind tests.

We find it remarkable that, in spite of the very wide variety of morphologies displayed by CSOs, it is possible to classify them into just four morphological classes. We also find the agreement in our blind tests noteworthy.

The resulting classifications of CSO 2s, and their different positions in the (P, D) plane can be explained on the simple hypothesis that there is an evolutionary sequence CSO 2.0→CSO 2.1→CSO 2.2, with CSO 2.0s being "early life," CSO 2.1s "midlife," and CSO 2.2s "late-life" CSOs.

Such an evolutionary sequence provides an explanation for the size cutoff of CSO 2s that was found in Paper II, and is consistent with all that is known about the phenomenology of

CSO 2s. The theory could be tested by carrying out a systematic study of the speeds of advance of CSO 2.2s compared to those of CSO 2.0s and also by looking for systematic differences in ages between these two classes.

The origins of CSO 2s and the reasons for their relatively short lives as jetted AGN will be the subjects of continuing studies. At this stage, none of the possibilities we have considered for ignition, including TDEs and MHD instabilities in the accretion disk, and the extraction of the spin energy of the SMBH can be definitively ruled out. It is entirely possible that multiple mechanisms play a role in CSOs since it is clear that CSOs constitute not so much a "class" but more of a "family" of AGN that is, as yet, relatively unexplored, and has the potential for studying AGN and relativistic jets that will lead well beyond what we can imagine at this stage.

All of these considerations make it clear that CSOs provide a unique and vastly underexploited window into the study of SMBHs, their accretion disks, and the birth of relativistic jets. This amounts to a new, and compelling, science driver for both the DSA2000 and ngVLA. The multiepoch DSA2000 surveys will have the sensitivity to dig down to very low luminosity to provide samples of weak CSOs. The ngVLA, operating up to 90 GHz in conjunction with the existing global VLBI network, where needed, will provide studies of CSOs that could revolutionize the study of AGN and, by extension, other sources known to form relativistic jets such as X-ray binaries, gamma-ray bursts, and pulsars. These include the creation, launching, and fueling of relativistic jets, and, most importantly, whether the existing paradigm for the fueling of relativistic jets, via accretion, is always correct, or whether their energy can derive from the spin of the black hole.

---

[20] https://ngvla.nrao.edu/page/performance

jetted AGN, this paper is dedicated to Mark Birkinshaw. Mark was working hard on this paper right up until his death from cancer on 2023 July 23. Mark is sorely missed worldwide by his colleagues and friends.

Appendix A
Table of Bona Fide CSOs in R.A. Order

Table 8 has the same information as that in Table 1, but with the sources arranged in order of R.A.

Table 8
Key to the CSOs in Figure 1 in R.A. Order

Source Name	ID #	z	Class	Source Name	ID #	z	Class
J0029+3456	8	0.517	CSO 2.0	J1311+1658	38	0.081408	CSO 1
J0111+3906	3	0.668	CSO 2.0	J1313+5458	20	0.613	CSO 2.2
J0119+3210	35	0.0602	CSO 2.2	J1326+3154	13	0.37	CSO 2.2
J0131+5545	41	0.03649	CSO 2.2	J1347+1217	28	0.121	CSO 2.2
J0405+3803	53	0.05505	CSO 2.0	J1400+6210	15	0.431	CSO 2.2
J0713+4349	11	0.518	CSO 2.0	J1407+2827	52	0.077	CSO 2.1
J0741+2706	9	0.772137	CSO 2.1	J1414+4554	36	0.186	CSO 2.1
J0825+3919	18	1.21	CSO 2.1	J1434+4236	22	0.452	CSO 2.2
J0832+1832	54	0.154	CSO 1	J1440+6108	30	0.445365	CSO 2.1
J0855+5751	39	0.025998	CSO 2.1	J1508+3423	33	0.045565	CSO 2.1
J0906+4124	46	0.027	CSO 1	J1511+0518	51	0.084	CSO 2.0
J0909+1928	44	0.027843	CSO 1	J1559+5924	47	0.0602	CSO 1
J0943+1702	10	1.601115	CSO 2.0	J1602+5243	26	0.105689	CSO 1
J1025+1022	40	0.045805	CSO 1	J1609+2641	14	0.473	CSO 2.1
J1035+5628	12	0.46	CSO 2.0	J1644+2536	23	0.588	CSO 2.1
J1111+1955	1	0.299	CSO 2.0	J1723−6500	49	0.01443	CSO 2.1
J1120+1420	21	0.362	CSO 2.0	J1734+0926	6	0.735	CSO 2.0
J1148+5924	42	0.01075	CSO 1	J1735+5049	4	0.835	CSO 2.0
J1158+2450	32	0.203	CSO 2.2	J1816+3457	31	0.245	CSO 2.1
J1159+5820	17	1.27997	CSO 2.0	J1915+6548	25	0.486	CSO 2.1
J1205+2031	43	0.024037	CSO 2.1	J1939−6342	7	0.1813	CSO 2.0
J1220+2916	45	0.002	CSO 1	J1944+5448	29	0.263	CSO 2.0
J1227+3635	16	1.975	CSO 2.0	J1945+7055	37	0.101	CSO 2.2
J1234+4753	34	0.373082	CSO 2.1	J2022+6136	2	0.227	CSO 2.1
J1244+4048	19	0.813586	CSO 2.2	J2203+1007	5	1.005	CSO 2.0
J1247+6723	50	0.107219	CSO 2.0	J2327+0846	27	0.02892	CSO 1
J1254+1856	48	0.1145	CSO 1	J2355+4950	24	0.238	CSO 2.2

Notes. The ID # is the reference number in Figure 1. References for the redshifts are given in Paper I.

Appendix B
Individual Classification Notes for the 54 Bona Fide CSOs that Have Spectroscopic Redshifts

Numbers in [square] brackets are those assigned to the objects in Figure 1, Tables 1, and 8. A dagger[†] indicates the reference to the map displayed in Figure 1.

J0029+3456, CSO 2.0 [8]: maps at 5 GHz (Fomalont et al. 2000)[†] and 15 GHz (MOJAVE stacked epoch) show clear hot spots at the opposite outer edges of the lobes.

J0111+3906, CSO 2.0 [3]: Taylor et al. (1996),[†] using multifrequency, multiepoch observations, pinpointed the flat spectrum center of activity—marked by the red cross in Figure 1—and provided compelling evidence of steep spectrum hot spots situated at the outer edges of the lobes straddling the nucleus. This was the first CSO to be shown to have some faint large-scale structure, and thus to have had previous activity, which established the existence of multiple epochs of activity in some CSOs (Baum et al. 1990).

J0119+3210, CSO 2.2 [35]: the 5 GHz map by Giroletti et al. (2003)[†] shows weak hot spots in highly resolved lobes perpendicular to the source axis.

J0131+5545, CSO 2.2 [41]: the stacked epoch MOJAVE[†] image shows two highly resolved, edge-brightened lobes with no hot spots, (Lister et al. 2020), making this is a CSO 2.2 object. Lister et al. (2020) interpret this and the emission gap between the lobes and bright inner jet as evidence of two separate epochs of activity in this object, which may be correct, but since compact components are seen along the jets of many CSO 2s, and since we interpret the structure as showing two such compact components (see Section 6.2, and Figure 8(e)), we assume here that this is a normal CSO and not an object displaying two separate epochs of acitvity.

J0405+3803, CSO 2.0 [53]: the multifrequency observations of Maness et al. (2004)[†] show clearly that there are hot spots at the outer extremities of the inner lobe structure. In addition, as these authors show, there are two active nuclei in this object, so this is also a rare example of a binary SMBH. This CSO exhibits more than one epoch of activity (Maness et al. 2004).

J0713+4349, CSO 2.0 [11]: Readhead et al. (1984) showed that this object has a flat spectrum core, a steep spectrum jet, and two steep spectrum lobes. Taylor et al. (1996) pinpointed the center of activity and showed that there are hot spots at the extremities of the lobes. The image shown is a MOJAVE[†] stacked image.

J0741+2706, CSO 2.1 [9]: Tremblay et al. (2016)[†] observed this object at 5 GHz and 8 GHz, and identified the flat spectrum core and two steep spectrum lobes. The object is edge dimmed—i.e., the regions of highest surface brightness outside of the core are closer to the core than to the outer edges of the lobes. There are no clear hot spots. The blind tests were split equally between CSO 2.1 and 2.2. This shows that the classification is intermediate, and hence this is a CSO 2.1 object.

J0825+3919, CSO 2.1 [18]: in view of the absence of dominant hot spots at the outer edges of the lobes (Orienti et al. 2004),[†] we classify this as a CSO 2.1.

J0832+1832, CSO 1.0 [54]: like J0741+2706, Tremblay et al. (2016)[†] observed this object at 5 GHz and 8 GHz, and identified the flat spectrum core and two steep spectrum lobes. The object is edge dimmed—i.e., the regions of highest surface brightness outside of the core are closer to the core than to the outer edges of the lobes. There are no clear hot spots. The edge-dimmed morphology makes this a CSO 1 object.

J0855+5751, CSO 2.1 [39]: Taylor et al. (2005), in pilot VIPS 5 GHz observations, identified this object as a CSO based on the morphology of the two lobes and the hot spots in the lobes. Biggs et al. (2016)[†] rereduced the data and their map makes clear that the northern hot spot is at the outer extremity of the lobe, whereas the southern hot spot is not at the outer extremity of the lobe. This discrepancy in the morphologies of the two lobes leads to the classification as "intermediate," or CSO 2.1.

J0906+4124, CSO 1 [46]: the European VLBI Network (EVN) images at 5 GHz and 8 GHz by Cheng et al. (2021)[†] show a flat spectrum core flanked by two oppositely directed edge-dimmed jets in this low-luminosity CSO 1 object.

J0909+1928, CSO 1 [44]: the VLBA image at 8.4 GHz by Cheng & An (2018)[†] shows a strong core flanked by two oppositely directed edge-dimmed jets in this low-luminosity CSO 1 object.

J0943+1702, CSO 2.0 [10]: Tremblay et al. (2016) identified this as a CSO based on 5 and 8 GHz observations, which showed a clear flat spectrum core and two steep spectrum lobes. The lobes are barely resolved in the Tremblay et al. (2016) maps, but the MOJAVE[†] 15 GHz observations show clear hot spots at the outer edges of the lobes, making this a clear CSO 2.0 object. This is one of only three CSOs whose classification was revised after the blind tests[‡]. The CSO 2.0 classification was agreed unanimously in a group discussion of how the MOJAVE image was embedded in the 5 GHz image and the positions of the 15 GHz hot spots at the outer edges of the 5 GHz lobes.

J1025+1022, CSO 1 [40]: the VLBA image at 8.4 GHz by Cheng & An (2018)[†] shows a strong core flanked by two oppositely directed edge-dimmed jets in this low-luminosity CSO 1 object.

J1035+5628, CSO 2.0 [12]: Taylor et al. (1996) made 8.4 and 15 GHz observations of this PR (Pearson & Readhead 1988) CSO and identified its flat spectrum core and two leading-edge-brightened lobes, which are seen clearly in the MOJAVE[†] 15 GHz image.

J1111+1955, CSO 2.0 [1]: the 8.4 GHz image of Peck & Taylor (2000)[†] shows clear hot spots at the outer edges of the two lobes. Gugliucci et al. (2005) confirmed this as a CSO based on the steep spectra of the edge-brightened outer lobes.

J1120+1420, CSO 2.0 [21]: Bondi et al. (1998)[†] identified this as a CSO based on 23 GHz MERLIN and 1.6 GHz VLBA observations. In the Radio Fundamental Catalog[21] maps, this object has clear hot spots at the outer edges of the lobes, making this a CSO 2.0 object.

J1148+5924, CSO 1 [42]: the Tremblay et al. (2016) 5 and 8 GHz maps show this to be an edge-dimmed object, as is also seen in this image, which was processed by MOJAVE[†]. The morphology and low luminosity indicate this is a CSO 1 object. This object shows evidence of a previous epoch of activity.

J1158+2450, CSO 2.2 [32]: a very unusual object, as revealed in the 5, 8, and 15 GHz maps of Tremblay et al. (2008)[†]. The 5 GHz map shows an apparent east–west double source, but the 15 GHz map shows that the eastern component has a north–south CSO embedded in the slightly larger east–west structure. The 8–15 GHz spectral index map of Tremblay et al. (2008) clearly identifies the flat spectrum core and steep spectrum lobes in the north–south structure in the eastern

---

[21] http://astrogeo.org/rfc/

27

component, making this a clear CSO 2.2. This is one of only two CSOs whose classification was revised after the blind tests had been carried out‡. The final CSO 2.2 classification was unanimously agreed in a group discussion of the Tremblay et al. (2008) 8 and 15 GHz maps.

J1159+5820, CSO 2.0 [17]: the extended steep spectrum, edge brightened by hot spot outer lobes revealed in the 5 and 8 GHz images of Tremblay et al. (2016)† mark this objects as a CSO 2.0.

J1205+2031, CSO 2.1 [43]: the EVN images at 5 and 8 GHz by Cheng et al. (2021)† show two resolved lobes in this low-luminosity CSO 2.1 object.

J1220+2916, CSO 1 [45]: this object is observed in the 5 and 8 GHz observations of Tremblay et al. (2016)† to have a flat spectrum core, indicated by the red cross, and two edge-dimmed jets extending in opposite directions from the core. The morphology and low luminosity mark this as a CSO 1 object.

J1227+3635, CSO 2.0 [16]: this object is observed in the 1.7 and 5 GHz observations of Dallacasa et al. (2013), as well as the 5 and 8 GHz observations of Tremblay et al. (2016)† to have a flat spectrum core straddled by two steep spectrum lobes, one of which is at the end of a long, narrow jet and is strongly edge brightened. The optical identification is a quasar at redshift 1.973, which suggests that the jet axis cannot be close to the plane of the sky. The most likely interpretation is that this is a CSO where some effects of relativistic beaming are being seen, which might also explain the fact that this is the highest-luminosity CSO in this sample of 54. The side opposite the jet on this interpretation is deboosted and the hot spot radiation on that side is likely also deboosted. The morphology of the very narrow jet and strong hot spot on one side mark this as a CSO 2.0 object.

J1234+4753, CSO 2.1 [34]: this is an interesting case. Tremblay et al. (2016)† show that this object has an apparent flat ($\alpha \sim -0.5$ from 5 to 8 GHz) to steep ($\alpha \sim -1.0$ from 8 to 15 GHz) spectrum core, however, this could be a bright jet component, in which case the object is edge-brightened. The well-separated southern component makes clear the edge-brightened structure. We adopt this interpretation. As can be seen in Table 9 (Appendix C), all four teams classified this object as a CSO 2.1 in the blind tests.

J1244+4048, CSO 2.2 [19]: the Orienti et al. (2004)† map shows a nucleus and two-sided edge-dimmed jets. The 5 GHz and 8 GHz images of Tremblay et al. (2016) show a flat spectrum core and two-sided steep spectrum jet with highly resolved hot spots, indicative of a CSO 2.2.

J1247+6723, CSO 2.0 [50]: the 15 GHz map of Marecki et al. (2003)† shows hot spots toward the outer edges of the lobes, making this a CSO 2.0 object. This object is a clear double on larger scales, showing evidence of a previous epoch of activity.

J1254+1856, CSO 1 [48]: the 5 and 8 GHz maps of Tremblay et al. (2016) show a flat spectrum core with two fading, edge-dimmed steep spectrum jets. The morphology and low luminosity clearly indicate a CSO 1. The MOJAVE† image shows the same features.

J1311+1658, CSO 1 [38]: the 5 and 8 GHz observations of Tremblay et al. (2016)† show this object to have a flat spectrum core and two edge-dimmed steep spectrum jets. It is therefore a CSO 1 object.

J1313+5458, CSO 2.2 [20]: the 5 GHz map of Taylor et al. (1994)† shows two heavily resolved lobes. The 5 and 8 GHz observations of Tremblay et al. (2016) show these lobes to have steep spectra. The highest surface brightness region, possibly a hot spot, in one lobe is not at the extremity of the source, and the other lobe has an amorphous structure with no hot spot.

J1326+3154, CSO 2.2 [13]: the 5 GHz map of Helmboldt et al. (2007)† shows two highly resolved lobes with hot spots at extremities of the lobes in some directions, but not the overall extremities of the source, making this a CSO 2.2 object.

J1347+1217, CSO 2.2 [28]: the 5 GHz map of Stanghellini et al. (1997)† hows a well-resolved lobe on one side, and a weak lobe on the other side of the presumed nucleus. This object shows evidence of a previous epoch of activity.

J1400+6210, CSO 2.2 [15]: Taylor et al. (1996)† pinpointed the center of activity in this object, which made clear that it is a CSO. They also pointed out that, while there is a lot of structure in the jets, there are no visible hot spots. So this is a CSO 2.2 object.

J1407+2827, CSO 2.1 [52]: the strange morphology of this source, as shown in the MOJAVE† image, makes this object difficult to classify—hence it is "indeterminate," i.e., CSO 2.1.

J1414+4554, CSO 2.1 [36]: the 5 GHz map of Gugliucci et al. (2005)† shows an edge-brightened southern lobe with a resolved hot spot, and an edge-dimmed northern lobe, making this an "indeterminate" CSO 2.1 object.

J1434+4236, CSO 2.2 [22]: the 5 and 8 GHz observations of Tremblay et al. (2016)† show this object to have two resolved lobes, each with well-resolved extensions perpendicular to the source axis. Hence this is a CSO 2.2 object,

J1440+6108, CSO 2.1 [30]: the 5 and 8 GHz observations of Tremblay et al. (2016)† show this object to have two resolved lobes, each with well-resolved extensions perpendicular to the source axis, but with hot spots at the leading edges. Hence this is a CSO 2.1 object.

J1508+3423, CSO 2.1 [33]: the 5 GHz MERLIN observations by Kunert-Bajraszewska et al. (2010)† show a complex structure indicative of a CSO 2.1 object.

J1511+0518, CSO 2.0 [51]: the 22 GHz image of Orienti et al. (2006)† shows slight edge dimming in both lobes in this a very compact source. We have provisionally classified it as a CSO 2.0 because of its very compact, unresolved structure at all frequencies, from 2.3 to 22 GHz, including in the MOJAVE stacked image, perpendicular to the axis, but further observations at higher frequencies are needed to confirm this.

J1559+5924, CSO 1 [47]: the MOJAVE† and the 5 and 8 GHz observations of Tremblay et al. (2016) show this to be an edge-dimmed, low-luminosity CSO 1 object.

J1602+5243, CSO 1 [26]: the image of de Vries et al. (2009)† shows two edge-dimmed jets and this is clearly a CSO 1 object.

J1609+2641, CSO 2.1 [14]: the 5 and 8 GHz observations of Tremblay et al. (2016)† show this object to have a hot spot at the end of one lobe and the other lobe to be well resolved with no hot spot, making this an "intermediate"" CSO 2.1 object.

J1644+2536, CSO 2.1 [23]: the 5 and 8 GHz observations of Tremblay et al. (2016)† show this object to have a flat spectrum core flanked by two edge-dimmed jets, making this a CSO 2.1 object.

J1723−6500, CSO 2.1 [49]: the 8.4 GHz image of Angioni et al. (2019)† of this low-luminosity object shows a very curious, edge-dimmed structure, making this a CSO 2.1 object.

J1734+0926, CSO 2.0 [6]: as shown in the MOJAVE[†] map, this is a double-lobed object with hot spots at the outer edges of the lobes, and hence this is a CSO 2.0 object.

J1735+5049, CSO 2.0 [4]: Orienti & Dallacasa (2014)[†] carried out six -frequency VLBA observations of this object, which revealed its flat spectrum core, and steep spectrum lobes with hot spots at the outer edges being self-absorbed below 6 GHz. So this is clearly a CSO 2.0 object.

J1816+3457, CSO 2.1 [31]: the Gugliucci et al. (2005)[†] 8.4 GHz map shows resolved lobes, edge dimming in the southern lobe, and no hot spot in the northern lobe. Hence the CSO 2.1 classification. Note that the image has been rotated to fit into the available space in Figure 1, so that the southern lobe is the lobe at the upper left.

J1915+6548, CSO 2.1 [25]: as described by Gugliucci et al. (2007),[†] this is a very curious object, and is therefore of indeterminate class: CSO 2.1.

J1939–6342, CSO 2.0 [7]: as shown in the 8.4 GHz image of Tzioumis et al. (2002),[†] one of the lobes is unresolved at the outer edge, and the other is unresolved near the outer edge. Both lobes are unresolved perpendicular to the jet axis, making this a CSO 2.0 object.

J1944+5448, CSO 2.0 [29]: the 8.4 GHz map of Rastello et al. (2016) and the MOJAVE[†] image both show the core and two outer lobes with hot spots at the outer edges, which make this a CSO 2.0 object.

J1945+7055, CSO 2.2 [37]: in the 8 GHz map of this much-studied CSO (Peck et al. 1999), we see the core and two linear curving jets, the southern one culminating in a resolved component and the northern one having a hot spot coincident with a sharp bend in the jet transitioning to a fainter component further out. Since this object shows edge dimming at the ends of the two oppositely directed jets, as can be seen in the MOJAVE[†] image, we classify it as a CSO 2.2 object.

J2022+6136, CSO 2.1 [2]: in this object one lobe is edge brightened and the other is edge dimmed—hence the CSO 2.1 classification. The image is from Lister & Smith (2000).[†]

J2203+1007, CSO 2.0 [5]: the 15 GHz image of Orienti & Dallacasa (2014)[†] shows clear hot spots at the outer edges of the two lobes, making this a CSO 2.0 object.

J2327+0846, CSO 1 [27]: this highly unusual CSO was mapped at 1.4 GHz by Momjian et al. (2003),[†] who showed that its age as a jetted AGNR FR IIs this occurs a is a few megayears. Note that the center of activity has been identified by Momjian et al. (2003) with the highest surface brightness component, This source shows strong edge dimming and is therefore a CSO 1 object.

J2355+4950, CSO 2.2 [24]: this object has been extensively studied as the archetypical CSO by R96, who showed that it has two extended lobes—a southern one with a hot spot at the outer edge of he lobe, and a northern one having no hot spot. Although the southern lobe has a hot spot, material is spilling out of this hot spot toward the east. In addition, at lower frequencies the structure extends outside of the jets and hot spots to form a common envelope. The position of the flat spectrum nucleus was pinpointed by Taylor et al. (1996). R96 showed that there is a bright jet component in the northern jet, and they also showed that the northern jet is an order of magnitude brighter than the southern jet. This strongly suggests that the northern side is the approaching side and that we are seeing slightly beamed radiation from the two jets. On this interpretation, the northern lobe is seen at a considerably later epoch than the southern lobe, which could explain the lack of a hot spot in the northern lobe if the jet is no longer powering the hot spot in the northern lobe. There is, therefore, a strong hint of evolution in the jets and lobes. These considerations plus that extended envelope and significant extension of the source normal to the jet axis led us unanimously to classify this as a CSO 2.2 object in our blind tests (see Table 9). The image shown is from Owsianik et al. (1999).[†]

Appendix C
The Blind Tests

To conduct the blind tests, we formed four independent teams each consisting of two of the coauthors of this paper. These tests were "blind" in the following two senses. First, the four teams worked completely independently, with no knowledge of the classifications of the other three teams. Second, the classifications were based on morphology alone, with no cognizance of redshift, physical size, and luminosity, thereby precluding any influence of location in the (P, D) plane. We reclassified three objects because not all of the relevant maps had been taken into account in the initial classifications (J0943+1702, J1158+2450, and J2327+0846) after we had finished the blind tests, but these reclassifications were done after completing the blind tests and carrying out the statistical tests on the blind tests, and so do not affect the statistical results of the binomial tests presented in Table 2.

The two members of each team individually classified the 54 CSOs, then compared their results and agreed on a team classification. The results of the four teams' classifications are shown in Table 9. The results show remarkable consistency, given the variety of morphologies observed, and the small number of classes. In 47% of the cases all four teams agreed on the classification, in 85% of the cases three or four teams agreed, in 5% of the cases the classifications were split 2:2, and in 9% they were split 2:1:1. The final classifications are also given in Table 9.

The probabilities shown in Table 2 are derived as follows. There are four possible ways all four teams can choose the same classification ($p = 4/256 = 0.0156$), and 4! possible ways ($p = 24/256 = 0.0938$) all four teams could choose different classifications. In the case of exactly three teams agreeing, the number of possibilities is (four ways to pick the agreeing classification) × (three ways to pick a disagreeing classification) × (four ways to arrange these) = 48 ($p = 48/256 = 0.1875$). That leaves 180 ways that exactly two teams (or two pairs of teams) could choose the same classification ($p = 180/256 = 0.7031$).

The probabilities, under the random assumption, of agreement by all four teams, three or four teams, two teams, and by no teams, are given in the third column of Table 2. The differences between the actual numbers (fifth column) and the expected number (fourth column) are striking.

In the cases of the three objects marked with a double dagger (‡), which includes one of the 2:2 splits, the objects were discussed and the final decision on the correct classification was unanimous.

Table 9
Results of the Blind Classifications of CSOs in Figure 1

CSO Name	Team #1	Team #2	Team #3	Team #4	Final Class	CSO Name	Team #1	Team #2	Team #3	Team #4	Final Class
J0029+3456	2.0	2.0	2.0	2.0	2.0	J1311+1658	1	1	1	1	1
J0111+3906	2.0	2.0	2.0	2.0	2.0	J1313+5458	2.2	2.2	2.0	2.2	2.2
J0119+3210	2.1	2.2	1.0	2.2	2.2	J1326+3154	2.2	2.2	2.0	2.2	2.2
J0131+5545	2.2	2.2	1	2.2	2.2	J1347+1217	2.2	2.2	2.2	1	2.2
J0405+3803	2.0	2.0	2.1	2.2	2.0	J1400+6210	2.2	2.2	2.1	1	2.2
J0713+4349	2.0	2.2	2.0	2.0	2.0	J1407+2827	2.1	2.1	2.1	2.1	2.1
J0741+2706	2.2	2.1	2.1	2.2	2.1	J1414+4554	2.1	2.1	2.0	2.1	2.1
J0825+3919	2.2	2.1	2.2	2.1	2.1	J1434+4236	2.2	2.2	2.2	2.2	2.2
J0832+1832	1	1	2.1	1.0	1	J1440+6108	2.1	2.1	2.0	2.1	2.1
J0855+5751	2.1	2.1	2.1	2.1	2.1	J1508+3423	2.1	2.1	1.0	2.1	2.1
J0906+4124	1	1	1	2.0	1	J1511+0518	2.0	2.0	2.0	2.2	2.0
J0909+1928	1	1	1	1	1	J1559+5924	1	1	2.1	1	1
J0943+1702‡	2.0	2.1	2.1	2.1	2.0	J1602+5243	1	1	1	1	1
J1025+1022	1	1	1	2.2	1	J1609+2641	2.1	2.0	2.2	2.1	2.1
J1035+5628	2.0	2.0	2.0	2.0	2.0	J1644+2536	2.1	2.1	2.1	1	2.1
J1111+1955	2.0	2.0	2.0	2.0	2.0	J1723−6500	2.1	2.1	2.0	2.2	2.1
J1120+1420	2.0	2.0	2.0	2.0	2.0	J1734+0926	2.0	2.0	2.0	2.0	2.0
J1148+5924	1	1	1	1	1	J1735+5049	2.0	2.0	2.0	2.0	2.0
J1158+2450‡	2.2	2.2	2.1	2.1	2.2	J1816+3457	2.1	2.1	2.2	2.1	2.1
J1159+5820	2.0	2.0	2.0	2.0	2.0	J1915+6548	2.1	2.1	2.1	2.1	2.1
J1205+2031	2.1	2.1	2.0	2.1	2.1	J1939−6342	2.0	2.0	2.0	2.1	2.0
J1220+2916	1	1	1	1	1	J1944+5448	2.0	2.0	2.0	2.1	2.0
J1227+3635	2.0	2.0	2.0	2.0	2.0	J1945+7055	2.2	2.2	2.0	2.2	2.2
J1234+4753	2.1	2.1	2.1	2.1	2.1	J2022+6136	2.1	2.1	2.1	2.1	2.1
J1244+4048	2.2	2.2	2.2	2.2	2.2	J2203+1007	2.0	2.0	2.0	2.0	2.0
J1247+6723	2.0	2.0	2.0	2.0	2.0	J2327+0846‡	2.2	2.2	1.0	2.2	1
J1254+1856	1	1	1	1	1	J2355+4950	2.2	2.2	2.2	2.2	2.2

Notes. Four teams of two carried out the classification independently. At first each member of a team made their own independent classification, and then they conferred to agree on a final classification. The results are listed for each team. The final classification was chosen based on the majority vote. There were only three cases in which there was an even 2:2 split, and in the cases of J0741+2706 and J0825+3919 the indeterminate (2.1) class was chosen. In the cases of the three objects marked with a double dagger (‡), which includes one of the 2:2 splits, the objects were discussed and the final decision on the correct classification was unanimous. This was done without reference to the redshifts, luminosities, or physical sizes of these three objects.

Appendix D
(u, v) Coverage with a Near-Earth Orbiter

In Figure 16 we show the (u, v) coverage that could be obtained on a typical CSO with observations spread over 1 day per month over 18 months. For the chosen apogee and perigee heights of 32,000 km and 1000 km the precession rates of the R.A. of the ascending node (Ω) and the the argument of perigee (ω) are $-71°.4 \, \mathrm{yr}^{-1}$ and $+17°.8 \, \mathrm{yr}^{-1}$, respectively, for an orbit inclination of $60°$. This allows the large (u, v) holes obtained when observing the source closest to the orbit normal direction (as occurs in the first (u, v) coverage for each sequence shown) to be filled in with subsequent shorter-baseline observations when the source is observed further away from this direction due to Ω precession.
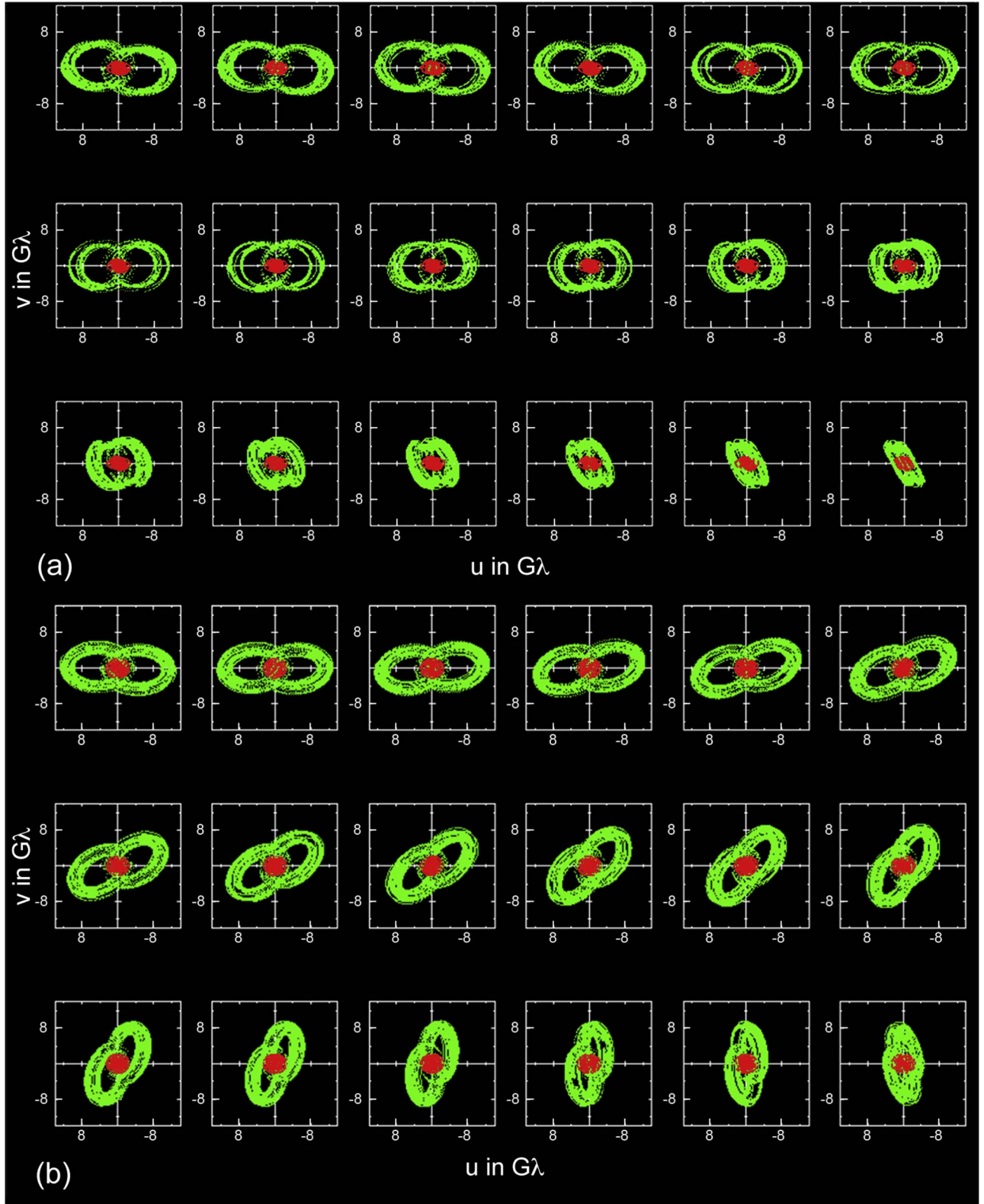
Figure 16. (u, v) coverage at 86 GHz with a near-Earth orbiter of apogee 2.5 Earth diameters at inclination 60° operating in conjunction with a ground array. Red tracks show Earth–Earth baselines and green tracks show space–Earth baselines. The successive frames show observations of duration 1 day spaced 1 month apart over an 18 month period. (a) For a source at decl. $\delta = 30°$ and (b) for a source at decl. $\delta = 60°$. Over an 18 month period holes in the (u, v) coverage are well filled. In order to fill the (u, v) gaps adequately, the observations over 1 day would not need to be continuous, and many objects could be observed each day. Such a near-Earth orbiter could observe many hundreds of CSOs (see text).

ORCID iDs

A. C. S Readhead ● https://orcid.org/0000-0001-9152-961X
V. Ravi ● https://orcid.org/0000-0002-7252-5485
R. D. Blandford ● https://orcid.org/0000-0002-1854-5506
A. G. Sullivan ● https://orcid.org/0000-0002-9545-7286
J. Somalwar ● https://orcid.org/0000-0001-8426-5732
M. C. Begelman ● https://orcid.org/0000-0003-0936-8488
M. Birkinshaw ● https://orcid.org/0000-0002-1858-277X
M. L. Lister ● https://orcid.org/0000-0003-1315-3412
T. J. Pearson ● https://orcid.org/0000-0001-5213-6231
G. B. Taylor ● https://orcid.org/0000-0001-6495-7731
S. Kiehlmann ● https://orcid.org/0000-0001-6314-9177
A. Siemiginowska ● https://orcid.org/0000-0002-0905-7375
K. Tassis ● https://orcid.org/0000-0002-8831-2038

References

An, T., & Baan, W. A. 2012, ApJ, 760, 77
An, T., Wu, F., Yang, J., et al. 2012, ApJS, 198, 5
Andreoni, I., Coughlin, M. W., Perley, D. A., et al. 2022, Natur, 612, 430
Angioni, R., Ros, E., Kadler, M., et al. 2019, A&A, 627, A148
Balbus, S. A., & Hawley, J. F. 1991, ApJ, 376, 214
Baldi, R. D. 2023, A&ARv, 31, 3
Baldi, R. D., Capetti, A., & Giovannini, G. 2015, A&A, 576, A38
Baldwin, J. E. 1982, in IAU Symp. 97, Extragalactic Radio Sources, ed. D. S. Heeschen & C. M. Wade (Dordrecht: Reidel), 21
Bartko, H., Martins, F., Trippe, S., et al. 2010, ApJ, 708, 834
Baum, S. A., O'Dea, C. P., Murphy, D. W., & de Bruyn, A. G. 1990, A&A, 232, 19
Begelman, M. C. 1996, in Cygnus A—Study of a Radio Galaxy, ed. C. L. Carilli & D. E. Harris (Cambridge: Cambridge Univ. Press), 209
Begelman, M. C., Blandford, R. D., & Rees, M. J. 1984, RvMP, 56, 255
Bell, E. F., McIntosh, D. H., Katz, N., & Weinberg, M. D. 2003, ApJS, 149, 289
Biggs, A. D., Zwaan, M. A., Hatziminaoglou, E., Péroux, C., & Liske, J. 2016, MNRAS, 462, 2819
Blandford, R., & Globus, N. 2022, MNRAS, 514, 5141
Blandford, R., Meier, D., & Readhead, A. 2019, ARA&A, 57, 467
Blandford, R. D. 1990, in Active Galactic Nuclei, ed. T. J.-L. Courvoisier & M. Mayor (Berlin: Springer), 161
Blandford, R. D. 1999, in ASP Conf. Ser. 160, Astrophysical Discs—an EC Summer School, ed. J. A. Sellwood & J. Goodman (San Francisco, CA: ASP), 265
Blandford, R. D., & Payne, D. G. 1982, MNRAS, 199, 883
Boccardi, B., Krichbaum, T. P., Ros, E., & Zensus, J. A. 2017, A&ARv, 25, 4
Bondi, M., Garrett, M. A., & Gurvits, L. I. 1998, MNRAS, 297, 559
Bondi, M., Marchã, M. J. M., Polatidis, A., et al. 2004, MNRAS, 352, 112
Bonnerot, C., & Lu, W. 2020, MNRAS, 495, 1374
Britzen, S., Brinkmann, W., Campbell, R. M., et al. 2007, A&A, 476, 759
Bromberg, O., Granot, J., Lyubarsky, Y., & Piran, T. 2014, MNRAS, 443, 1532
Bromberg, O., Nakar, E., Piran, T., & Sari, R. 2011, ApJ, 740, 100
Callingham, J. R., Gaensler, B. M., Ekers, R. D., et al. 2015, ApJ, 809, 168
Calzetti, D., Armus, L., Bohlin, R. C., et al. 2000, ApJ, 533, 682
Carilli, C. L., Perley, R. A., Dreher, J. W., & Leahy, J. P. 1991, ApJ, 383, 554
Carnall, A. C., McLure, R. J., Dunlop, J. S., & Davé, R. 2018, MNRAS, 480, 4379
Cendes, Y., Eftekhari, T., Berger, E., & Polisensky, E. 2021, ApJ, 908, 125
Cheng, X., An, T., Sohn, B. W., Hong, X., & Wang, A. 2021, MNRAS, 506, 1609
Cheng, X. P., & An, T. 2018, ApJ, 863, 155
Conway, J. E. 2002, NewAR, 46, 263
Conway, J. E., Pearson, T. J., Readhead, A. C. S., et al. 1992, ApJ, 396, 62
Curd, B. 2021, MNRAS, 507, 3207
Curd, B., Emami, R., Roelofs, F., & Anantua, R. 2022, Galax, 10, 117
Czerny, B., Siemiginowska, A., Janiuk, A., Nikiel-Wroczyński, B., & Stawarz, Ł. 2009, ApJ, 698, 840
Dallacasa, D., Orienti, M., Fanti, C., Fanti, R., & Stanghellini, C. 2013, MNRAS, 433, 147
Davis, S. W., & Tchekhovskoy, A. 2020, ARA&A, 58, 407

De Colle, F., & Lu, W. 2020, NewAR, 89, 101538
de Vries, N., Snellen, I. A. G., Schilizzi, R. T., Mack, K. H., & Kaiser, C. R. 2009, A&A, 498, 641
Dong, D. Z., Hallinan, G., Nakar, E., et al. 2021, Sci, 373, 1125
Dotter, A. 2016, ApJS, 222, 8
Duggal, C., O'Dea, C., Baum, S., et al. 2021, AN, 342, 1087
Event Horizon Telescope Collaboration, Akiyama, K., Alberdi, A., et al. 2019, ApJL, 875, L1
Fanaroff, B. L., & Riley, J. M. 1974, MNRAS, 167, 31P
Fanti, C., Fanti, R., Dallacasa, D., et al. 1995, A&A, 302, 317
Fomalont, E. B., Frey, S., Paragi, Z., et al. 2000, ApJS, 131, 95
Giroletti, M. 2008, in ASP Conf. Ser. 386, Extragalactic Jets: Theory and Observation from Radio to Gamma Ray, ed. T. A. Rector & D. S. DeYoung (San Francisco, CA: ASP), 176
Giroletti, M., Giovannini, G., & Taylor, G. B. 2005, A&A, 441, 89
Giroletti, M., Giovannini, G., Taylor, G. B., et al. 2003, A&A, 399, 889
Godfrey, L. E. H., & Shabala, S. S. 2013, ApJ, 767, 12
Gräfener, G. 2021, A&A, 647, A13
Gugliucci, N. E., Taylor, G. B., Peck, A. B., & Giroletti, M. 2005, ApJ, 622, 136
Gugliucci, N. E., Taylor, G. B., Peck, A. B., & Giroletti, M. 2007, ApJ, 661, 78
Guillochon, J., & Ramirez-Ruiz, E. 2013, ApJ, 767, 25
Hallinan, G., Ravi, V., Weinreb, S., et al. 2019, BAAS, 51, 255
Hargrave, P. J., & Ryle, M. 1974, MNRAS, 166, 305
Harrison, R., Gottlieb, O., & Nakar, E. 2018, MNRAS, 477, 2128
Helmboldt, J. F., Taylor, G. B., Tremblay, S., et al. 2007, ApJ, 658, 203
Horesh, A., Cenko, S. B., & Arcavi, I. 2021, NatAs, 5, 491
Johnston, S., Taylor, R., Bailes, M., et al. 2008, ExA, 22, 151
Jonas, J. & MeerKAT Team 2016, MeerKAT Science: On the Pathway to the SKA (MeerKAT2016) (Trieste: Sissa)
Kaiser, C. R., Dennett-Thorpe, J., & Alexander, P. 1997, MNRAS, 292, 723
Kelley, L. Z., Tchekhovskoy, A., & Narayan, R. 2014, MNRAS, 445, 3919
Kharb, P., Gabuzda, D. C., O'Dea, C. P., Shastri, P., & Baum, S. A. 2009, ApJ, 694, 1485
Kiehlmann, S., Lister, M. L., Readhead, A. C. S., et al. 2024a, ApJ, 961, 240
Kiehlmann, S., Readhead, A. C. S., O'Neill, S., et al. 2024b, ApJ, 961, 241
Kochanek, C. S. 2016, MNRAS, 461, 371
Komatsu, E., Dunkley, J., Nolta, M. R., et al. 2009, ApJS, 180, 330
Koratkar, A., & Blaes, O. 1999, PASP, 111, 1
Kormendy, J., & Ho, L. C. 2013, ARA&A, 51, 511
Kosmaczewski, E., Stawarz, Ł., Siemiginowska, A., et al. 2020, ApJ, 897, 164
Kubota, A., & Done, C. 2018, MNRAS, 480, 1247
Kunert-Bajraszewska, M., Gawroński, M. P., Labiano, A., & Siemiginowska, A. 2010, MNRAS, 408, 2261
Kunert-Bajraszewska, M., Marecki, A., & Thomasson, P. 2006, A&A, 450, 945
Kunert-Bajraszewska, M., Marecki, A., Thomasson, P., & Spencer, R. E. 2005, A&A, 440, 93
Lacy, M., Baum, S. A., Chandler, C. J., et al. 2020, PASP, 132, 035001
Lara, L., Cotton, W. D., Feretti, L., et al. 2001a, A&A, 370, 409
Lara, L., Márquez, I., Cotton, W. D., et al. 2001b, A&A, 378, 826
Lawrence, C. R., Zucker, J. R., Readhead, A. C. S., et al. 1996, ApJS, 107, 541
Levinson, A., & Begelman, M. C. 2013, ApJ, 764, 148
Levinson, A., & Globus, N. 2017, MNRAS, 465, 1608
Lister, M. L., Aller, M. F., Aller, H. D., et al. 2018, ApJS, 234, 12
Lister, M. L., Homan, D. C., Kovalev, Y. Y., et al. 2020, ApJ, 899, 141
Lister, M. L., Kellermann, K. I., Vermeulen, R. C., et al. 2003, ApJ, 584, 135
Lister, M. L., & Smith, P. S. 2000, ApJ, 541, 66
Longair, M. S. 2011, High Energy Astrophysics (3rd ed.; Cambridge: Cambridge Univ. Press)
Longair, M. S., & Scheuer, P. A. G. 1970, MNRAS, 151, 45
Lyubarsky, Y. 2009, ApJ, 698, 1570
Lyubarsky, Y. 2011, PhRvE, 83, 016302
MacLeod, M., Guillochon, J., & Ramirez-Ruiz, E. 2012, ApJ, 757, 134
Magorrian, J., & Tremaine, S. 1999, MNRAS, 309, 447
Maness, H., Martins, F., Trippe, S., et al. 2007, ApJ, 669, 1024
Maness, H. L., Taylor, G. B., Zavala, R. T., Peck, A. B., & Pollack, L. K. 2004, ApJ, 602, 123
Marecki, A., Barthel, P. D., Polatidis, A., & Owsianik, I. 2003, PASA, 20, 16
McConville, W., Ostorero, L., Moderski, R., et al. 2011, ApJ, 738, 148
Mockler, B., Twum, A. A., Auchettl, K., et al. 2022, ApJ, 924, 70
Momjian, E., Romney, J. D., Carilli, C. L., & Troland, T. H. 2003, ApJ, 597, 809
Morton, B. R., Taylor, G., & Turner, J. S. 1956, RSPSA, 234, 1
Murphy, T., Chatterjee, S., Kaplan, D. L., et al. 2013, PASA, 30, e006

Mutel, R. L., & Phillips, R. B. 1980, ApJL, 241, L73
Narayan, R., Chael, A., Chatterjee, K., Ricarte, A., & Curd, B. 2022, MNRAS, 511, 3795
Nayakshin, S., & Sunyaev, R. 2005, MNRAS, 364, L23
Norman, S. M. J., Nixon, C. J., & Coughlin, E. R. 2021, ApJ, 923, 184
O'Dea, C. P. 1998, PASP, 110, 493
O'Dea, C. P., Baum, S. A., & Stanghellini, C. 1991, ApJ, 380, 66
O'Dea, C. P., & Saikia, D. J. 2021, A&ARv, 29, 3
Orienti, M., & Dallacasa, D. 2014, MNRAS, 438, 463
Orienti, M., Dallacasa, D., Fanti, C., et al. 2004, A&A, 426, 463
Orienti, M., Dallacasa, D., Tinti, S., & Stanghellini, C. 2006, A&A, 450, 959
Orienti, M., Murgia, M., & Dallacasa, D. 2010, MNRAS, 402, 1892
Orienti, M., Murgia, M., Dallacasa, D., Migliori, G., & D'Ammando, F. 2023, MNRAS, 522, 3877
Osaki, Y. 1996, PASP, 108, 39
Owsianik, I., & Conway, J. E. 1998, A&A, 337, 69
Owsianik, I., Conway, J. E., & Polatidis, A. G. 1999, NewAR, 43, 669
Parfrey, K., Philippov, A., & Cerutti, B. 2019, PhRvL, 122, 035101
Pasham, D. R., & van Velzen, S. 2018, ApJ, 856, 1
Paumard, T., Genzel, R., Martins, F., et al. 2006, ApJ, 643, 1011
Paxton, B., Schwab, J., Bauer, E. B., et al. 2018, ApJS, 234, 34
Peacock, J. A., & Wall, J. V. 1982, MNRAS, 198, 843
Pearson, T. J., & Readhead, A. C. S. 1988, ApJ, 328, 114
Peck, A. B., & Taylor, G. B. 2000, ApJ, 534, 90
Peck, A. B., Taylor, G. B., & Conway, J. E. 1999, ApJ, 521, 103
Perucho, M., Martí, J.-M., & Quilis, V. 2019, MNRAS, 482, 3718
Pfister, H., Bar-Or, B., Volonteri, M., Dubois, Y., & Capelo, P. R. 2019, MNRAS, 488, L29
Phillips, R. B., & Mutel, R. L. 1980, ApJ, 236, 89
Phinney, E. S. 1989, in IAU Symp.136, The Center of the Galaxy, ed. M. Morris (Dordrecht: Kluwer), 543
Planck Collaboration, Aghanim, N., Akrami, Y., et al. 2020, A&A, 641, A6
Polatidis, A. G. 2009, AN, 330, 149
Polatidis, A. G., & Conway, J. E. 2003, PASA, 20, 69
Polatidis, A. G., Wilkinson, P. N., Xu, W., et al. 1995, ApJS, 98, 1
Pooley, G. G., & Ryle, M. 1968, MNRAS, 139, 515
Readhead, A. C. S., Pearson, T. J., & Unwin, S. C. 1984, in IAU Symp. 110, VLBI and Compact Radio Sources, ed. R. Fanti, K. I. Kellermann, & G. Setti (Dordrecht: Reidel), 131
Pushkarev, A. B., Kovalev, Y. Y., Lister, M. L., & Savolainen, T. 2017, MNRAS, 468, 4992
Rastello, S., Dallacasa, D., & Orienti, M. 2016, AN, 337, 42
Readhead, A. C. S., Taylor, G. B., Xu, W., et al. 1996, ApJ, 460, 612
Readhead, A. C. S., Xu, W., Pearson, T. J., Wilkinson, P. N., & Polatidis, A. 1993, AAS Meeting 182, 53.07
Readhead, A. C. S., Xu, W., Pearson, T. J., Wilkinson, P. N., & Polatidis, A. G. 1994, in Compact Extragalactic Radio Sources, ed. J. A. Zensus & K. I. Kellermann (Green Bank, WV: National Radio Astronomy Observatory), 17
Rees, M. J. 1988, Natur, 333, 523
Reynolds, C. S., & Begelman, M. C. 1997, ApJL, 487, L135

Ripperda, B., Liska, M., Chatterjee, K., et al. 2022, ApJL, 924, L32
Rybicki, G. B., & Lightman, A. P. 1985, Radiative Processes in Astrophysics (New York: Wiley), 155
Saikia, D. J., Gupta, N., & Konar, C. 2007, MNRAS, 375, L31
Saikia, D. J., Konar, C., & Kulkarni, V. K. 2006, MNRAS, 366, 1391
Salpeter, E. E. 1955, ApJ, 121, 161
Scheuer, P. A. G. 1974, MNRAS, 166, 513
Scheuer, P. A. G., & Readhead, A. C. S. 1979, Natur, 277, 182
Schmidt, M. 1968, ApJ, 151, 393
Schoenmakers, A. P., de Bruyn, A. G., Röttgering, H. J. A., & van der Laan, H. 1999, A&A, 341, 44
Shabala, S. S., & Godfrey, L. E. H. 2013, ApJ, 769, 129
Shakura, N. I., & Sunyaev, R. A. 1973, A&A, 24, 337
Shankar, F., Weinberg, D. H., & Miralda-Escudé, J. 2009, ApJ, 690, 20
Siemiginowska, A., Sobolewska, M., Migliori, G., et al. 2016, ApJ, 823, 57
Simon, J. B., Hawley, J. F., & Beckwith, K. 2011, ApJ, 730, 94
Smak, J. 1984, AcA, 34, 161
Sobolewska, M., Migliori, G., Ostorero, L., et al. 2022, ApJ, 941, 52
Somalwar, J. J., Ravi, V., Dong, D. Z., et al. 2023, ApJ, 945, 142
Stanghellini, C. 2003, PASA, 20, 118
Stanghellini, C., O'Dea, C. P., Baum, S. A., et al. 1997, A&A, 325, 943
Stanghellini, C., O'Dea, C. P., Dallacasa, D., et al. 1998, A&AS, 131, 303
Stanghellini, C., O'Dea, C. P., Dallacasa, D., et al. 2005, A&A, 443, 891
Stawarz, Ł., Ostorero, L., Begelman, M. C., et al. 2008, ApJ, 680, 911
Taylor, G. B., Charlot, P., Vermeulen, R. C., & Pradel, N. 2009, ApJ, 698, 1282
Taylor, G. B., Fassnacht, C. D., Sjouwerman, L. O., et al. 2005, ApJS, 159, 27
Taylor, G. B., Marr, J. M., Pearson, T. J., & Readhead, A. C. S. 2000, ApJ, 541, 112
Taylor, G. B., Readhead, A. C. S., & Pearson, T. J. 1996, ApJ, 463, 95
Taylor, G. B., Vermeulen, R. C., Pearson, T. J., et al. 1994, ApJS, 95, 345
Tchekhovskoy, A., Metzger, B. D., Giannios, D., & Kelley, L. Z. 2014, MNRAS, 437, 2744
Tchekhovskoy, A., Narayan, R., & McKinney, J. C. 2011, MNRAS, 418, L79
Tremblay, S. E., Taylor, G. B., Helmboldt, J. F., Fassnacht, C. D., & Pearson, T. J. 2008, ApJ, 684, 153
Tremblay, S. E., Taylor, G. B., Ortiz, A. A., et al. 2016, MNRAS, 459, 820
Tzioumis, A., King, E., Morganti, R., et al. 2002, A&A, 392, 841
van Breugel, W., Miley, G., & Heckman, T. 1984, AJ, 89, 5
van Velzen, S. 2018, ApJ, 852, 72
Wang, Y., He, Z., Mao, J., et al. 2022, ApJ, 928, 7
White, R. L., & Becker, R. H. 1992, ApJS, 79, 331
Wilkinson, P. N., Booth, R. S., Cornwell, T. J., & Clark, R. R. 1984, Natur, 308, 619
Wilkinson, P. N., Polatidis, A. G., Readhead, A. C. S., Xu, W., & Pearson, T. J. 1994, ApJL, 432, L87
Willett, K. W., Stocke, J. T., Darling, J., & Perlman, E. S. 2010, ApJ, 713, 1393
Wójtowicz, A., Stawarz, Ł., Cheung, C. C., et al. 2020, ApJ, 892, 116
Woods, A. W. 2010, AnRFM, 42, 391
Wright, A. H., 2016 LAMBDAR: Lambda Adaptive Multi-band Deblending Algorithm in R, Astrophysics Source Code Library, ascl:1604.003